Examining the deformation in the Krafla region, Iceland

Vummidi Narayanee (4898699)

To get an insight on the recent changes in the observed deformation pattern

Committee:
Dr. Elske de Zeeuw-van Dalfsen
Dr.ir. Sandra Verhagen
Dr.ir. W. (Wouter) van der Wal

TU Delft

Examining the deformation in the Krafla region, Iceland

by

Vummidi Narayanee (4898699)

to obtain the degree of Master of Science
at the Delft University of Technology,
to be defended publicly on Friday October 30, 2020 at 13.30.

Student number:	4898699	
Project duration:	December, 2019 – October, 2020	
Thesis committee:	Dr. Elske de Zeeuw-van Dalfsen	Daily Superviosr, TU Delft.
	Dr. ir. Sandra Verhagen,	Supervisor, TU Delft.
	Dr. ir. W. (Wouter) van der Wal,	External Supervisor, Tu Delft.

Acknowledgements

" No one who achieves success does so without acknowledging the help of others. The wise and confident acknowledge this help with gratitude." -Alfred North Whitehead

My deepest gratitude to Dr. Elske de Zeeuw-van Dalfsen, my guiding light throughout. I vividly remember attending her first class, the ways in which she made the difficult concepts sound simple and my admiration for both her and for what she taught. She has been the pillar of support not only academically but also emotionally. Her appreciation for the smallest of things motivated me to push forward even during the some of my low-points and made me want to do better every time. My heartfelt thank you to Dr.ir. Sandra Verhagen, who always kept me on check with regards to deadlines. Her line of questioning and critical evaluation during our weekly meetings moulded me to think better and become more prudent. Thank you, Dr.ir. W. (Wouter) van der Wal who graciously agreed to being my external supervisor and committee member. He was both empathetic regarding my difficulties and gave me perspective regarding my thesis. InSAR processing, one of the important parts of my thesis and something I was new to, was possible because of Dr.ir. F.J. (Freek) van Leijen and Adriaan van Natijne. Thank you for both your time and patience. The contribution of University of Iceland and ISOR who provided the data for this project, is truly appreciated.

I wish to acknowledge the support and great love my parents, V. Gopal and V. Sujatha Gopal, provided. They did their best to keep me sane. From miles away, they sensed my troubles and wiped them away. Despite the financial crunch we faced, not once did my parents let me know the difficulties they were going through. I am who I am today, because of my parents and I am supremely blessed to have them. Along with gratitude, as this marks another milestone in my life, I promise to keep them happy and make them proud. If there's one thing my parents have taught me, it is to be grateful to whatever I have. This is my gratitude to them. Thank you to my sister, Poornima, who checked in on me week after week and made sure that I keep well.

Last but not least, my friend Samyuktha from bachelors who is currently doing her masters with me is my main support. She made me feel like home even when I am away from my home. She stood as a pillar of support without her this would have been many folds difficult. At times when I lost confidence in myself, she helped me regain it. I am really fortunate to have her by my side. My friends from my country of birth need special mention for putting up with all my woes. Reshmma and Anush, the two souls who happily listened to me always even when I was complaining about something for the nth time, thank you for being my biggest support. Nisanth, RaghavaPriya, Aswath and Prasanth, who took turns to talk to me and keep my mind off the problems at the end of a hectic day, thank you for keeping me sane from afar. All of them (and many others) who were there for me during the oddest hours despite the time zone differences, who celebrated my progress and set-backs making me realize that neither define me, make my world a little better. Thank you to Lord Almighty for all the blessings showered upon me.

Abstract

In the Krafla region in North East Iceland, a change in the deformation pattern was observed in 2018. Since the 1975-1984 rifting event, there was subsidence seen in the Krafla caldera and along the fissure swarm. This subsidence was explained by deflation which decreased exponentially along the years. In 2018, this deformation pattern reversed, and for the first time since 1989, uplift was observed in the region. Therefore, this work concentrates on examining the change in deformation pattern in the region that occurred in 2018. Four geodetic techniques, a combination of ground and space geodetic techniques, are used to study this change in deformation pattern noted in the Krafla region. Data from 2016 to 2019 are considered as they span the time of interest when the change took place. In levelling, InSAR and GPS, the uplift observed is located to the North of the Krafla power plant. Similarly, there is an increase in net gravity seen to the North of the power plant. This suggests there is an increase in mass/density. A possible reason could be movement of magma from the deep to the shallow magma chamber. The reason behind this start of the magma movement is not known. On the other hand, there is continued subsidence and an increase in net gravity seen in the fissure swarms present to the south of the power plant. This result agrees with the fact that the uplift is concentrated (a local phenomena) in the northern region and there is still subsidence seen in the south.

A simple Mogi model is fitted to InSAR and GPS data to understand the cause for this change in deformation. But, the fitted model provided very few insights in this work. The results from modelling mainly concentrated on the subsidence in the southern region and corresponding model parameters were obtained. The location of the source responsible for the modelled deformation (subsidence) is found to be near the power plant. The depth and volume however are not properly constrained. But since the model tries to constrain at deeper depths, correspondingly larger volume is also seen. This outcome strengthens the hypothesis that the source for the deformation could lie at deeper depths.

Based on the overall results, the following recommendations are made to enhance the results: i) Maintaining the continuity in the data ii) To increase the number of benchmarks measured near the deformation area (especially in gravity and levelling) iii) Use of multiple source modelling for the better understanding of the sub-surface processes.

Abbreviations

AOE	Atmosphere and Orbit Error
BCFAG	Bouguer Corrected Free Air Gradient
B.S	Backsight
CGPS	Continuous Global Positioning System
DInSAR	Differential Interferometric Synthetic Aperture Radar
DEM	Digital Elevation Model
ERS	European Remote Sesnsing
EVZ	Eastern Volcanic Zone
FAG	Free Air Gradient
F.S	Foresight
GAMIT	GNSS At MIT
GBIS	Geodetic Bayesian Inversion Software
GIA	Glacial Isostatic Adjustment
GLOBK	Global Kalman filter
GLONASS	GLObal NAvigation Satellite Systems
GNSS	Global Navigation Satellite Systems
GPS	Global Positioning System
InSAR	Interferometric Synthetic Aperture Radar
ITRF	International Terrestrial Reference Frame
IW	Interferometric Wide
LOS	Line Of Sight
NRCAN	National Resources Canada
NVZ	Northern Volcanic Zone
PDF	Probability Density Function
PPK	Post Processed Kinematic
PPP	Precise Point Positioning
PS	Permanent Scatters
PSI	Persistent Scatterer Interferometry
RINEX	Receiver Independent Exchange Format
SAR	Synthetic Aperture Radar
S.D	Standard Deviation
SLC	Single Look Complex
SNAP	SentiNel Application Platform
SNR	Signal to Noise Ratio
StaMPS	Stanford Method for Permanent Scatters
TOPSAR	Terrain Observation with Progressive Scans Synthetic Aperture Radar
TFZ	Tjórnes Fracture Zone
WVZ	Western Volcanic Zone

List of Figures

List of Tables

Contents

1

Background Information

1.1. Introduction

Iceland is one of the few places in the world which has a large number of active volcanoes located on it. Iceland is located at the intersection of the Mid-Atlantic Ridge and the Greenland-Faeroes Ridge. The width of the Island is approximately 500 Km extending in the east-west direction, and the length of the island is around 300 Km extending in the north-south direction. Iceland is a part of the oceanic plateau and it is one of the very few places with the mid-oceanic ridge present above the sea level. There is a hotspot or mantle plume situated below the central and the north-western part of Iceland. Therefore, this anomalous mantle elevates the country above the sea level making Iceland a sub-aerial part of the Mid-Atlantic Ridge. Therefore, these remarkable features, their interaction and their results have made Iceland a place to learn extensively on geodynamics [Sigmundsson, 2006].

The subaerial part of the divergent plate boundary between the North American and Eurasian plates is marked by a series of spreading centres causing countrywide deformation in Iceland. Plate divergence occurs at the rate of 17-19.5 mm/year in the direction N (105-110)°E within 50-150 Km wide zones [Drouin and Sigmundsson, 2019; Árnason, 2020]. The plate spreading was well measured in the past only by the electronic distance measurements, optical levelling, Lake level measurements and tiltmeters. Glacial Isostatic Adjustment (GIA) is the other source of countrywide deformation. The retreat of ice from various ice caps and mainly from the Vatnajkull ice cap in Iceland is one of the main reasons for GIA. At present, these large scale deformations are well monitored and observed through the time by the Space geodetic techniques like GPS and InSAR [Árnadóttir et al., 2009]. Therefore, this enhances the knowledge of crustal deformation caused by plate spreading and GIA [Drouin et al., 2017].

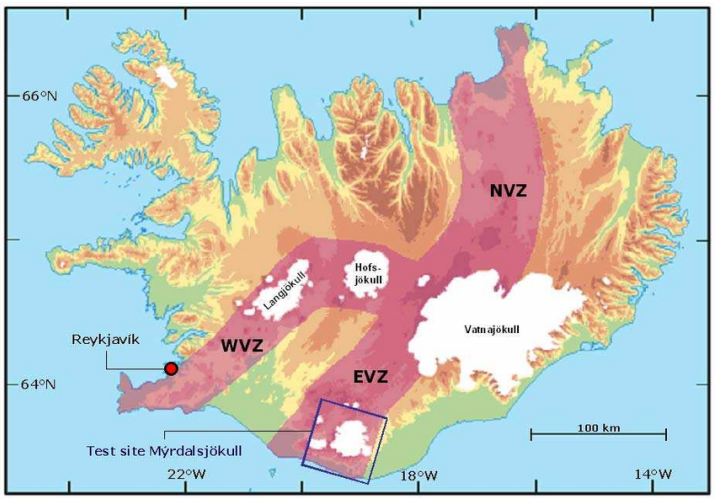

Figure 1.1: Neovolcanic Zone of Iceland is shown in pink color in the above Topographic map. The Northern (NVZ), Eastern (EVZ) and Western Volcanic zone (WVZ) are represented as well. In addition to this, the icecaps present in Iceland are shown in white.

The surface expression of the mid-ocean ridge in Iceland is the neovolcanic zone which consists of active volcanoes[Gudmundsson, 2000]. The neovolcanic area (Figure 1.1) is divided into the axial rift zone representing the plate spreading with the active volcanoes and the flank zone, which describes the isolated volcanic systems present off-axis. The neovolcanic area has three main segments: the Northern Volcanic Zone (NVZ), Eastern (EVZ) and Western Volcanic Zone (WVZ). These volcanic zones have a certain number of active volcanoes, and several eruptions have occurred in the recent past. In this work, there will be a focus on the small area of the NVZ.

1.2. Northern Volcanic Zone

The Northern Volcanic Zone (NVZ) is bounded by the Tjórnes Fracture Zone (TFZ) in the north and by the Vatnajkull ice cap in the south (Figure 1.2). Each volcanic system present in this zone 1.2 has a central volcano and an associated fissure swarm. The volcanic systems are arranged in a left-stepping "en echelon" pattern along the axial rift zone. The Volcanic systems present in this zone from north to south are named after their respective central volcanoes: Theistareykir, Krafla, Fremrinámar, Askja and Kverkfjll [Einarsson, 2008]. These volcanic systems have specific characteristics in common, but they have marked differences between each other too. Theistareykir has a powerful and well-developed fissure swarm but no caldera. The presumed last rifting episode that occurred in this region was in 1618 [Tryggvason, 1984]. The krafla volcanic system has a partly filled caldera with a pervasive fissure swarm. The last rifting episode in Krafla occurred in 1975-1985. The Fremrinámar volcanic system has a shield volcano and two large lava fields cover its central volcano. No calderas are visible in this region. The fissure swarm of the Askja volcanic system is very long and the central volcano hosts three overlapping calderas. This volcano erupted several times between 1920-1930 following the major eruption that occurred in 1875. The last eruption happened in 1961. Kverkfjöll, a large stratovolcano is hidden beneath the North-East end of the Vatnajökull glacier. It has two calderas filled with ice. Many eruptions took place in 1720 in this region. The last eruption in this region occurred in 1968.

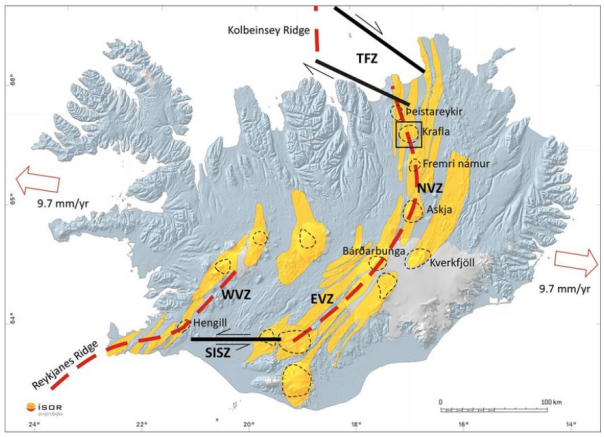

Figure 1.2: The Northern Volcanic Zone with the volcanic systems present in it. Thin black lines represent the central volcanoes and the yellow region represent the fissure swarm [Árnason, 2020]

The Krafla and the Askja volcanic systems have well-developed chambers [Einarsson, 1978;Tryggvason, 1989]. The rifting process does not require a well-developed magma chamber, but a volcanic system which contains a magma chamber in the roots of its central volcano rifts more frequently than the ones which do not have magma chambers. Additionally, the volcanic systems with a magma chamber have a thinner crust. This can be observed in the areas of Theistareykir and Fremrinámar volcanic systems because the rifting there occurs at much longer intervals and their crustal thickness is larger than that of the Krafla or Askja volcanic system [Björnsson, 1985]. When the rifting takes place in one fissure swarm, land rise and contraction happen on either side due to the elastic rebound. This elastic rebound releases tension in the adjacent echelon arranged fissure swarm which prevents simultaneous rifting. For example, the Krafla fires (1975-1984) were confined to the Northern region of the Krafla caldera as the tension in the south was released during the rifting episode of the Askja fissure swarm in 1874-1875 [Björnsson, 1985].

1.3. Krafla Volcanic system

Krafla is the central volcano of the Krafla volcanic system. The Krafla area is one of the most studied places in Northern Iceland due to the geothermal plant situated above the inferred location of the shallow magma chamber of the caldera region. Additionally, the area is easily accessible, which helps in continuous monitoring of the region for various geodynamic studies. The central caldera measures about 10 Km east-west and about 8 km north-south. A N10°E trending fissure swarm transects the caldera. The fissure swarms are the surface expressions of the rifting events that have occurred in the past with dike intrusions. The length of the Krafla fissure swarm is 100 Km and its width is about 5-10 Km. The fissure swarm extends both in the north and the south direction. The caldera region contains mostly basaltic eruption products but rhyolitic domes are formed around the caldera rims. These domes are formed due to the high viscosity of the rhyolite magma which finally forms a lava dome near the vent.

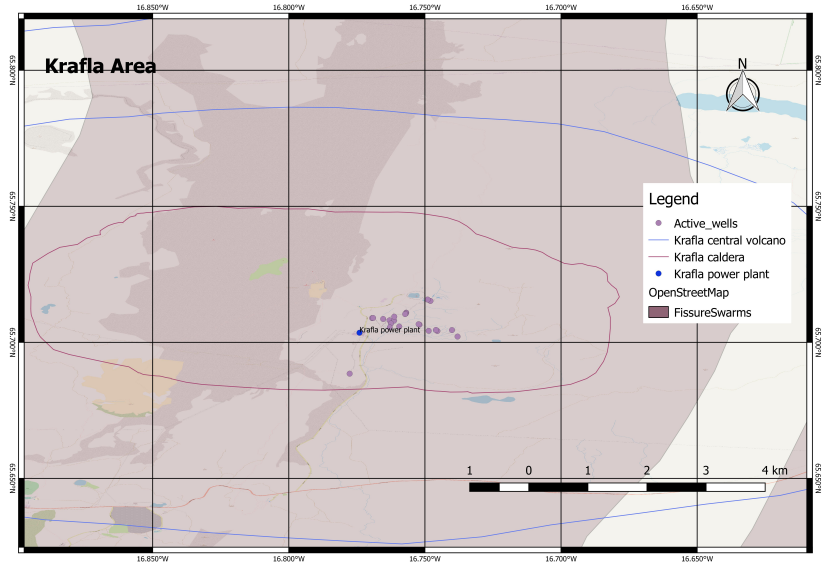

Figure 1.3: Complete Overview of Krafla region with Krafla Caldera, central volcano, power plant and the fissure swarm in the background.

1.3.1. Past rifting events

In the past, the Mývatn fires (1724 – 1729) and the Krafla fires (1975 – 1984) were the two rifting events which were recorded in the Krafla region. The former event time line is given in the following table 1.1 [Björnsson et al., 1977].

Table 1.1: Chronology and description of the events during the Mývatn fires

Time of the event	Description of event
May-1724	Formation of row of explosion craters. Eruption was mainly from the Viti crater.
January-1725	Earthquakes occurred and ground fissures opened along the swarm in the southern region of Krafla.
	Steam and Mud craters were formed in the Krafla and Námafjall geothermal fields.
	Earthquakes were felt throughout 1725.
August-1727	Fissure eruption started in the centre of the Caldera
April-1728	Eruptive fissure extended southwards to Námafjall
September-1729	Lava flow ceased when the eruption stopped.

During the latter event, geodetic measurements monitored the complete rifting process. The timeline of the Krafla rifting episode [Tryggvason, 1989; Tryggvason, 1986] is given in the table 1.2. The following table lists the epochs at which the deflation occurred. The ground deformation between these events was mostly inflation and at times, there was no significant movement seen.

Table 1.2: Chronology and description of the events in the Krafla fires

Subsidence-Rifting event (Time)	Description of the event
20-December-1975	Beginning of the rifting episode with large subsidence in leirhnjúkur (center of the Krafla caldera). This intense earthquake swarm lasted up to February-1976.
28-September-1976	Small deflation was seen in the north of leirhnjúkur.Rifting occurred with no surface fissures. This event lasted up to 4-October-1976.
31-October-1976	Rapid and large deflation was seen for less than 48 hours.Intense earthquake swarm accompanied this event. Majority of them was located about 10 Km north of leirhnjúkur.
20-January-1977	Rapid deflation accompanied by earthquake.Highest concentration of earthquakes about 7 Km north of leirhnjúkur. This event lasted for less than 24 hours.
27-April-1977	Raid deflation accompanied by minor eruption about 3 Km north of leirhnjúkur. Fissures were seen to open across the Krafla Caldera and as far as 15 - 20 Km South of leirhnjúkur.
8-September-1977	Rapid deflation accompanied by lava eruption in the north and south of leirhnjúkur.
2-November-1977	Small and rapid deflation occurred. The subsidence lasted for 2 hours.
7-January-1978	Slow deflation rate. Intense earthquake swarm accompanied this deflation and rifting event. The epicentres were distributed along the fissure swarm from about 10 - 45 Km north of leirhnjúkur.
10-July-1978	Slow deflation and lasted about 3 days. This event was accompanied by earthquake
10-November-1978	The deflation rate was slow and lasted for 5 days. This event was accompanied by earthquake located at 18 - 28 Km north of leirhnjúkur.
13-May-1979	Slow deflation and lasted for 5 days. This event was accompanied by earthquake located at 12 - 23 Km north of leirhnjúkur.
3-December-1979	Minor deflation continued for 4-6 days. No fissuring was observed.
11-February-1980	Slow deflation started and lasted 4 - 5 days. Earthquake epicentres were found at the south of leirhnjúkur.
16-March-1980 10-July-1980	Very rapid deflation and lasted about 12 hours. Fissure eruption with lava was seen from 1- 6 Km north of leirhnjúkur. Moderately fast deflation with lava eruption. These both continued for 7 days.
18-October-1980	Rapid deflation followed by fissure eruption and lava production which continued for 5 days.
25-December-1980	Slow deflation and lasted up to December 28,1980.
30-January-1981	Rapid deflation accompanied by fissure eruption from 6 - 8 Km north of leirhnjúkur. This event lasted for 4 days.
18-November-1981	Rapid deflation accompanied by fissure eruption. The eruption extended northwards from leirhnjúkur to 6.5 Km north of leirhnjúkur.
1982 - 1984	Slow Inflation
4-September-1984	Rapid deflation with seismic tremors. The eruption began in the north of leirhnjúkur. In the next minute, there was eruption seen in the south of leirhnjúkur as well. This event lasted up to 18-September-1980.

At least 20 inflation/deflation cycles were recorded, out of which nine resulted in basaltic fissure eruptions (figure 1.4 shows the rifting and volcanic eruptions from 1975 - 1982, the rest can be seen in the table 1.2). During each cycle, the reservoir pressure exceeded the critical value, leading to the injection of dykes into the fissure swarms, which finally resulted in rifting. Various geodetic techniques like electronic distance mea-

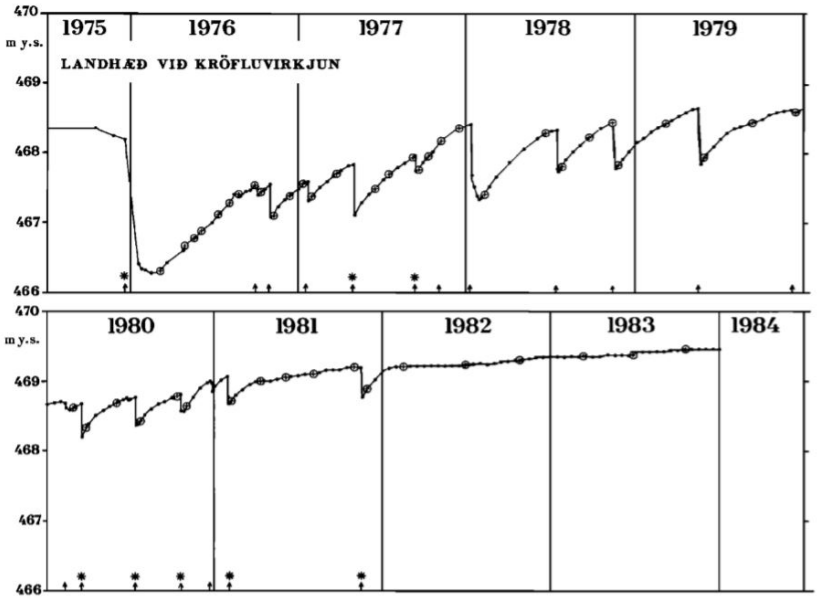

Figure 1.4: Represents the Inflation/Deflation cycles from 1975 to 1982. The Arrows represent the rifting events and the star represents the volcanic eruption

surements, precise levelling, lake levelling and optical levelling carefully examined the deformation during rifting [Björnsson, 1985]. The subsurface solidification was mostly due to dikes caused by the magma from the shallow magma chambers. After the last eruption in 1984, there was inflation seen in the magma chamber until 1989. Then the area has been subsiding since 1989. Geodetic techniques like InSAR, GPS and Levelling monitored these deformations after the rifting episode. There was continuous subsidence seen in the region until 2015 [Drouin et al., 2017]. In addition to this, constant inflation was observed in the north of the Krafla caldera, which represented deep magma accumulation or post-rifting relaxation [Dalfsen et al., 2004]. Apart from the deformation data, the Krafla region has the advantage of long term gravimetric data. The results from gravimetry show a significant gravity decrease in the caldera region which represents significant mass decrease or cooling in the magma chamber[de Zeeuw-van Dalfsen et al., 2006]. Besides the magma chambers, crustal deformation was affected by the extraction of water in the Krafla area. The extraction of water additionally caused subsidence in the region. Therefore, the various processes that affect the deformation in the Krafla region are given as follows:

1. Plate spreading (Tectonic setting)
2. Glacial Isostatic adjustment
3. Volcanic processes: Movement of magma between the chambers or cooling of the magma
4. Human Induced process: Geothermal power plants (Extraction/Injection of water)

1.4. Relevant previous research

The following section provides information on the use of geodetic techniques in the past to understand the deformation during the rifting process and the post-rifting process. Active studies have been going in the Krafla region for the past 50 years. The foremost research after the beginning of the rifting event in 1975 was done by Björnsson et al. [1977]. He explained the initial seismic activity and the lava eruption that took place in 1975 and 1976. Field observations, Levelling and the Tilt observations aided in identifying the changes that happened in the Krafla region after the initial rifting event in 1975. The upward movement of magma and its accumulation were the reasons stated for inflation. On the other hand, deflation was stated due to the movement of magma from the chamber to the fissure swarms on account of exceeded pressure in the chamber and the widening seen in the fissure swarm. To substantiate the presence of a shallow magma chamber, Einarsson[1978] used the technique of S-wave attenuation. The attenuation was seen near the centre of the caldera region, which leads to the fact that the magma chamber is a localized feature. The extent of magma was not

well mapped but the upper limit was found at a depth of (app) 7 Km. To deepen the knowledge about ground deformation Johnsen et al.[1980] used gravity measurements and compared it with the elevation changes measured using levelling. The elevation changes were converted into gravity changes (using the combined free air and Bouguer model) and then it was compared to the measured gravity measurements. Finally, the analysis indicated that the inflation and deflation in the caldera were due to the inflow and the outflow of the magma with speculation on the influence of groundwater during the deflation events. On the other hand, Hauksson[1983] studied the underlying process of fissure opening and its growth using the data from the displacement meters that were deployed in 1977 and 1980. The interplay between the fissure opening and the magma pressure was well described. The work indicated that the period of fissure opening is almost equal to the period of land uplift. Similarly, Tryggvason[1984] studied more about the widening of the fissure swarms using the microwave distance measurements. Summing up all the events up to 1983, Björnsson[1985] presented the magnetotelluric results for crustal thickness, inflation-deflation cycles in the Krafla rifting episode, the formation of dikes, magma transport and the process of rifting. Additionally, a simple model of the Krafla volcanic system was explained in along with the relationship between the deformation and the activities in the fissure swarm. The next major and the last event occurred in September 1984. Tryggvason[1986] studied this event in detail using the electronic distance, the optical tilt level and the lake-level measurements. With all these measurements, the magmatic process was well explained. These geodetic measurements related the position of benchmarks from the source of deformation to the magmatic processes occurring beneath this source. After the rifting episode, post-rifting deformations were occurring. These deformations were clearly addressed in Tryggvason[1994]. Various geodetic measurements clearly show these deformations. There was inflation seen until 1989 but the rate of inflation was less than the rate found during the rifting events. Following this, deflation started in 1989. The tilt measurements near the flanks show the decrease in strain in the fissure swarms. Therefore, the post-rifting relaxation was seen in the geodetic measurements. Besides this, space geodetic technique GPS (Global Positioning System) was introduced in 1987 to measure various deformations in North Iceland. Hofton and Foulger[1996] used GPS data (1987-1992) to analyse the horizontal and vertical displacements. There was a decrease in the rate of plate spreading seen from 1987-1990 to 1990-1992. Similarly, the expansion rate was high near the fissure zone but it decreased as the distance increased. Forward modelling was performed with appropriate elastic layer thickness and the viscosity of the visco-elastic layer was devised. The crustal deformation is measured remotely with millimetre accuracy using the InSAR (Interferometric Synthetic Aperture Radar) data. This was a major advance in the field of geodynamics. Sigmundsson et al. used this technique to monitor the deformation in the Krafla region. Subsidence in the centre of Krafla region was in good agreement with the GPS measurements from Hofton and Foulger. The drainage of magma and the solidification were the possible reasons stated in this work. The other major break-through using InSAR was in identifying the wide inflating area in the North of the Krafla region [Dalfsen et al., 2004].

From early 2000 till now, GPS and InSAR turned out to be one of most the important geodetic techniques to measure crustal deformation. They were used individually or in combination to measure the regional deformation. Information on the plate spreading rate, location and the parameters of the plate spreading, local deformation in the Krafla and the Bjarnarflag region and the influence of GIA in North Iceland [Sturkell et al., Pedersen et al., Drouin et al., Auriac et al., Drouin and Sigmundsson] were given by these measurements in aid with suitable modelling. The use of these techniques are explained in detail in their corresponding chapters. Most of the work concentrated on the deformation associated on a larger scale. Drouin et al.[2017] used these techniques in along with levelling to investigate the deformation happening (1993-2015) in the Krafla and the Bjarnarflag region. Individual rates of deformation were found with the average volume decrease of $6.6 * 10^5 m^3/yr$ in the Krafla region and $3.9 * 10^5 m^3/yr$ in the Bjarnarflag region. The complex regional deformation and local deformation sources were well discriminated. Two models were used (1 - single mogi source for the geothermal areas and 2 - array of mogi sources for each borehole). Additionally, the subsidence in the fissure swarm was addressed. The post-rifting adjustment, thermal contraction along the Krafla fissure swarm and crustal weakness were termed to be the possible reasons for the subsidence in the fissure swarm as the models used were not able to differentiate the possible contribution.

1.5. Research Objective

The previous studies confirms the post-rifting subsidence (subsidence in the caldera region and subsidence along the fissure swarm) and human induced local deformation due to the water extraction in the Krafla region. Space and ground geodetic techniques measured these deformations with reasonable accuracy. The

measurements helped in modelling suitable parameters and volume changes to understand the process behind the deformation. A detailed analysis of the subsidence until 2015 in the Krafla and Bjarnarflag region was studied by Drouin et al. with suitable geodetic measurements. Extending this work to 2019 would give a better insight on the long term analysis of the surface deformation after the rifting event. In addition, University of Iceland found a change in the pattern of subsidence to uplift in the Krafla region on July 1 2018. The reason behind the uplift has to be found but the possible reason could be listed as follows: Inflow of the magma into the shallow reservoir or the post-rifting relaxation as seen in the North of the caldera. Therefore, the main objective of this work is to combine the space and ground geodetic techniques to identify the reason behind the sudden change in the deformation pattern and finally obtain an insight on the location, amount and the extent of the deformation happening in the region.

The above mentioned objective can be formulated into the following main research question:

What is the insight that could be gained from the available geodetic data regarding the location, extent (vertical and horizontal) and the gravity change of the recently observed change in the deformation pattern noted in the Krafla region, Iceland ?

The combination of ground geodetic techniques (Gravity and Levelling) and the Space geodetic techniques (GPS and InSAR) would help in finding the deformation pattern over the considered time interval of data. This would help us in finding the good combination of methods that would be suitable for identifying and analysing the long term and short term deformation patterns. This research question can be divided into several questions that would address different sections of the main objective.

- *Can the change in the deformation pattern be located in the InSAR data analysis? If yes, what is the location and the extent (vertical and horizontal) of deformation happening in the region?*
- *Does the levelling data show similar vertical deformation as seen in InSAR ?*
- *Similarly, does the GPS data show similar location, timing and the extent of deformation as seen in InSAR and Levelling ?*
- *Does the change in gravity data help in understanding the underlying process in 2018?*
- *Is the deformation seen in the above observation techniques significant enough to draw a conclusion from it?*
- *Can the Model estimate the location, depth and the volume of the possible sources responsible for the deformation based on the InSAR and GPS data?*

The research is to get an insight on the recent changes in the deformation pattern of the Krafla region. This research is unique because four geodetic techniques (both space and ground geodetic techniques) are used to gain an insight on the deformation. All the techniques are cohesive and the results from these techniques have supported each other. With the available data, an preliminary understanding of the change in deformation has been brought into limelight. The upcoming chapter 2 includes the information on acquiring, processing and interpretation of Levelling data. Chapter 3 includes information on acquiring and processing of PPP data. The results of the Online PPP processing and the PPP results from GAMIT processing is also compared. Additionally, the local coordinates obtained from the PPP processing are used for the further interpretation of deformation and recommendations are given for further improvements. Chapter 4 includes information on acquiring and processing of gravity data, the net gravity data used for the interpretation purpose. Finally, the problems faced in the data processing are explained and recommendations are given. Chapter 5 includes the information on the InSAR data used, steps involved in SNAP and StaMPS processing and the interpretation of these results. In addition, different ways to tune the results are also given. Chapter 6 comprises of information on the GBIS software (Modelling software) that is used, information on the data that is used and the format in which they are ingested into the model. Finally, the results are discussed and improvements that can be done are recommended. Chapter 7 mainly includes summarised conclusion of all the techniques and the research question and the objective are individually answered. Additionally, recommendations are also included in this chapter.

2

Levelling

2.1. Introduction

Levelling is one of the oldest geodetic techniques. This technique calculates the height differences between the two points(benchmarks). The absolute height of the individual points can be calculated if the absolute height of one point and the height difference between the points are known. Else, only the relative height differences can be found.

The measured absolute heights are the orthometric heights (height above the geoid). A short description of the procedure is given in the following to understand how the measurements are taken.

- One levelling instrument and two rods are used for the levelling survey, as seen in figure 2.1. Two backsight (B.S) measurements and two foresight (F.S) measurements are taken between every intermediate benchmark (double levelling) to increase the reliability of the measurements taken and to reduce the observational errors. The tripod with the levelling instrument is placed approximately in the centre between the two rods to reduce the refraction and the curvature effects in the reading. Their corresponding distances are also measured. This procedure is continued from the start of one fixed benchmark to another fixed benchmark.

- The levelling survey must be closed (to start and finish on the same benchmark). Therefore, the levelling is done in both ways, forward and backwards between the two fixed benchmarks to close the loop. The procedure is the same for both the ways.

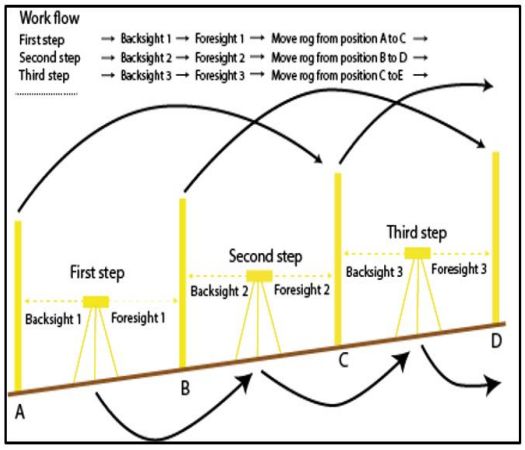

Figure 2.1: A sketch of the procedure in which leveling is done with two rods and one leveling instrument.

A Digital levelling instrument was used in the above procedure of levelling throughout the years. Therefore the standard deviation of the overall levelling is around ±0.4mm/1Km [Algarni and Ali, 1998]. This value

represents the error that can be introduced in the levelling measurements. This value may increase as the measurements can also be affected by external conditions.

The repetition of this procedure at particular time intervals would allow us to determine the change in vertical deformation over the years considered. In our case, we are examining the deformation that has occurred in the recent past in the Krafla region. Measuring absolute deformations cannot be done as the whole region is moving and measurements taken within the region would allow only to find the relative deformation that has occurred over the years. In the past, the Krafla rifting episode (1975-1984) was followed by inflation until 1989. Then there was continuous subsidence in the region. The subsidence rate was higher in the initial years but it started to decay in an exponential manner [de Zeeuw-van Dalfsen et al., 2006]. Therefore, levelling data is useful to get an overview of the trend of the vertical deformation in the recent past.

2.2. Previous Literature on levelling

Initial levelling was carried out in the year 1974 from Mývatn in the south to Krafla in the north. The number of levelling benchmarks was gradually increased depending on the purpose of the measurements. Regular levelling measurements were made since March 1976 (after the initial rifting event), larger parts of the initial levelling line were regularly levelled, generally with one or two months intervals and other stations were levelled with longer intervals. The profiles found on the east of the Mývatn were connected to the benchmark (FM-1) present in the south-west of the lake several times to understand the deformation occurring in the Krafla region 2.2. This procedure was repeated until 1979 and sometimes tilt measurements were used for the interpolation between the levelling data to find the elevation changes in a region [Johnsen et al., 1980].

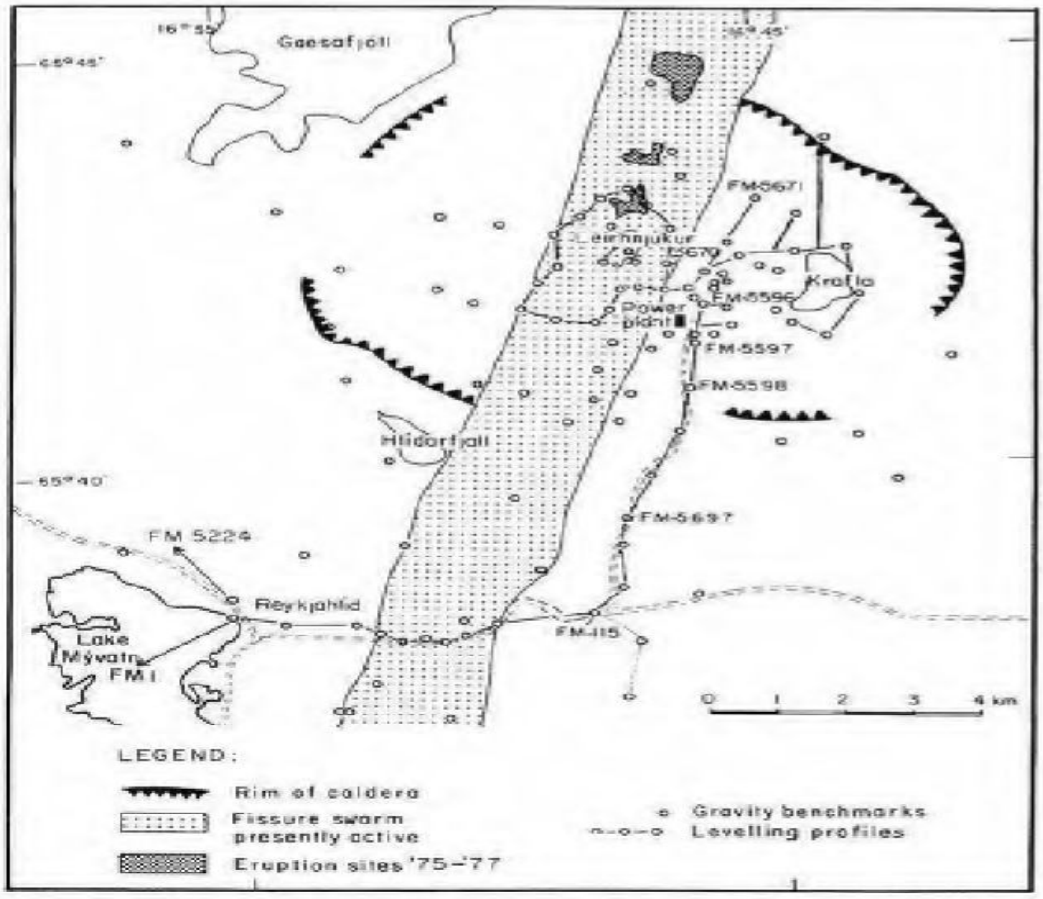

Figure 2.2: Gravity and Levelling benchmarks in the Krafla region [Sigmundsson et al., 1997].

Another set of levelling measurements was carried out on an east-west profile situated to the south of the lake Mývatn. This profile was levelled initially during 1982 and then it was re-levelled in 2000 and 2005 to analyse the post-rifting changes [Sturkell et al., 2008]. Most of the ground displacement data during the rifting

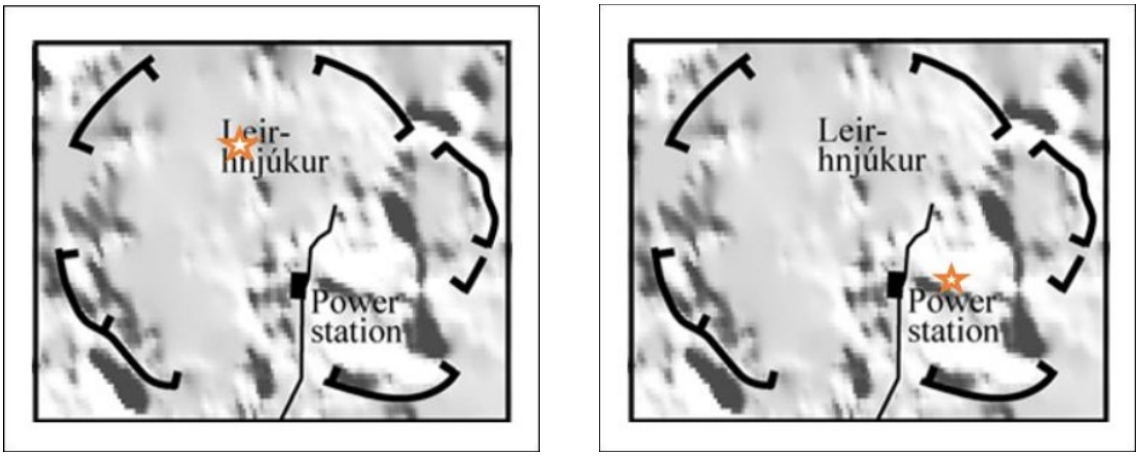

(a) (b)

Figure 2.3: Pictorial representation of the shift in location of maximum subsidence from a) Leirhnjukur (the envisaged location of the Krafla magma chamber) to b) the Krafla power plant. Dashed line shows the caldera boundaries.

and few years of post-rifting was measured using geodimeters (to measure distance), tiltmeters and lake levelling measurements. The next major levelling survey was conducted in the year 1989 by the National energy authority of Iceland. The levelling surveys were then repeated in 1995 and 2000 [Sturkell et al., 2008]. Following this, levelling surveys were conducted in 2005 and 2010 by the company Landsvirkjun [Landsvirkjun, 2006;Landsvirkjun, 2011]. These measurements show consistent subsidence happening in the Krafla region. The locus of the maximum subsidence was near the centre of the Krafla magma chamber (1989-1995). Then the maximum was shifted to south-east (near the Krafla power plant) [Sturkell et al., 2008] (figure: 2.3). The levelling surveys were then conducted by the Delft University of Technology in collaboration with the University of Iceland from 2013 - 2019 to monitor the ground displacements in the Krafla region.

2.3. Description of the data

After 1989, continuous subsidence was recorded in the region. The rate of subsidence was decreasing. This was well recorded and studied until 2008 [Sturkell et al., 2008]. The gradual subsidence began with the decrease of pressure in the magma chambers after the rifting event. This was not the only source of deformation. Plate spreading and extraction of water from the geothermal areas were the other main sources of deformation. Therefore, examining the levelling data over the years (2013-2019) would provide the trend of the vertical deformation occurring in this region in the recent past.

Five levelling lines were established in the past by by the company Landsvirkjun to measure the ground displacements in and around the Krafla region. But, the data measured recently (2013-2019) constitutes of the benchmarks present in the levelling lines 2 and 3. The location of the levelling lines can be seen in the following figure 2.4.

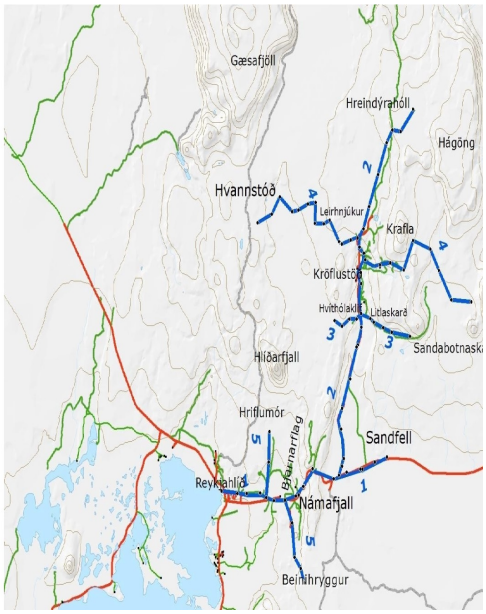

Figure 2.4: Map of the five levelling lines established by the company Landsvirkjun to measure the ground displacements in the Krafla region. (Source:Landsvirkjun, 2011)

The benchmarks measured over the years (2013-2019) by levelling are shown in the following Table 2.5. In figure 2.6, the location of the benchmarks measured are shown. The color in the table 2.5 for each year corresponds to the color shown in the figure 2.6. This indicates the pair of benchmarks chosen for each year.

Benchmarks	2013	2014	2015	2016	2017	2018	2019
KMDE							
KMDD							
L595							
KMDC							
LV056104							
KB11							
L596							
LV056103							
KB8A							
L597							
L598							
OS7161							
OS7162							
LV056103							
SQ18							

Figure 2.5: Benchmarks measured each year at the Krafla region.

(a)

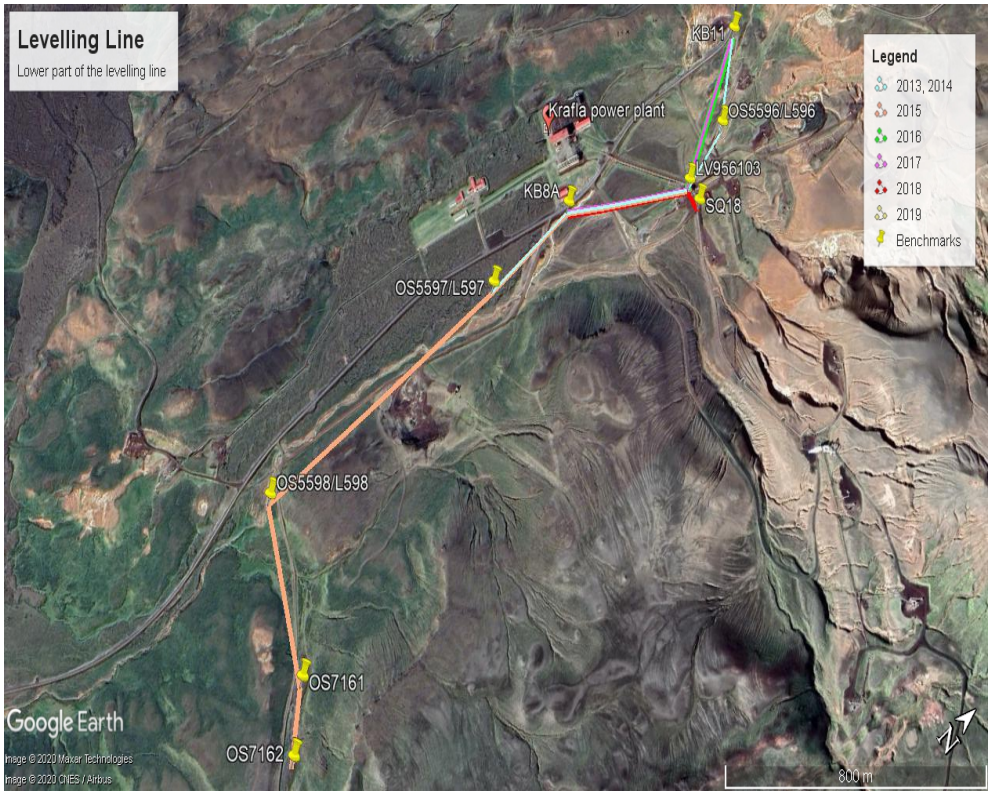

(b)

Figure 2.6: Sub-figure(a) shows the upper part of the levelling line from KMDE (in north) to LV056104. Additionally, the different color lines represent each year in which the levelling was done. The Viti crater marked with black line is shown in the background. Sub-figure(b) represents the lower part of the levelling line from KB11 to OS7162 (in south). Similarly, different color lines represent each year in which the levelling was done. The colors are represented in accordance to the colors shown in Table 2.5. The location of the Krafla power plant is shown in the background. The background image is a Google Earth image of the Krafla region

2.3.1. Formulas used

The levelling calculations are done as follows:

1. Following calculations are done separately for the measurements (Two backsight (B.S), two foresight (F.S) and distance measurements) obtained between intermediate benchmarks for both the forward and backward levelling.

- The height difference is calculated twice as two backsight and foresight measurements are taken. Height Difference (Δh) = $B.S - F.S$
- Error = $(\Delta h)_{i=1} - (\Delta h)_{i=2}$
- Mean = $\frac{(\Delta h)_{i=1}+(\Delta h)_{i=2}}{2}$

2. Sum of Forwards (S.O.F) = $\sum Mean_{forward-levelling}$
3. Sum of Backwards (S.O.B) = $\sum Mean_{backward-levelling}$
4. Height Difference (ΔH) (between two fixed benchmarks) = S.O.F - S.O.B
5. The total distance is calculated by summing up all the distances measured during the forward and backward levelling between two benchmarks. It is expressed Total Distance (T.D) = $\sum Distances$
6. Closing error = $\frac{\Delta H}{T.D}$
7. The Tolerance for higher order of network is $1.5\sqrt{T.D}$ [Johnsen et al., 1980] .In our case the network is much smaller than the higher order networks, therefore the following formula is used: Standard deviation (S.D) = $\sqrt{\frac{T.D}{2}}$

2.4. Results and Analysis

From the benchmarks considered in the previous years, the following figures 2.8a, 2.9a and 2.10a represent the pairs that were chosen for analysis (as data is present in various years to create a time-series). These benchmark pairs are located to the north of the Krafla power plant and to the west of the Viti crater (figure 2.7).These plots represent the change in height differences between the benchmarks analysed over the years. When there is an increase in the height difference between the two benchmarks considered over the years, it represents uplift in the region. It is the vice versa for the subsidence. In addition to this, figure 2.8b, figure 2.9b and figure 2.10b represents the change in trend (Double difference obtained by keeping the starting year as the reference point) of the height difference values along the years. This would give a better interpretation on the vertical changes happening in the region.

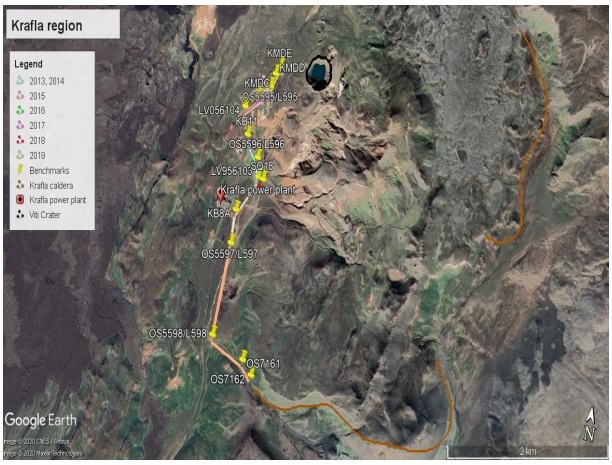

Figure 2.7: The location of the benchmarks chosen for analysis in along with the other benchmarks. In the background, Krafla Caldera is drawn with an orange line. The google image is in the background.

2.4.1. LV956103 - KB8A

In the year 2013 and 2014, the distance measurements were not recorded between the benchmarks and the intermediate points. Therefore the total distance value between LV956103 - KB8A of 2015 was used for both the years. In addition to this, 2005 and 2010 values have been taken from the report provided by the Landsvirkjun company after the completion of the levelling surveys in the year 2005 and 2010 [Landsvirkjun, 2006; [30], 2006]. Both benchmarks have been used in the past, hence a longer time series of height differences is available for this pair which can be seen in the following results. The height differences have been calculated along the years by considering LV956103 as the reference benchmark.

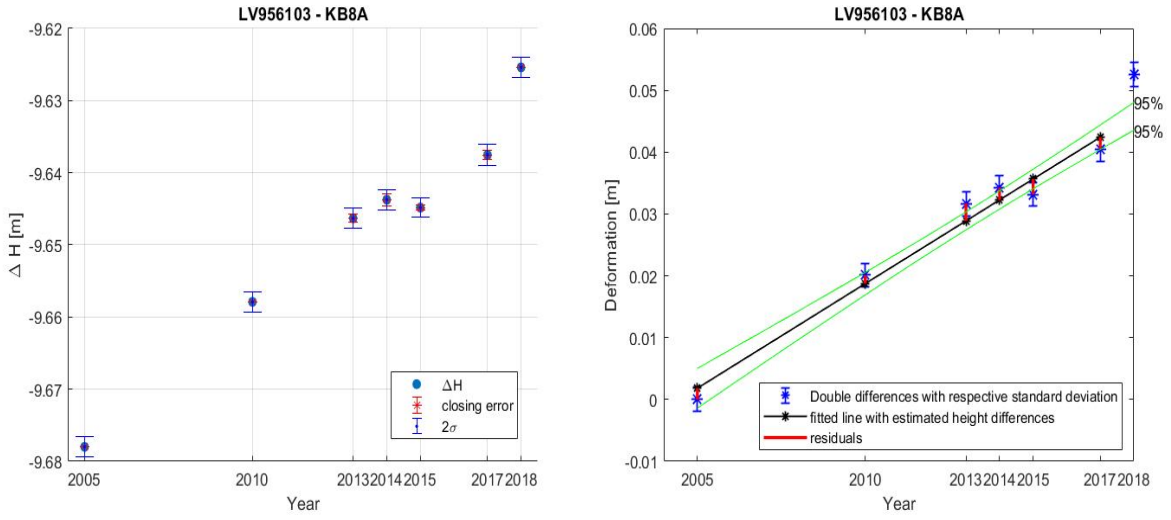

(a) (b)

Figure 2.8: a) Height differences between KB8A - LV956103. b) Trend of the height differences between KB8A - LV956103 (Double Difference)

.

Table 2.1: Calculated Height differences, Closing error, standard deviation , Height differences between the years and the trend between the benchmarks LV956103 - KB8A is displayed

Years	Values (height difference, m)	2 sigma	Closing error (mm/Km)	Differences (mm)	Double differences (mm)	2 sigma - (D.D) (mm)
2005	-9.67800	1.382		0	0	1.954
2010	-9.65790	1.382		20.1	20.1	1.954
2013	-9.64632	1.382	0.579	11.58	31.68	1.954
2014	-9.64374	1.382	0.816	2.58	34.26	1.954
2015	-9.64483	1.382	0.361	-1.09	33.17	1.954
2017	-9.63753	1.426	0.604	7.3	40.47	1.986
2018	-9.62540	1.388	0.017	12.13	52.6	1.958

The values (height difference) column in the table 2.1 represent the height difference between the benchmarks calculated for each year. This is clearly represented in the figure 2.8a. The data for 2005 and 2010 were added to give a longer time series as mentioned before.The standard deviation σ for these years are assumed to have the σ value of 2013. The 2σ column represents 95.4% confidence interval of the height difference value. The differences column represent the change in the height differences between the years. The differences are higher than the 2σ values except in 2014-2015. Therefore, the change caused by the event (2014-2015) is insignificant. The closing error of 2014 is higher than the standard deviation (σ) which shows there might be few mistakes done during the levelling. The double difference (calculated by taking the difference between the ΔH of other years and the reference year (in this case 2005)) seems to be increasing except in 2015. The 2σ for the double difference is calculated in accordance to properties of variance ($Var(X-Y) = Var(X) + Var(Y)$). In addition to this, a linear trend is fitted to the graph representing the double difference values which can be seen in figure 2.8b using least squares. The rate and the intercept of the linear trend are the unknown variables x. The double difference values represent the measurements y. They are related by a linear model. $y = Ax + e$ where $A = \begin{bmatrix} 1 & t \\ 1 & t+i \\ : & : \end{bmatrix}$

The number of rows in the A matrix depends on the number of measurements available. The t in the A matrix represent the epoch at which the measurements were taken and i is the interval between the respective epochs. The Least square solution $\hat{x}$ of x is calculated. Additionally, the $\hat{y}$ and $\hat{e}$ values are calculated [Teunissen and Montenbruck, 2017]. An Overall model test is conducted to see how well the model fits the data. The model is rejected during the testing. Therefore the w-test is performed to find the outliers [Teunissen et al., 2006]. The 2018 value is found to be an outlier. Then by removing it, the linear model is accepted by the overall model test. This clearly shows that there is an significant change in 2018 deviating from the assumed linear trend.

2.4.2. LV056104 - KMDC

The Benchmark KMDC was set up in 2016. From then this pair of benchmarks is measured yearly which can be seen in the following results. The height differences have been calculated along the years by considering LV056104 as the reference benchmark.

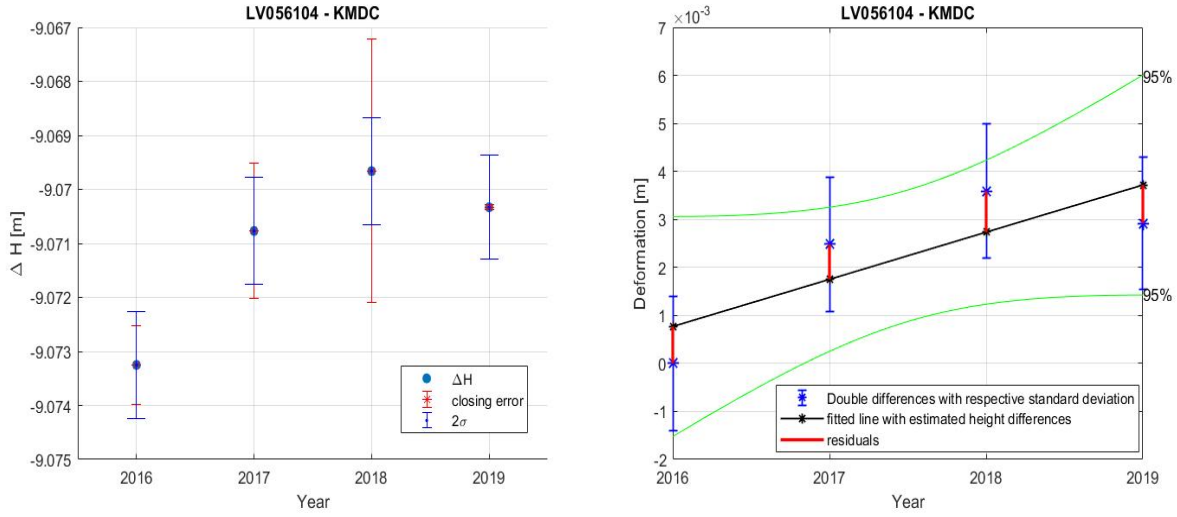

(a) (b)

Figure 2.9: a) Height differences between KMDC - LV056104. b) Trend of the height differences between KMDC - LV056104 (Double Difference)

Table 2.2: Calculated Height differences, Closing error and standard deviation between the benchmarks LV056104 - KMDC

Year	Values (height difference (m))	2 sigma (mm)	closing error(mm/Km)	Differences (mm)	Double Differences (mm)	2 sigma - D.D (mm)
2016	-9.07325	0.988	0.727	0	0	1.398
2017	-9.07077	0.994	1.257	2.48	2.48	1.401
2018	-9.06966	0.986	2.44	1.11	3.59	1.396
2019	-9.07033	0.968	0.043	-0.67	2.92	1.383

The contents of table 2.2 is similar to that of the table 2.1 but the difference is that it is applied to a different set of benchmarks.The differences column represent the change in height differences between the years. The change in 2018-2019 is insignificant as the difference value is less than the 2σ value. The closing error is higher than the σ value except for 2019, which shows there might be few mistakes done in the field measurements. The double difference (calculated by taking the difference between the ΔH of other years and the reference year (in this case 2016)) seems to be increasing in 2017,2018 and then decrease in 2019. The 2σ for the double difference is calculated in accordance to the explanation given in the previous section. In addition to this, a linear trend is fitted to the graph representing the double difference values which can be seen in figure 2.9b using least squares. Similar linear model is constructed with the unknowns (rate and intercept of the linear model) and the measurements (double difference values) as explained in the previous section [Teunissen and Montenbruck, 2017]. An Overall model test is conducted to see how well the model fits the data.The model is accepted by the overall model test [Teunissen et al., 2006]. From the data considered, it clearly proves that there is no significant change that has happened in these years and the changing trend is approximately linear. But the scenario can change if a longer time series is considered which is impossible due to the lack of data. As of now, the change in 2019 seems to be insignificant but this has to investigated with a longer time series. In addition, other techniques can be investigated in regards with the change in height between 2018-2019.

2.4.3. KMDC - L595

As previously mentioned, After the installation of benchmark KMDC in 2016, this pair of benchmarks are measured yearly except in 2018. The height differences have been calculated along the years by considering KMDC as the reference benchmark.

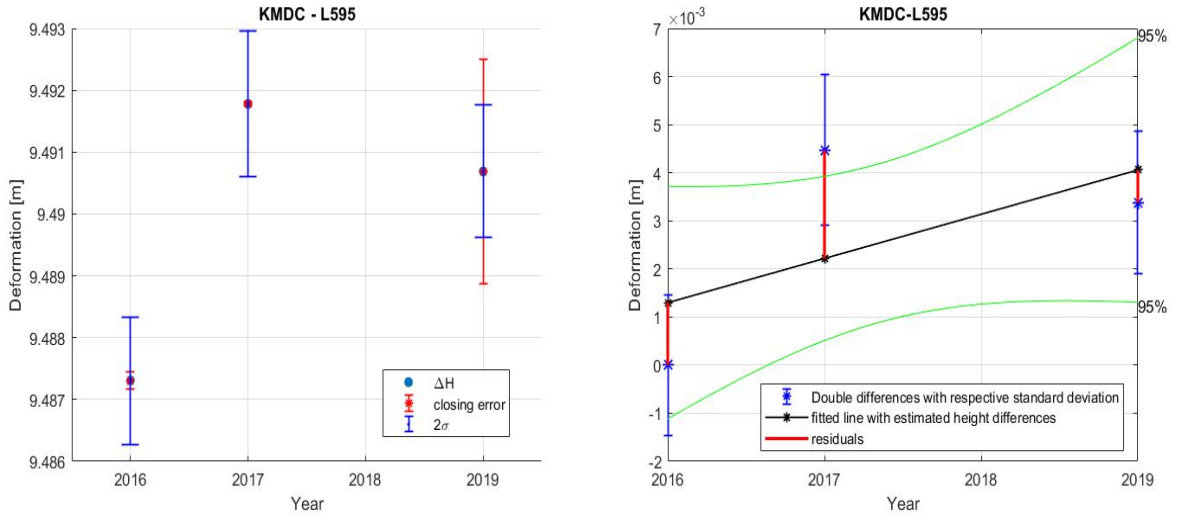

(a) (b)

Figure 2.10: a) Height differences between KMDC - L595. b)Trend of the height differences between KMDC - L595 (Double Difference)

Table 2.3: Calculated Height differences, Closing error and standard deviation between the benchmarks KMDC - L595

Years	Values (height difference (m))	2 sigma (mm)	Closing error (mm/Km)	Differences (mm)	Double Difference (mm)	2 sigma (D.D)(mm)
2016	9.48731	1.03	0.141	0	0	1.457
2017	9.49178	1.178	0.034	4.47	4.47	1.456
2019	9.49069	1.072	1.815	-1.09	3.38	1.487

Similarly, the contents of table 2.3 is similar to the tables of the other benchmark pairs. The same method is applied to a different data set is the difference between the tables. The differences value between 2017-2019 is almost equal to or slightly higher than the 2σ. This leads to difficulty in deciding the significance of the value. The closing error is lower than the σ value except in 2019. Therefore, it shows that there could be some mistakes made during the field measurements. The double differences calculated with respect to 2016 seems to increase in 2017 and then decrease in 2019. The property of variance is then used to calculate the 2σ for the double differences calculated across the years. In addition to this, a linear trend is fitted to the graph representing the double difference values which can be seen in figure 2.10b using least squares. This is carried out to find if any value deviates from the linear trend. Similarly, the unknown estimates are found using the linear model [Teunissen and Montenbruck, 2017]. Therefore, an Overall model test is conducted. The model is accepted and this clearly proves that the changes caused in this area are still insignificant to arrive at a conclusion. With respect to this data, the trend seems to be linear.

2.5. Conclusion

The vertical deformations (height differences between the years) calculated in the previous section are relative and they are not the absolute vertical deformation of the region. In Figure 2.8b, it has to be noted that the increase in height difference between 2017-18 is significant and it is identified as an outlier when the linear trend was fitted to the data. This trend-fitting supports the information that there has been a significant change in height near the benchmark pairs LV956103-KB8A (near the Krafla power plant). The benchmark KB8A is increasing with respect to LV956103 until 2018 (except in 2014-2015). On the other hand, with benchmarks LV056104, KMDC and L595 the change in height is in the opposite direction. From the table 2.2, it is seen that KMDC is increasing with respect to LV056104 in an overall manner (especially from 2016-2018). Similarly, L595 is increasing with respect to KMDC (Table 2.3) in an overall manner (especially from 2016-2017). This pattern forms a subsidence area in the middle between these benchmarks (between KB8A, LV956103 and LV056104, KMDC and L595). Diagrammatic representation of the above explanation is given in the upper part of the figure 2.11b. The uplift is seen on the sides of the subsidence area (near the benchmarks).

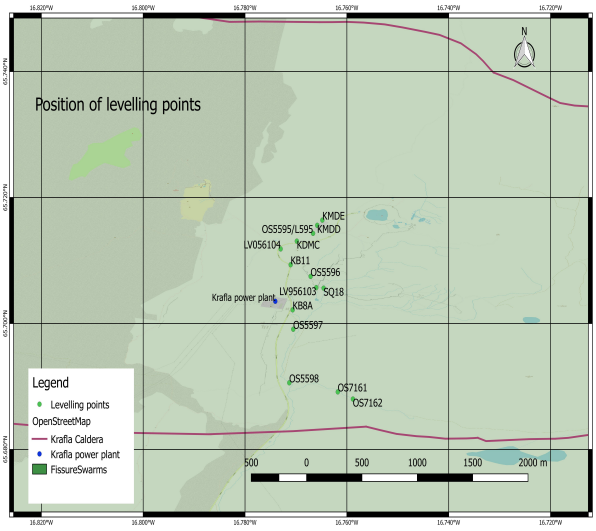

(a) Map displaying the position of the levelling benchmarks

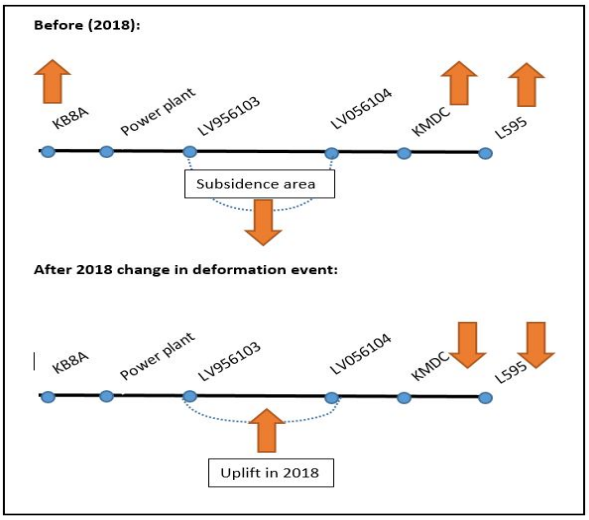

(b) Diagrammatic representation of the deformation happening before the event and after the event.

Figure 2.11: Representing the top view of the position of the benchmarks on the left. Cross section of the change in deformation pattern is displayed on the right side of the figure.

On the other hand, subsidence is seen in 2018-2019 for both the benchmark pairs (LV056104-KMDC and KMDC-L595). The fact that there is a similar trend seen between the benchmark pairs LV056104-KMDC and KMDC-L595 is reinforced by this observation. The uplift in the central part of the caldera (North of the Krafla power plant) is the reason for the subsidence seen in these benchmark pairs LV056104-KMDC and KMDC-L595 in 2018-2019 (figure 2.9b and 2.10b). The diagrammatic representation of the above explanation is seen in the lower part of figure 2.11b. Therefore, from the available levelling data subsidence is seen only in the benchmarks present to the north of the power plant. The uplift in the centre region has caused this subsidence of the benchmarks (north of the power plant). In the next chapters, we will see if these results can be confirmed using data from other techniques.

3

GPS

3.1. Introduction

Global Positioning System (GPS) is one of the space geodetic techniques. It is one of the Global Navigation Satellite Systems (GNSS). GPS helps in real time 3d-positioning. This technique works based on the distance from the receiver (user) to the satellite. Once the distance from the receiver to minimum of 4 satellites are known, then the position of the receiver can be found using the 'trilateration' principle. This technique aids in geodynamic studies. Geodynamic study relies on both the displacement and the displacement time series of a particular region. Study on earthquakes, tectonic plate motion, plate boundary deformation, volcanic deformation, glacial isostatic adjustments, geothermal exploitation are various examples of geodynamic studies. These phenomena cause surface deformation. Geodetic information from GNSS is an ideal tool to understand these processes that are causing this surface deformation [Teunissen and Montenbruck, 2017]. This technique helps in measuring the 3d surface displacements over time. It can provide a time series of the position of sensors with millimetre accuracy. Therefore, GNSS is a powerful tool to monitor surface deformation. The GNSS/GPS data are obtained using different survey styles. The survey styles include continuous (occupation time: several months or more), static (occupation time: several hours to days), rapid static (occupation time: several hours) and kinematic (occupation time: seconds). The continuous and static are mainly used used to monitor crustal deformation. The GNSS data used in this work is obtained using the Precise Point Positioning (PPP) method. It is a self contained static or kinematic positioning method. Information on precise orbits, satellite clocks and observations from single receiver help in identifying the position with few centimetres level of accuracy. Nevertheless, PPP in static mode can give give sub-centimetre accuracy. To achieve 1 cm horizontal accuracy 24h of convergence period is required for PPP [Abou-Galala et al., 2018]. The results from PPP static mode can be post processed. There are many techniques to do the post-processing. The observation period varies from several minutes to several hours. This technique is mostly used to check the existing markers or set up new markers. It can also be used to get the coordinates of the reference receiver during the Post Processed Kinematic (PPK) survey.

3.2. Previous Literature

In 1986, countrywide GPS measurements were taken in Iceland. In 1987, large scale GPS survey was conducted in the Krafla region to to monitor the relaxation process after the Krafla rifting event (1975-1984) and other deformation sources. In the following years, additional surveys were performed in 1990 and 1992 to study the post-rifting relaxation process. The regional plate spreading during this period was identified to be 5.6 cm/year which was three times higher than the normal plate spreading rate. This was attributed to the post-rifting stress relaxation after the diking event [Foulger et al., 1992; Hofton and Foulger, 1996]. On a whole, initial GPS (campaign) measurements were used to account for the plate spreading and the isostatic uplift due to the ice melt [Hofton and Foulger, 1996]. Densely spaced GPS measurements were taken in the Krafla region in 1993, 1994 and 1995. Most of them replaced the Electronic distance (EDM) measurement sites in the geodetic network. In 1995, the first Continuous GPS (CGPS) station was set up in Iceland. Following this the number of CGPS stations was increased to study the plate spreading process occurring in Iceland. Since 2002, the area has been measured on a yearly basis with sparse observations until 2012. In the following years, dense measurements were acquired by the University of Iceland in collaboration with the Delft

University of Technology. However, the sites close to the Bjarnarflag power plant were monitored with GPS in detail from summer 2012, but have been measured every summer since then. The GPS campaigns after 1992 showed the decaying pattern of the horizontal extensional rates [Metzger et al., 2011]. There were various models developed to match the regional deformation data from GPS. In the study conducted by Sturkell et al.(2008), regional and local deformation processes occurring in the Krafla region from 1989-2005 was discussed in detail. The GPS measurements provided additional constraints for the horizontal displacements and revealed similar type of deformation as measured by the other geodetic techniques. Árnadóttir et al. (2009) used the GPS survey measurements and CGPS measurements to construct a kinematic model for the plate-spreading process. Pedersen et al.(2009) used 2D and 3D Finite Element Models to explain the inter-rifting process in NVZ region using GPS and InSAR measurements. Until now, regional deformation at some points due to GIA was measured using GPS measurements. But Auriac et al. (2013) used both the InSAR and GPS data to constrain the uplift of the ground all the way until the edge of the Vatnajökull ice cap. Drouin et al.(2017) found the location, rate of plate spreading axis and the contribution of GIA in Northern part of Iceland using the GPS measurements. Additionally, the work by Drouin et al. used InSAR, GPS and Levelling to observe the regional deformation processes in Krafla and Bjarnarflag area. It included the deflation and inflation due to the magmatic and post-rifting sources, deflation due to the extraction of water in the power plant and the plate spreading signal.

3.3. Description of data

The GNSS data (only GPS or mixed data - GPS and GLObal NAvigation Satellite Systems - GLONASS) measured by University of Iceland and Delft University of Technology is analysed in this work. The data ranges from 2010 to 2019. The benchmarks are measured during the summer of each year. The availability of the data for a particular benchmark can be seen in the following figure 3.1.

Figure 3.1: Represents the availability of data for each benchmark through the years.

The benchmarks chosen in this work cover the Krafla, Bjarnarflag and its outer regions. Therefore, the local and regional deformations can be seen in the GNSS measurements. The location of the benchmarks are shown in the following figure 3.2.

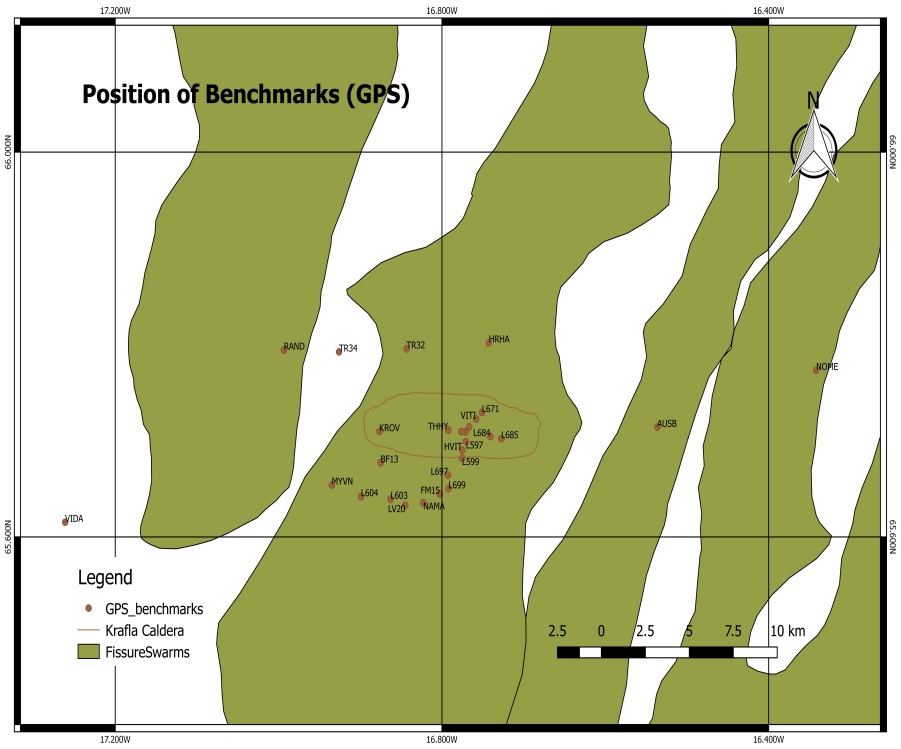

Figure 3.2: Represents the location of the selected benchmarks. The Krafla caldera and the fissure swarms are shown in the background.

3.4. Procedure and processing of data

In this work, the GNSS data is measured using the PPP in static mode as mentioned before. The tripod and tribrach are centered and levelled over the benchmark. The antenna is attached to the tribrach gently and then the antenna cable is connected. The antenna must be oriented to the north and then the height of the antenna is measured twice. The antennas in the survey network must point in the same direction as the antenna's physical centre and electronic centre could differ depending on the factors of satellite geometry. Then the antenna cable is connected to the receiver. The GNSS data is collected at least for two days to ensure the required accuracy. Once the antenna cable is removed from the receiver after the receiver is turned off, the antenna height, levelling and centering has to be measured again to see if there was any disturbances to the site.

The data stored in the receiver is downloaded in proprietary data format (Raw data). Later, the raw data is converted into Receiver Independent Exchange Format (RINEX) files which is used for further processing. There are several services that provide PPP solutions once the RINEX file is submitted. They provide the accurate co-ordinates in reference with the International Terrestrial Reference Frame (ITRF) [40][54]. The CRSS-PPP is one such online processing service that processes the data in static or Kinematic mode. This is operated by NRCAN, Canada [36]. In this work, the RINEX files are submitted to the CRSS-PPP online service in static mode. Then the Ellipsoidal and Cartesian coordinates are obtained with respect to ITRF.

3.5. Results

The Earth is constantly changing and the increase in geodetic data with time helps in updating the ITRF. Therefore, the Cartesian coordinates from the Online PPP processing are with respect to different ITRF. Therefore, all the the results are converted to the latest ITRF(2014) [40]; [54]. This way, the data at the same location but at different epochs can be compared.

Each benchmark has daily PPP solutions (Cartesian coordinates) for individual days as they are recorded at least for two days in a year as mentioned before. These daily online PPP solutions are converted into a single solution using the weighted least squares. Finally, these Cartesian coordinates for each benchmark are converted into local coordinates. On the other hand, GPS data from summer 1997 to 2018 summer has been analysed by the University of Iceland using the GAMIT/GLOBK 10.6 software (source: [13]). The site positions

obtained from this method are with respect to ITRF(2014). The GAMIT solutions of the above-mentioned benchmarks from 2010-2019 are used for the analysis in this work. The main purpose is to compare the results from PPP processing with the solutions from GAMIT processing. To compare these results, the GAMIT daily solutions for the individual days of the benchmark in a year are converted similarly into a single solution for that particular year. Then the site positions in geographic coordinates are converted into local coordinates as it can be compared to the local coordinates obtained from the online PPP processing. The results of the PPP and the GAMIT processing for few benchmarks are shown in the following figures (3.3 - 3.8). The analysis on the results are discussed in the following section. The results of the other benchmarks are in Appendix B. The benchmarks are chosen in a manner that it covers the complete region.

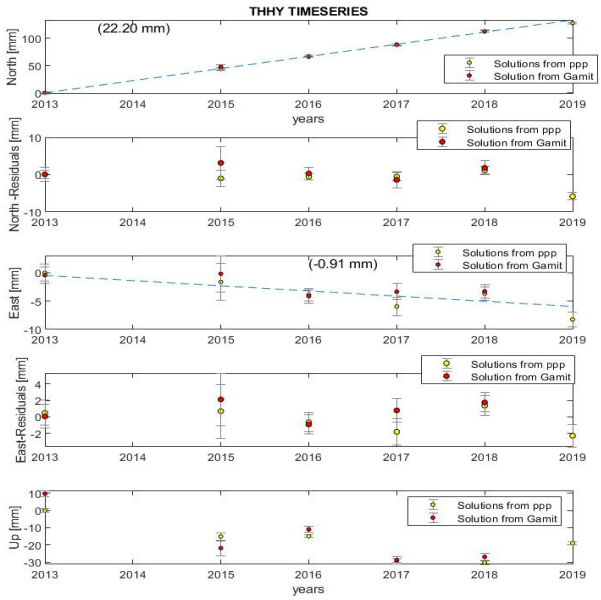

Figure 3.3: Represents the solutions from online PPP processing and GAMIT processing for the benchmark THHY. Average velocity of the fitted linear trend is shown for the North and East displacements.

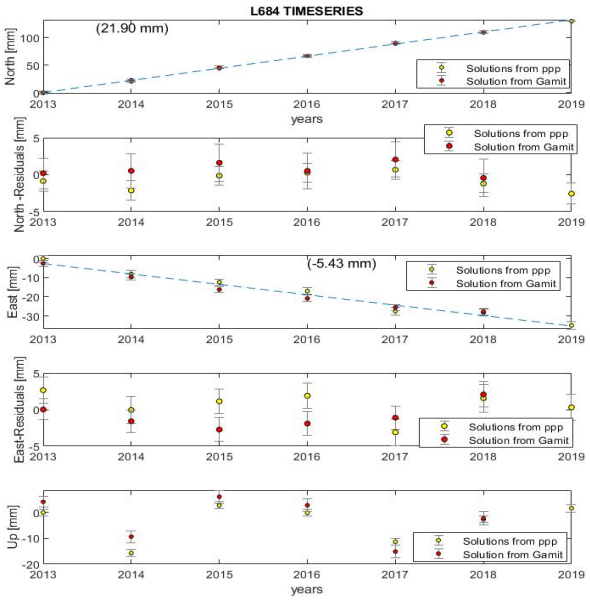

Figure 3.4: Represents the solutions from online PPP processing and GAMIT processing for the benchmark L684. Average velocity of the fitted linear trend is shown for the North and East displacements.

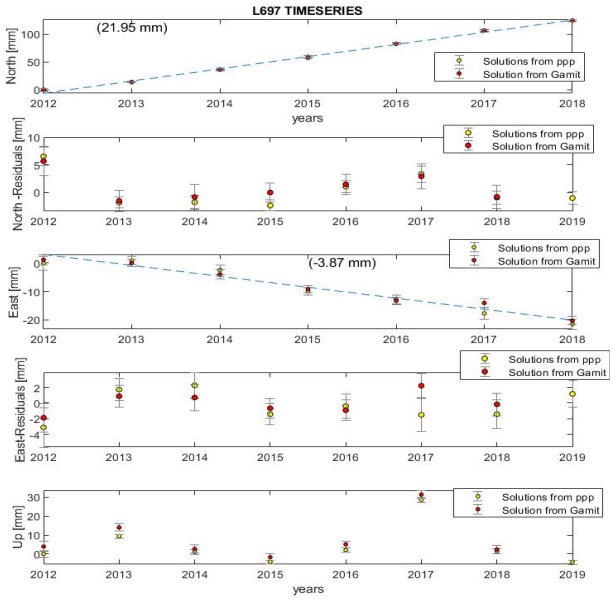

Figure 3.5: Represents the solutions from online PPP processing and GAMIT processing for the benchmark L697. Average velocity of the fitted linear trend is shown for the North and East displacements.

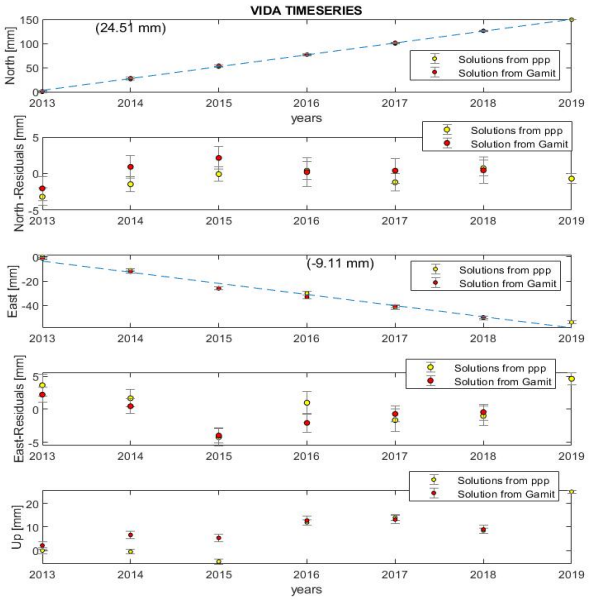

Figure 3.6: Represents the solutions from online PPP processing and GAMIT processing for the benchmark VIDA. Average velocity of the fitted linear trend is shown for the North and East displacements.

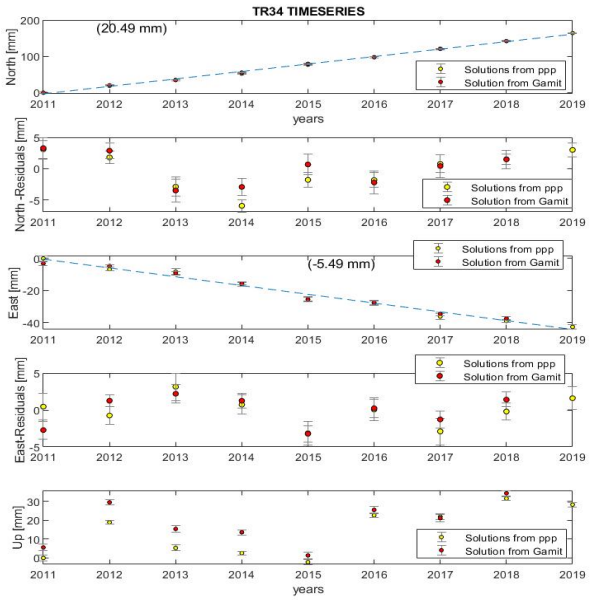

Figure 3.7: Represents the solutions from online PPP processing and GAMIT processing for the benchmark TR34. Average velocity of the fitted linear trend is shown for the North and East displacements.

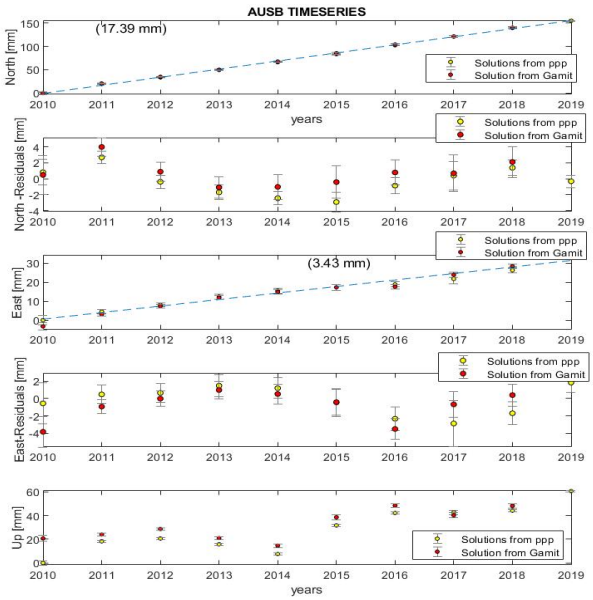

Figure 3.8: Represents the solutions from online PPP processing and GAMIT processing for the benchmark AUSB. Average velocity of the fitted linear trend is shown for the North and East displacements.

3.5.1. Horizontal Displacements

In this work, only the local coordinates from the online PPP solutions are considered for further analysis. The North and East coordinates of all the benchmarks are taken. Average East and North velocities (horizontal velocities) are found by fitting a linear trend to the data of each benchmark. The velocities contain both the regional and the local deformation. To focus on local deformation processes, the regional deformation has to be removed from the data. The plate spreading is the regional deformation process and it has to be removed from the velocities of the benchmarks to identify the local deformation processes.

Initially, the average east velocity of all the benchmarks in the Krafla region (inside the Krafla caldera) as shown in figure 3.9 is taken and the mean is calculated. The similar step is repeated to find the mean north velocity of the Krafla region. This mean horizontal velocity (north and east components) of the region is subtracted from the horizontal velocities of the individual benchmarks in the Krafla region. The similar process is applied to remove the mean horizontal velocity from the Bjarnarflag region (benchmarks outside the Krafla caldera in figure 3.9). Depending on the proximity of the benchmarks in the outer region (benchmarks outside the Krafla and Bjarnarflag region) with respect to the Krafla or Bjarnarflag region, respective mean horizontal velocities are subtracted from the benchmarks in figure 3.10. Additionally, horizontal velocity with respect to the Eurasian plate is shown in the figure 3.11

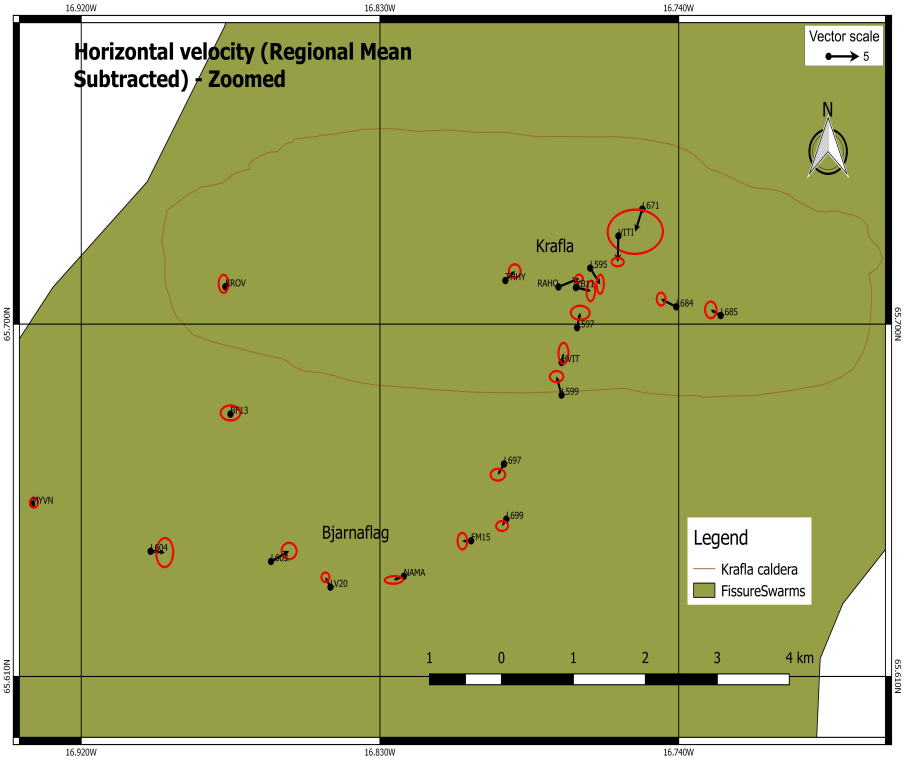

Figure 3.9: Represents the horizontal velocity after subtracting the mean velocity in zoomed version. Benchmarks inside the Krafla caldera belong to the Krafla region and the rest of the benchmarks in the south belong to the Bjarnarflag region. The red ellipses represent one sigma uncertainty. The Krafla caldera and the fissure swarm is shown in the background.

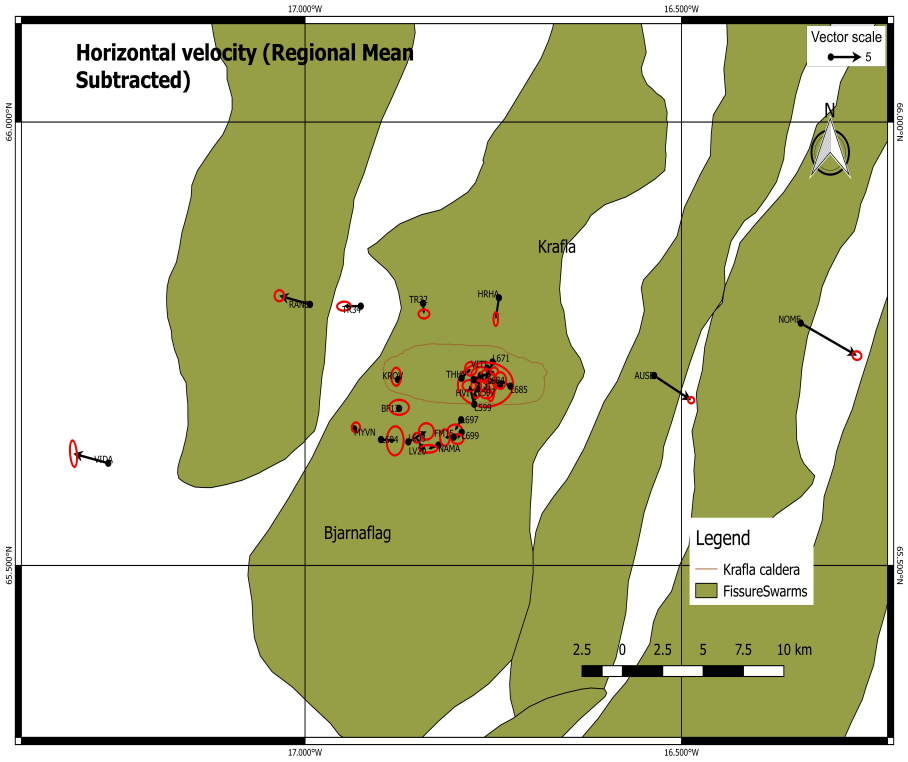

Figure 3.10: Represents the horizontal velocity after subtracting the mean velocity in a larger region. The benchmarks outside the Krafla and Bjarnarflag region is shown. The red ellipses represent one sigma uncertainty. The Krafla caldera and the fissure swarm is shown in the background.

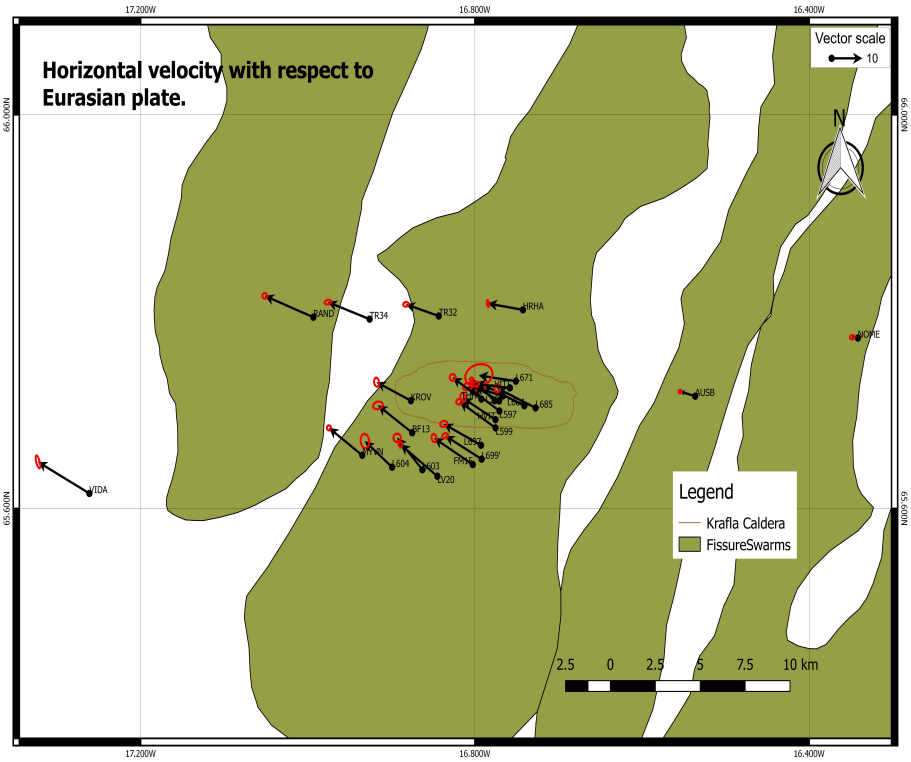

Figure 3.11: Represents the horizontal velocity with respect to the Eurasian plate (ETRF). The Krafla caldera and the fissure swarm is shown in the background.

3.5.2. Vertical Displacements

The local up coordinate is taken into account for all the benchmarks to understand the vertical deformation happening in the region. The local up coordinate represents the difference in height in a year with respect to the first year of the considered data set. Our time of interest lies in the year 2018. Therefore, the height difference between the years 2017-18 and 2018-19 is considered. Additionally, their standard deviation is calculated accordingly. The overall vertical deformation in the region is depicted in the following figure 3.12. This figure is a very rough representation of height change between the years. The vertical height differences between the years shown in the figure 3.12 could have fluctuations between the years due to the errors caused by the antenna height, position or geometry of the satellites, atmospheric disturbances,etc. Therefore, this figure represents the change in deformation pattern but the values in the figure are less reliable.

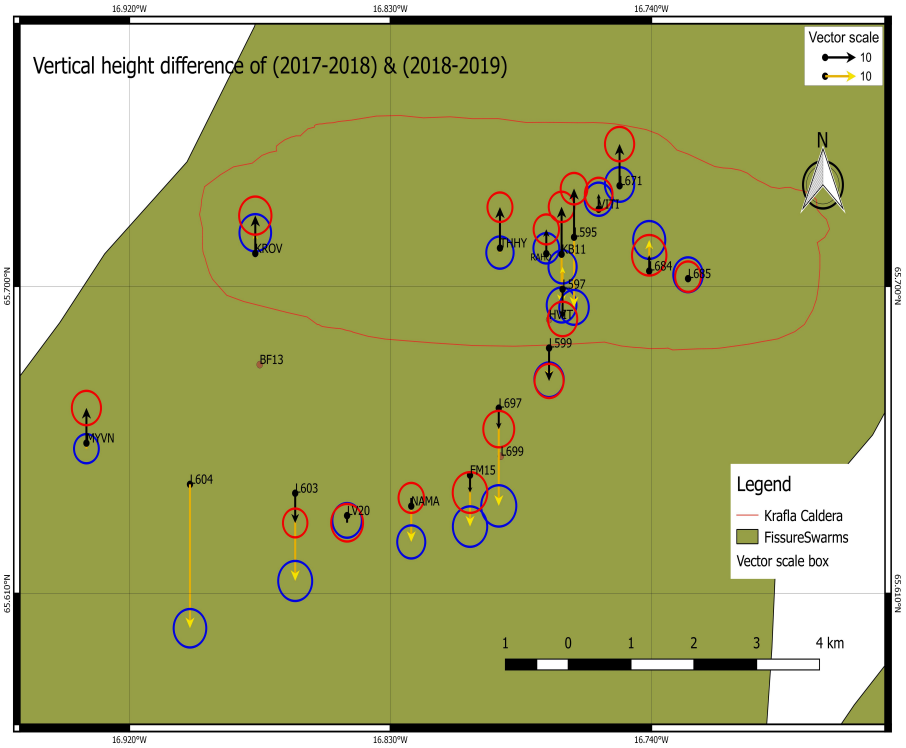

Figure 3.12: Represents the height difference between the years 2017-18 and 2018-2019. The black arrow (vector) and the red circle represent the 2018-19 data. The yellow arrow (vector) and the blue circle represent the 2017-18 data. The error ellipse is circle in this case for each benchmark. It represents the one sigma uncertainty for the height difference.

The benchmarks are analysed individually as following. A trend has to be fitted to each of the benchmarks. Therefore, in common a linear trend is fitted to all the individual benchmarks (time series of local up coordinate for the particular benchmark) using Least squares. The rate and the intercept of the linear trend are the unknown variables x. The double difference values represent the measurements y. They are related by a linear model. The Least square solution $\hat{x}$ of x is calculated using the measurements y and the variance of those measurements Q_{yy}. Additionally, the $\hat{y}$ and $\hat{e}$ values are calculated [Teunissen and Montenbruck, 2006]. An Overall model test is conducted to see how well the model fits the data. The model is rejected during the testing. Therefore the w-test is performed to find the outliers [Teunissen et al., 2006]. The selected important benchmarks are shown in figure 3.13. The results of these selected benchmarks are shown in the following figures(3.14-3.19).The results of the other benchmarks are included in the Appendix-B.

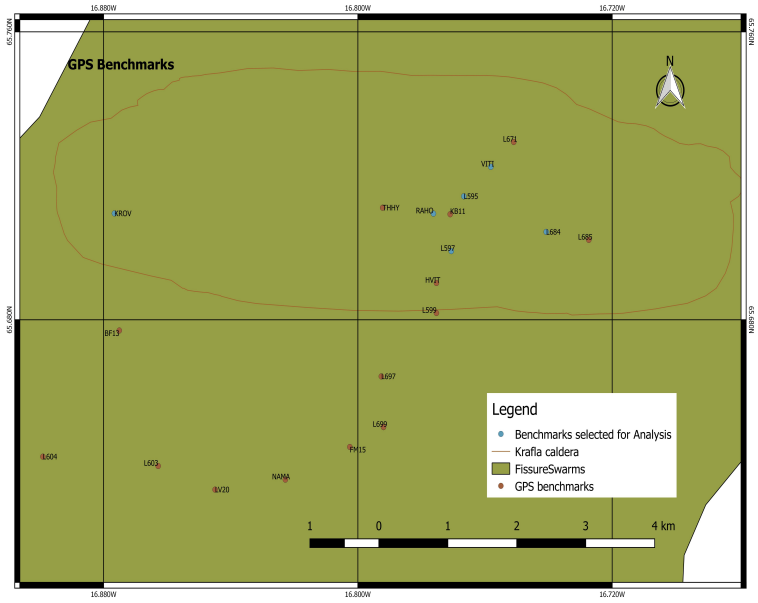

Figure 3.13: Represents the position of the selected benchmarks. The fissure swarm and the Krafla caldera is shown in the background.

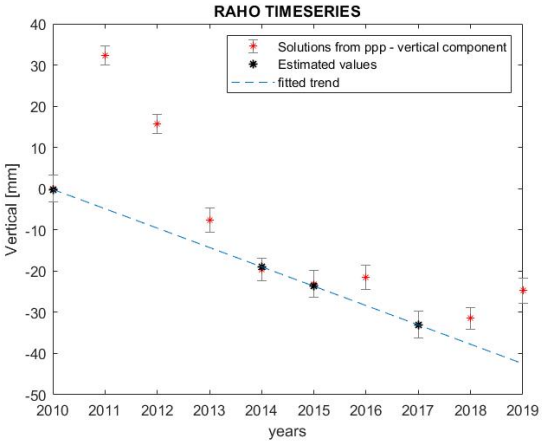

Figure 3.14: Time series of local up coordinate for the benchmark RAHO. The linear trend is fitted to this time series. The black star represents the estimated values and the blue line is the fitted linear trend. The other values with the red star are the outliers.

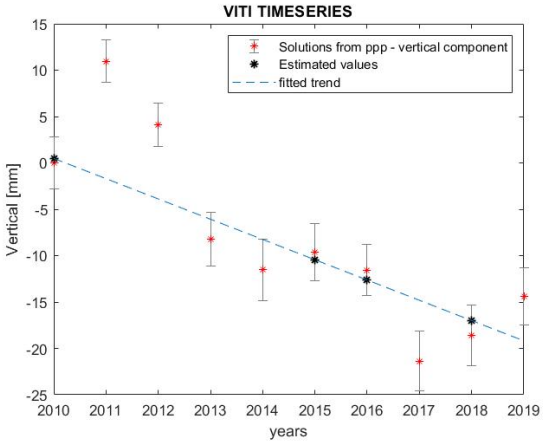

Figure 3.15: Time series of local up coordinate for the benchmark VITI. The linear trend is fitted to this time series. The black star represents the estimated values and the blue line is the fitted linear trend. The other values with the red star are the outliers.

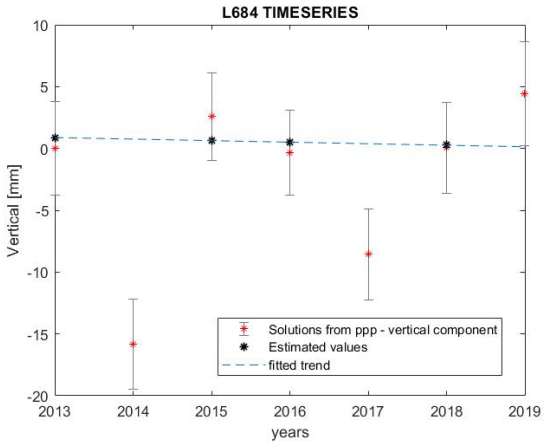

Figure 3.16: Time series of local up coordinate for the benchmark L684. The linear trend is fitted to this time series. The black star represents the estimated values and the blue line is the fitted linear trend. The other values with the red star are the outliers.

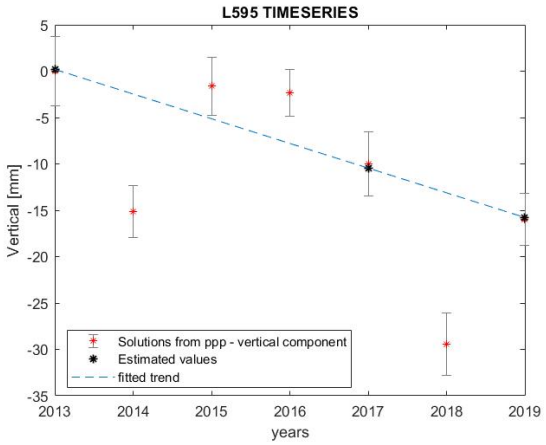

Figure 3.17: Time series of local up coordinate for the benchmark L595. The linear trend is fitted to this time series. The black star represents the estimated values and the blue line is the fitted linear trend. The other values with the red star are the outliers.

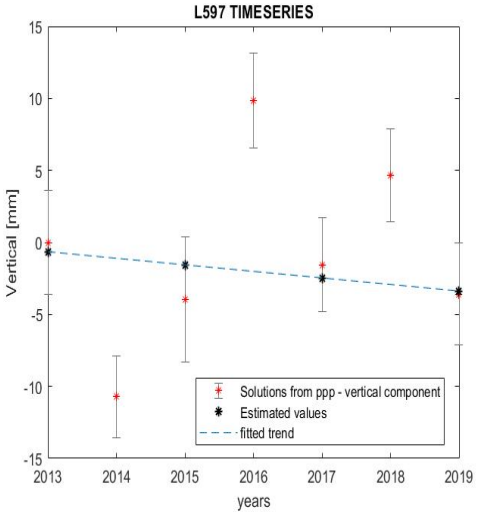

Figure 3.18: Time series of local up coordinate for the benchmark L597. The linear trend is fitted to this time series. The black star represents the estimated values and the blue line is the fitted linear trend. The other values with the red star are the outliers.

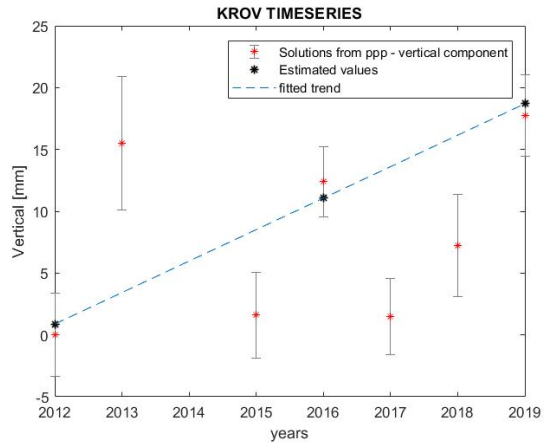

Figure 3.19: Time series of local up coordinate for the benchmark KROV. The linear trend is fitted to this time series. The black star represents the estimated values and the blue line is the fitted linear trend. The other values with the red star are the outliers.

3.6. Analysis of results and discussion

Initially, the online processed PPP results and the results from GAMIT processing were compared (figures(3.3 - 3.8)). The major finding from this comparison is that the local coordinates calculated from each of the method is very similar. There is only a difference of 5-10 mm at the maximum. That could be caused be the few assumptions taken during the processing of data. Horizontal and vertical velocity from the GNSS data can give more insight on the deformation happening in the region. The Regional mean subtracted overall horizontal velocity represents subsidence near the benchmark L595, KB11 as all the horizontal vectors point towards the centre (figure 3.9). The possible reason behind this subsidence could be due to extraction of water from the Krafla power plant or drainage of magma from the shallow chambers. The vertical height difference between the years 2017-18 and 2018-19 provide information on the change in the deformation pattern (figure 3.12). With the available data, few benchmarks (L595 & KB11) present to the north of the power plant show change in deformation pattern. In the year 2018-19, there is some inflation that can be

seen in the benchmarks present to the North and the East of the Krafla power plant. Additionally, the vertical velocity of the benchmarks are analysed individually (figures 3.14-3.19). In an overall manner, it can be seen that the linear trend does not fit the data as most of the points tend to be identified as outliers when this model is fitted. As of now better fitting model is not known but higher degree quadratic equation can be used to fit the model to know the change in pattern of deformation across the years. Additionally, there might be errors in antenna heights that could still invalidate results.

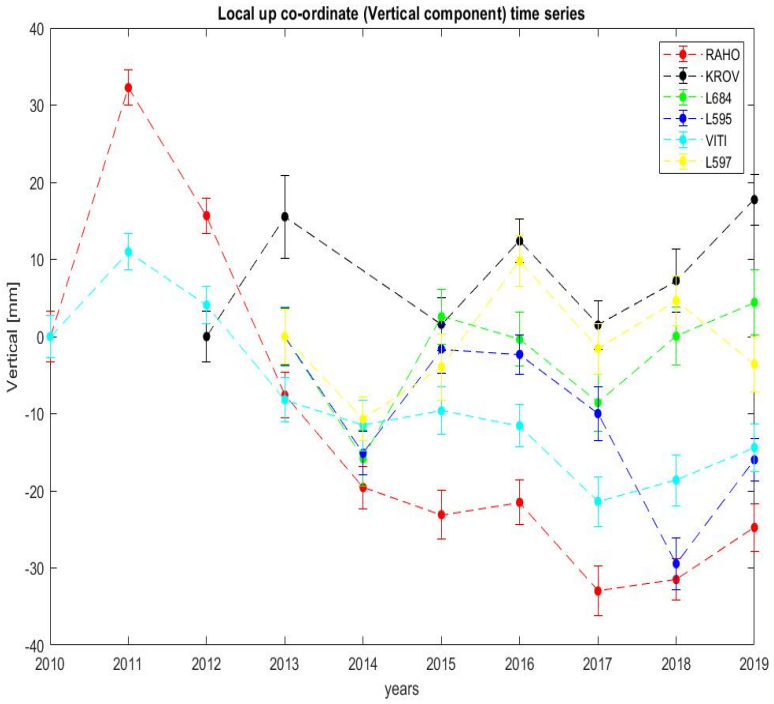

Figure 3.20: Time series of local up-coordinates of the individual benchmarks in the Krafla region

The decreasing trend can be seen in an overall manner (except KROV) and a consistent pattern is observed in almost all the benchmarks between 2012-2019, see figure 3.20. There is subsidence of about 10-20 mm seen in 2014 with respect to the previous year. Again, there is subsidence seen in 2017 with respect to 2016 and in some cases continuing upto 2018 (in the benchmark L595). Then in most of the benchmarks except L597 there is an uplift seen from 2018-2019. Therefore, these are the common changes seen among the benchmarks of the Krafla region. These changes are also seen in the benchmarks (L671, KB11, L685 and THHY) near to the selected ones (figure 3.13). Additionally, similar changes is seen in the time series of KRAC (Continuous GPS benchmark near the Krafla power plant) [Appendix-B, figureB.23].

3.7. Conclusion

The local coordinates obtained from the PPP post-processing (Online) were used in the above analysis. They were similar to the results obtained from the GAMIT processing. Therefore to obtain results in a short time period and accurately, PPP post online processing can be used and it is quite reliable. Besides, regional mean subtracted overall horizontal velocity shows subsidence in the Krafla region. As mentioned before, either the combined effect or individual effect of the power plant or slow drainage of magma may cause this subsidence. The main aim of the work is to find the change in deformation pattern in 2018. The change in pattern is seen in the figure 3.12. There is uplift seen near the North and the East of Krafla power plant. However, the values are less reliable due to the high uncertainty in vertical displacement. This change (uplift) is also seen in the time series of individual benchmarks of the Krafla region (figure 3.20). Therefore, the location of the uplift signal is seen in the Krafla region from the above-used GNSS data. The possible reason behind the uplift could be the migration of magma from the magma chambers or the Post-rifting relaxation signal from the North of the power plant could have caused this inflation [Dalfsen et al., 2004]. Further improvement

can be made by repeating the GNSS campaign every year by measuring the important benchmarks near the deformation region to maintain the continuous time series. Continuous time series with minimum disturbances in PPP measurement would increase the reliability of the data. Additional benchmarks can be added to improve the spatial accuracy and these benchmarks can be measured in the alternate years. Additionally, it would help in better constraining the pattern of the deformation. Now the change in deformation is seen in some benchmarks in 2018, but it would be more safer to draw conclusions and delineate the area when additional benchmarks are present. Current benchmarks are present near the Krafla power plant and along the road near to the power plant. Additional benchmarks can be set up to the east (Possible locations near the magma chamber) and west of the power plant (near L684 and L685 benchmarks). The Continuous GPS data is already available (from KRAC, a CGPS benchmark near the Krafla power plant and BJAC, a CGPS benchmark in the Bjarnarflag region and a CGPS station in Theistareykir (North of the Krafla region)) but additional CGPS station near the benchmark VITI would help in better monitoring of the region.

4

Gravimetry

4.1. Introduction

Measuring gravity helps in understanding the mass changes happening beneath the surface. Gravity data, combined with deformation data measured using other geodetic techniques, are a powerful tool to decipher the process behind mass or density changes happening in a region. This technique is used in many different applications (hydrology, oil/gas exploration, etc.). It is also used in the volcanic areas with volcanic and/or ground deformation. The gravity measurements can identify if the subsurface mass movements are related to the magmatic or hydrothermal activity. Moreover, the gravity data along with the deformation data, helps in constraining the sub-surface density. The gravity data provides the mass change and the deformation data provides the volume change. Together they can be used to constrain the sub-surface density changes. The Krafla region is subject to various processes which could potentially cause mass changes, like water extraction for geothermal use, volcanic unrest and plate movements.

The Mass movements below the surface of the earth will affect the gravitational acceleration on the surface. The gravimeters measure the gravitational acceleration. There are two types of gravimeters: absolute and relative gravimeters. The absolute gravity measurements are measured using absolute gravimeters. Generally, these gravimeters use the falling mass technique. This technique takes several hours to become stable and then several hours to get precise gravity value. But recently, absolute quantum gravimeters [Muquans] have become available. They work based on the principle of falling laser-cooled atoms. These instruments can measure gravity within one hour of setting up with μgal accuracy. Besides absolute gravity measurements, relative gravity measurements using relative gravimeters are useful to study subsurface mass changes. They work on the principle of falling mass technique. In short, the difference in gravitational acceleration between two points (relative gravity) is the principal for the microgravity survey. This technique has higher spatial resolution but lower temporal resolution than absolute measurements. The data analysed in this work were measured using the relative gravimeters(spring-based, Scrintex CG-3 and CG-5). The measurements of gravity are usually depicted in $mGal, (10^{-5} m/s^2)$ or $\mu Gal, (10^{-8} m/s^2)$. The accuracy of these gravimeters varies from $5-10\mu Gal$ [Scrintex]. All the results reported in the following sections are relative gravity measurements.

4.2. Previous Literature on Gravimetry

In the Krafla region, the first geodetic measurements were established in 1938. From then on, the geodetic surveys were repeated in 1965, 1970 and 1975. The gravity measurements were acquired as part of these surveys. On investigating the gravity variations, a continuous increase in gravity was seen in the neovolcanic zone in comparison with the Adjacent Tertiary basaltic zones [Johnsen et al., 1980; Torge, 1981]. The possible reason could be the indication of an imminent rifting event. Following this, a gravity survey was conducted in August 1975 to monitor the gravity changes associated with the utilization of fluids from the drill holes. Then it was repeated in March 1976 after the beginning of the Krafla rifting event. Since then, the region was repeatedly measured with a time interval of 1-2 months. The ground deformation was monitored extensively during the rifting event 1.2.

The vertical changes in the region were mostly measured using the levelling technique. The gravity variations correlate well with the height changes measured inside the Krafla caldera and the active parts of the

fissure swarm. The gravity values calculated from the measured elevation changes using the Bouguer relation were in good agreement to the measured gravity changes. As the Bouguer relation has a good agreement between the gravity and elevation changes, this implies that there is no significant change in density. Therefore, the gravity and ground deformation during 1975-1984 rifting event was due to inflow and outflow of the magma [Rymer et al., 1998; Johnsen et al.1980].

After the Rifting event, a gravity survey was performed every year from 1990 to 1996 (except in 1993) in the caldera region. From the net gravity results (corrected to Bouguer Corrected Free Air Gradient (BCFAG)), gravity decrease was noted above the magma chambers where subsidence was noted in the same time period [Rymer et al., 1998]. On the other hand, an increase in gravity was noted at 1-3 Km from the centre of deformation. The magma drainage quantified from the net gravity decrease was equivalent to the volume change of the magma chamber calculated from the ground deformation measurements. Therefore, the gravity decrease was due to the magma drainage and the gravity increase was due to variation of the steam/water interface or the closure of microfractures in the post-eruptive cooling period [de Zeeuw-van Dalfsen et al., 2006; Rymer et al., 1998]. Following this, the gravity network was remeasured in 1997, 2002 and 2003 [de Zeeuw-van Dalfsen et al., 2006]. The microgravity data was combined with other geodetic techniques (InSAR, GPS and Levelling). The deformation data showed deflation with an exponential rate. Additionally, the net gravity results showed a decrease in gravity at the centre of the caldera region. The decrease in gravity was mainly due to the mass change caused by magmatic process and the water extraction in the Krafla region.

It was also found that the edifice volume changes (sub-surface magma volume changes and magma chamber volume changes) were not significantly influenced by the water extraction as there was a smooth deflation curve observed in 1995-1996 even when the extraction of water was doubled. [de Zeeuw-van Dalfsen et al., 2006]. More recently, the gravity survey was performed by the Delft University of Technology in collaboration with the University of Iceland from 2013 - 2019 to monitor the deformation and mass displacements happening in the Krafla region.

4.3. Description of data

The gravity data used in the following analysis was measured by Delft University (2013-2019). The following figure indicates the years in which that particular benchmark was measured with the type of instrument used for the measurement.

Benchmarks	2013	2014	2015	2016		2017	2018	2019
KB11				CG5 ISOR	CG5 TUD	CG5 TUD	CG5 ISOR	
KROV								CG5 ISOR
L595	CG5 ISOR	CG3 TUD	CG5 ISOR	CG5 ISOR	CG5 TUD			
L597								
L598								
L599								
L604				CG5 ISOR	CG5 TUD			
L684								
L685								
RAHO								
THHY								
VITI								
L603								

Figure 4.1: Represents the benchmarks considered in the Krafla region. The colored boxes represent that the particular benchmark was measured in that year. The color represent the type of instrument used during the survey in that particular year.

The locations of the benchmarks are shown in the Figure 4.2. The benchmarks are spread through out the region. The benchmarks are present near the Krafla power plant, active wells and in the area of the the magma chambers. The above-mentioned are the major causes of possible mass changes beneath the surface. Therefore, the changes beneath the surface can be well monitored by analysing the gravity changes through the time.

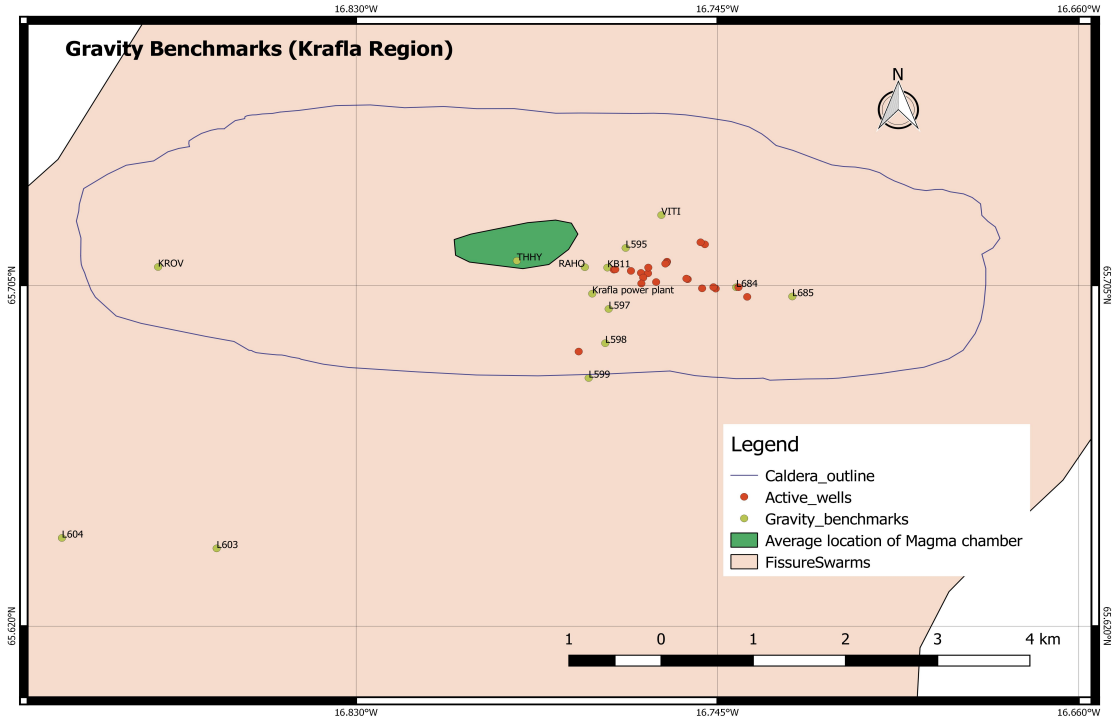

Figure 4.2: Locations of the gravity benchmarks considered for processing. Krafla caldera outline and the fissure swarm are shown in the background. Additionally, the average estimate of the location of magma chamber and the location of active wells are shown.

4.3.1. Procedure and Processing of data

The gravimeter measures the vertical gravity component. At each location, the gravimeter is placed on a mini-tripod centered and levelled over the benchmark. Ten readings of 60 seconds each are taken and they are checked to see if the variation lies within 10 μGal. Else, the procedure is repeated for another set of readings.

The gravity measurements were all taken during the summers of 2013-2019, in the month June. The measurements were taken in a single loop pattern with the same gravimeter. The loop pattern is where one starts by measuring the base station. Then the intermediate stations are measured. At the end, the same base station is measured with which the loop started. The loop pattern allows one to correct the drift endured by the gravimeter.

The raw data from the gravimeter is corrected for the solid, earth and ocean tides. The epoch at which the data was measured, tidal potential and suitable gravimetric factors have been used in the Tidal correction. Then the drift corrected relative gravity values with respect to their base station values are calculated using the following equation:

$$g_{obs} = g_0 + \frac{\Delta g_{drift}}{\Delta t} + \Delta g$$

The g_{obs} are the tide corrected gravity data. The g_0 is the intercept. The second term $\frac{\Delta g_{drift}}{\Delta t}$ represents the drift rate. The third term Δg represents the relative gravity value with respect to the base station. The relative gravity (gravity difference between the benchmark and the base station) of various benchmarks are calculated using the above equation. The standard deviation of the tide corrected gravity values were assumed to be 15 μGal. With the concept of least squares, the relative gravity values and their standard deviation were calculated as well.

The relative gravity values for the benchmarks measured from 2013-2017 are with respect to base station (L604). Then in 2018-2019, relative gravity values are with respect to the base station L595. Luckily, L595 (benchmark) was measured from 2013-2017. Therefore the relative gravity values with respect to L604 can be converted to L595 using the following expression.

$$\Delta g_{BM-L595} = \Delta g_{BM-L604} - \Delta g_{L595-L604}$$

Once uniformity was achieved in the data, the relative gravity values were converted with respect to L603. The benchmark (L603) is considered as it lies outside the region. Therefore, the relative gravity values with respect to L603 gives an better insight on the changes happening in the Krafla region. Additionally, the standard deviation of the drift corrected relative gravity values are changed in accordance.

As previously noted, there is an annual gap between the measurements. The area might have moved up or down between the surveys. Therefore the change in surface height between the gravity surveys must be known. For this, we use ellipsoidal heights calculated from the GPS for each of the benchmarks considered here. The movement causes an effective change in the distance from the centre of the earth that automatically changes the gravity. Therefore the drift corrected relative gravity values are corrected for the vertical displacement using the Free-Air gradient. The theoretical Free-Air Gradient (FAG) is equal to -0.3086 mGal/m. This theoretical average value is always used to do the FAG correction for all the stations in this work. An alternative to this would be to use the actual FAG measured at each benchmark. The actual FAG can be measured by placing the instrument on the ground and then on a high tripod consecutively for three times. In the past, these measurements have been conducted up to 2017 but unstable conditions have often caused unreliable "top" measurements. We consider the maximum error introduced when using the theoretical FAG instead of the measured FAG. The vertical displacement between the years for all the stations (considered) are not more than 40 mm. The FAG values measured in the past varies from 0.280 mGal/m to 0.360 mGal/m. Based on that, the possible change in gravity due to 40mm height change would be between 11.2 and 14.4 μGal. The theoretical value would give 12.3 μGal so the possible error introduced will be 1-2 μGal

$$\Delta g_{fag,corrected} = \Delta g_{BM-L603} - 0.3086 * \Delta h_{BM} - 0.3086 * \Delta h_{L603}$$

$\Delta g_{BM-L603}$ Represent the Drift corrected relative gravity value. Δh_{BM} Represent the change in height at the benchmark between two gravity surveys. Δh_{L603} Represent the change in height at the base station between the two gravity surveys.

4.4. Results and Analysis

Once the FAG corrected relative gravity values have been obtained for the benchmarks along the years, further analysis of these values was done by taking the double differences. When the double difference is calculated for a benchmark through the years, then the change in relative gravity (FAG corrected) can be obtained. A linear trend is fitted through the data (double differences) to find which of these double differences deviate from a linear trend. The results are grouped location-wise, so the similarities and the differences between the nearby stations can be identified.

4.4.1. North of the Krafla power plant

The benchmarks present to the North of the Krafla power plant are VITI, L595 and KB11 (Figure 4.2). The availability of data for these benchmarks can be referred from Figure 4.1. The double differences of these stations and their fitted trends can be seen in the following figures 4.3, 4.4 and 4.5 respectively.

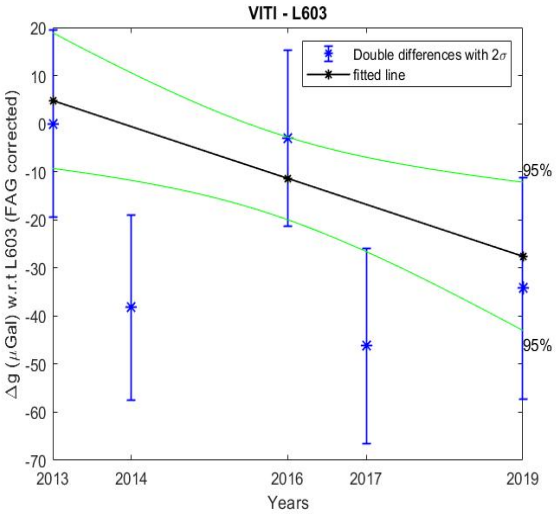

Figure 4.3: Represents the double differences with respect to the year 2013 for Benchmark VITI with 2σ error bars. Additionally, the fitted linear trend for these double differences is shown.

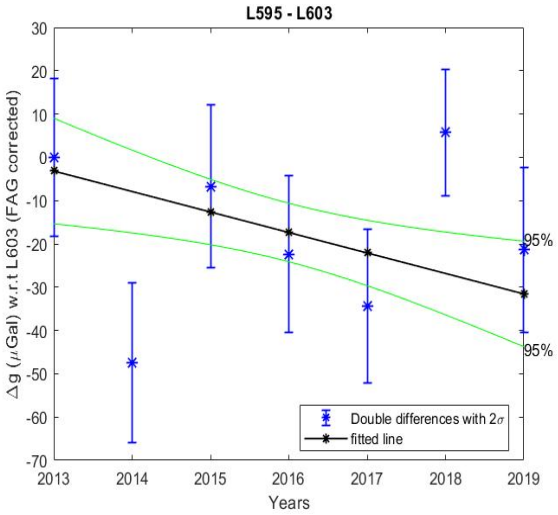

Figure 4.4: Represents the double differences taken with respect to the year 2013 for the Benchmark L595 in along with 2σ error bars.Additionally, the fitted linear trend for these double differences is shown.

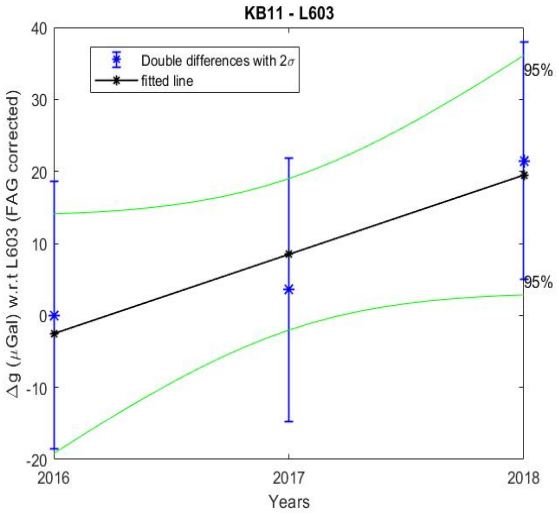

Figure 4.5: Represents the double differences taken with respect to the year 2016 for the Benchmark KB11 in along with 2σ error bars.Additionally, the fitted linear trend for these double differences is shown.

VITI and L595 have longer time series. Overall decrease in linear trend of (app) 30 μGal is seen in both

the benchmarks for the years considered (2013-2019). A significant decrease in net gravity is seen in 2014. Therefore a deviation from the trend is noted. Following this, there is an increase in gravity that is seen from 2017. This pattern is commonly seen in all the three benchmarks. In 2018, significant increase in gravity of (app) 35 μGal is seen in L595. Whereas, there is no 2018 data present in VITI and there is no significant deviations from the increasing linear trend seen in KB11.

4.4.2. South of the Krafla power plant

The benchmarks present to the south of the Krafla power plant are L597, L598 and L599. L597 and L599 are FAG corrected using the GPS data of their respective stations. Due to the lack of GPS data for L598, HVIT (near by benchmark to L598, 170m away) GPS data was used to obtain the net gravity results of L598. There were some assumptions taken behind this step. Extrapolation of GPS data was not done and the standard deviation was not increased. The double differences and the fitted trend for L597, L598 and L599 are shown in the following figures 4.6, 4.7 and 4.8 respectively.

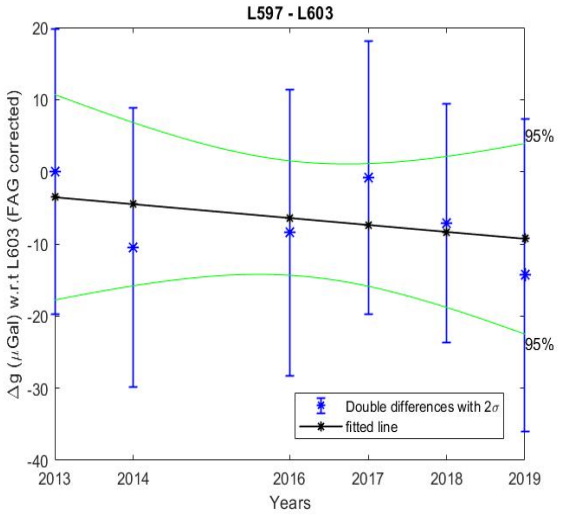

Figure 4.6: Represents the double differences with respect to the year 2013 for Benchmark L597 with 2σ error bars. Additionally, the fitted linear trend for these double differences is shown.

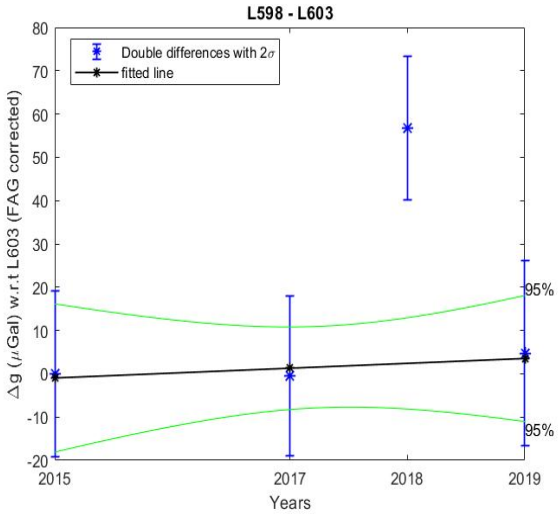

Figure 4.7: Represents the double differences taken with respect to the year 2015 for the Benchmark L598 in along with 2σ error bars. Additionally, the fitted linear trend for these double differences is shown.

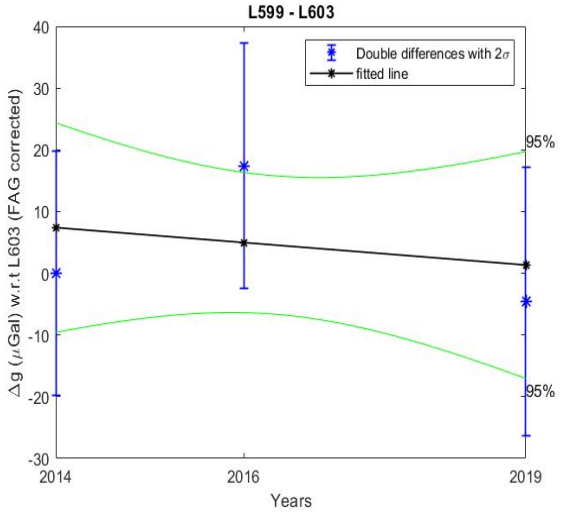

Figure 4.8: Represents the double differences taken with respect to the year 2014 for the Benchmark L599 in along with 2σ error bars.Additionally, the fitted linear trend for these double differences is shown.

Decrease in trend of (app) 5-10 μGal is seen in L597 and L599. The change in net gravity between the years are not significant as they lie within the 95% confidence interval of the overall trend. On other hand, there is a slight increase in trend seen in L598 from 2015-2019. This might change if a longer time series is available. There is a significant increase in net gravity of 55μGal seen in 2017-2018.

4.4.3. East of the Krafla power plant

The benchmarks present to the East of the Krafla power plant are L684 and L685. Both the benchmarks are FAG corrected. The linear trend is fitted only to the double differences of L684 as the availability of the data is less for L685 (only 2018 and 2019). The double differences and fitted linear trend for L684 are shown in figure 4.9. As previously said, the double differences for L685 is shown in figure 4.10.

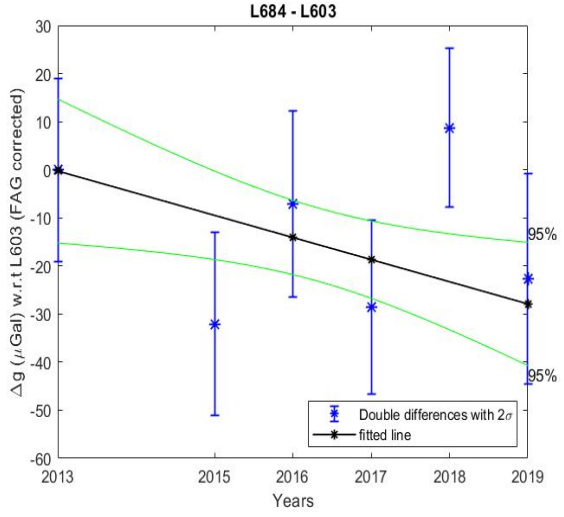

Figure 4.9: Represents the double differences with respect to the year 2013 for Benchmark L684 with 2σ error bars. Additionally, the fitted linear trend for these double differences is shown.

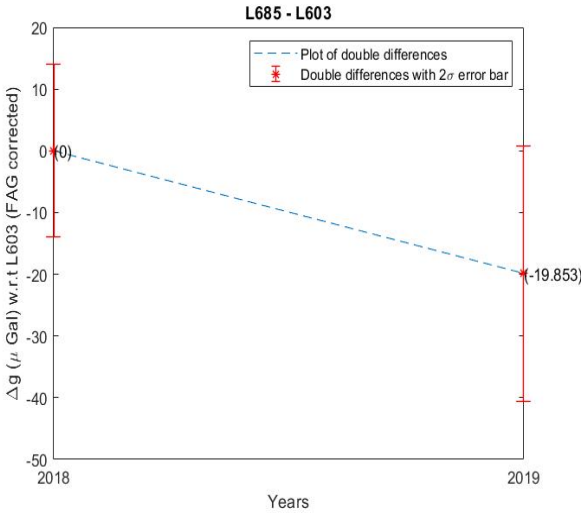

Figure 4.10: Represents the double differences taken with respect to the year 2018 for the Benchmark L685 in along with 2σ error bars.

Considering L684, decrease in linear trend of (app) 20 μGal is seen in the figure 4.9. There is an significant gravity decrease seen in 2015. Additionally, there is a significant increase in gravity of (app) 40 μGal seen in 2018. The term significance is used when the deviation is outside the 95% confidence interval. Between L684 and L685, there is a decrease in gravity of 20 μGal that can be seen from 2018-2019.

4.4.4. West of the Krafla power plant

The benchmarks present in the west of the Krafla power plant are RAHO, THHY and KROV. The FAG correction is done to all the benchmarks. The linear trend is fitted only to the benchmarks RAHO and THHY as the availability of data for KROV is less (only 2018 and 2019). This can be seen in the following figures 4.11, 4.12 and 4.13.

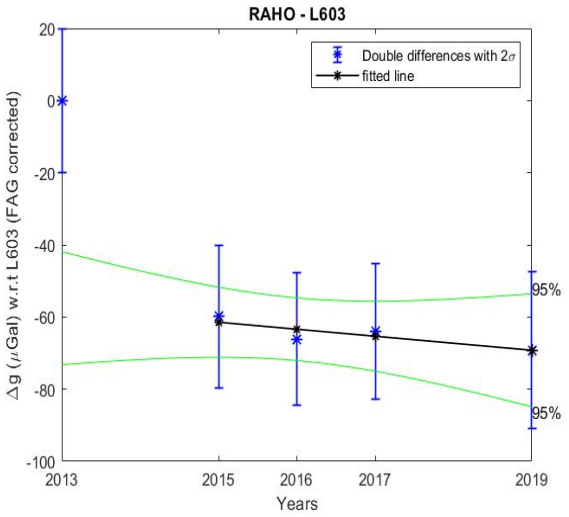

Figure 4.11: Represents the double differences with respect to the year 2013 for Benchmark RAHO with 2σ error bars. Additionally, the fitted linear trend for these double differences is shown.

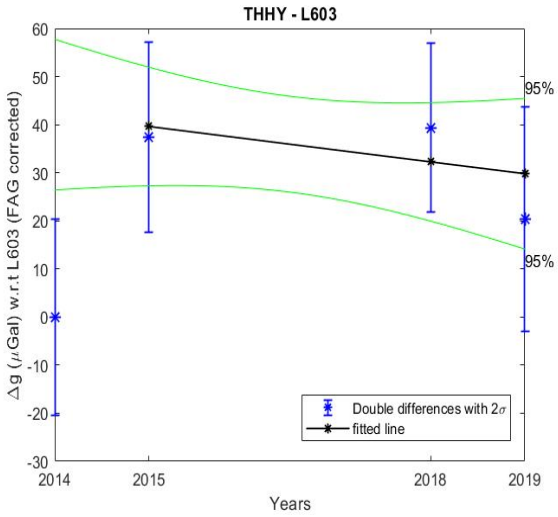

Figure 4.12: Represents the double differences taken with respect to the year 2014 for the Benchmark THHY in along with 2σ error bars.Additionally, the fitted linear trend for these double differences is shown.

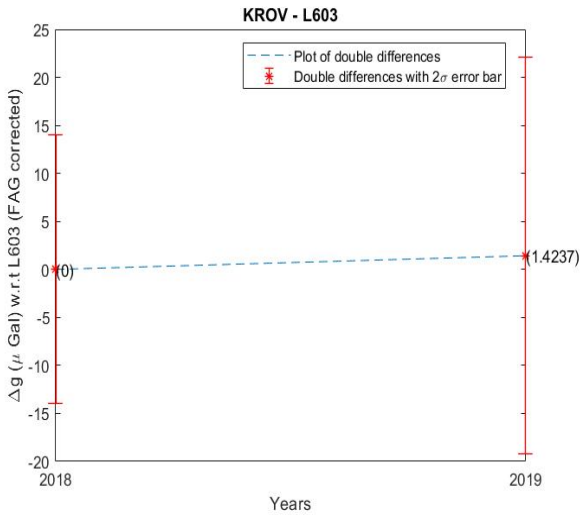

Figure 4.13: Represents the double difference taken with respect to 2018 for the benchmark KROV in along with 2σ error bars.

Decrease in linear trend is seen in RAHO and THHY. On combining the double differences from RAHO and THHY, there is a net gravity decrease that is seen in 2014. This is clearly shown in the figure 4.12. The net gravity at 2014 is 40 μGal lower than the value in 2015. In figure 4.11, there is net gravity decrease seen between 2013-2015 but 2014 data is missing. In both the benchmarks, there is no significant change in gravity between 2015-2019. On the other hand, there is an increase in trend seen in KROV (figure 4.13. Clear conclusions cannot be made as there is an absence of longer time series.

4.5. Discussion

On summing up all the results, overall decrease in trend of net gravity is seen in most of the benchmarks. The overall decrease in net gravity amounts from 10 to 30 μGal in most of the benchmarks. The slow but steady magma drainage could be one of the reasons for this overall decrease in gravity. The other possible reason could be the water extraction or the combined effect of both these factors. The two main deviations from this decreasing linear trend are addressed below and their spatial coverage is shown in the figure 4.14 and figure 4.15.

There is a significant decrease in net gravity seen in 2013-2014 results (figure 4.14). This significant decrease is seen in all the benchmarks except for the ones present in the south of Krafla power plant. This could have been caused due to the mass change that happened in that particular year or due to the use of different gravimeter (CG-3) from other years. The above mentioned could be the possible reasons for the significant decrease in gravity. Additionally, this significant decrease is relatively higher for the benchmarks present near the active wells and the magma chamber. Similar is the case seen in GPS and levelling data. The subsidence is around 15 mm or higher for the benchmarks present near the active wells in case of GPS data. With respect to levelling, there is subsidence seen near the active wells and the Krafla power plant. But in our analysis of gravimetry we use the net gravity results which only depends on the sub-surface mass/density changes. Therefore, I would conclude that most probable reason could be due to the decrease in sub-surface mass (water extraction) in combination with the use of different gravimeter. The actual cause of this event cannot be found due to the limitations in the gravity data.

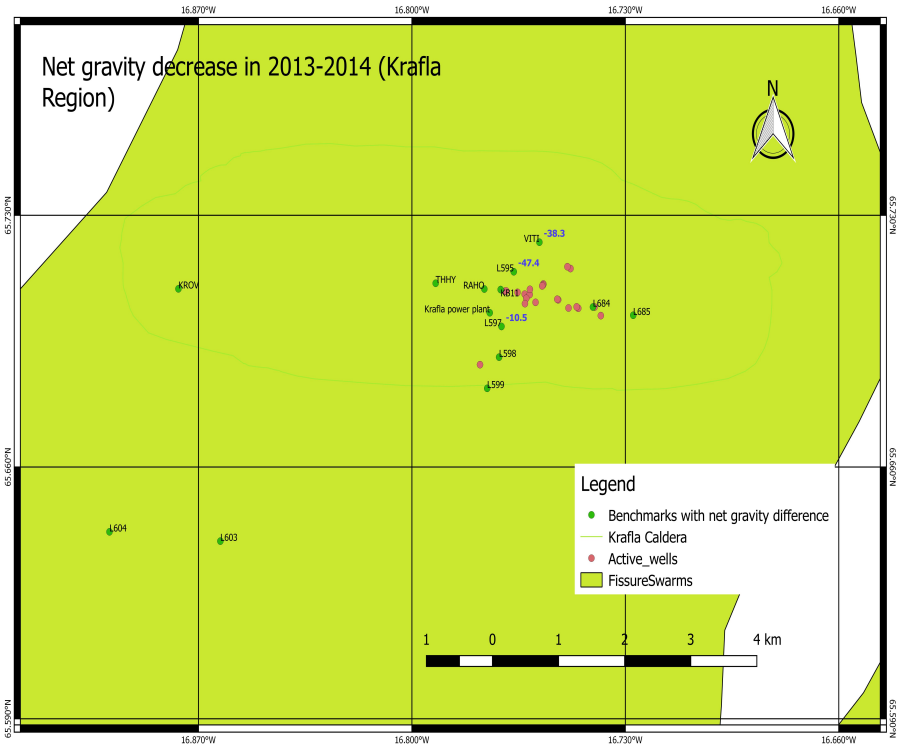

Figure 4.14: Represents the difference in net gravity between 2013-2014

The other result that is seen in an overall manner is the net gravity increase in benchmarks (L684, KB11, L598 and L595) of (approximately) 15-60 μGal in 2017-18 (figure 4.15). But, there is decrease in net gravity seen near the Krafla power plant (L597 benchmark, figure4.15). The water extraction in the Krafla power plant could be possibly influencing the gravity data at L597 more than the other sub-surface mass changing processes. However, there is an increase in gravity seen in the stations around the Krafla power plant. This increase is seen mostly to the north of the power plant from the available data. Therefore, an increase in sub-surface mass/density changes could be the reason for the increase in the net gravity seen among the benchmarks in the north of the power plant. This pattern is visible in the levelling data as well. The possible reasons behind this net gravity increase could be due to the migration of magma from to the shallow magma chamber. The deep magma chamber present in the north of the Krafla power plant [Dalfsen et al., 2004] could be the source for this change in gravity as net gravity increase is seen mostly to the north of the power plant. Additionally, the subsidence in along with the net gravity increase seen in L598 could be due to the solidification of magma along the fissure swarms.

There are certain limitations to this gravity work. First and foremost is the lack of availability of the data to interpret and the gaps in the data for different benchmarks. More errors can be introduced in the data when different instruments and different time instances are used along the years. Additionally, the weather and the person taking the reading could also be one of the reasons to introduce errors in the data. Therefore,

once these limitations are reduced by improved and increased data acquisition better interpretation can potentially be made from gravity data.

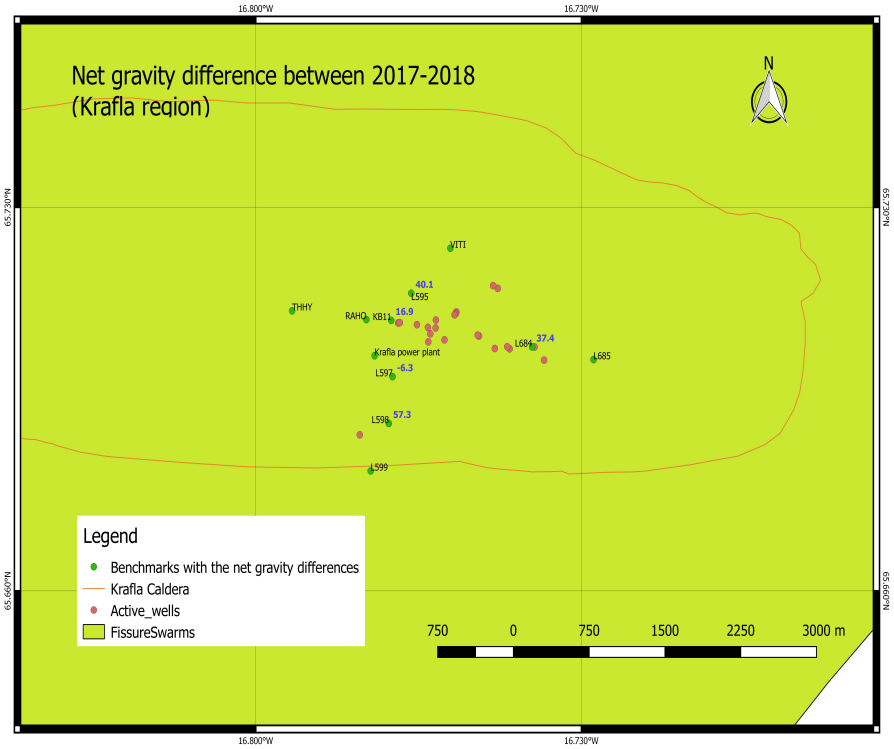

Figure 4.15: Represents the difference in net gravity between 2017-2018

4.6. Conclusion

The main objective was to investigate the underlying process that has caused the change in deformation in 2018. From the net gravity results obtained from this analysis, there is an increase in net gravity seen in 2018 with respect to 2017. This net gravity increase represents a sub-surface mass/density change which suggests the possibility of magma migration or solidification of magma. The increase in gravity is seen in benchmark near to the magma chamber KB11 and also in the benchmarks L595, L684 and L598. At the same time, there is a decrease in net gravity seen in the benchmark L597 (near the Krafla power plant). The water extraction could be possibly influencing this decrease in net gravity change. The increase in gravity seen among the benchmarks in the north of the power plant could be due to the following reasons: Migration of magma into the fissure swarms from the past rifting event, migration of magma into the shallow chamber due to the deep-seated source present in the north of the power plant. The increase in net gravity in L598 could be due to the migration of magma into fissure swarms as it is present away from the source or the solidification of magma present in the fissure swarms. The results can be substantiated if compared with the results fro other geodetic techniques. More stable conclusions cannot be made due to the limitations that exist for this set of gravity data. Therefore to improve the technique, the survey must be conducted regularly and can follow double loop procedures instead of a single loop. A double loop is required to maintain the precision of the values and sudden jumps in the readings can be identified. Specific important benchmarks have to be chosen and they should be measured every year consistently to understand the sub-surface change through the years. Additionally, these benchmarks should be widespread and the length of the measurements can be increased. Last but not least, the use of the base station should be maintained consistently throughout the years.

5

InSAR

5.1. Introduction

The Interferometric Synthetic Aperture Radar (InSAR) technique is a powerful tool to monitor the terrestrial deformations accurately, remotely and cost effectively [McCormack et al., 2011]. This technique is used in this work to find the change in deformation across the years and the extent of the deformation. The surface deformations are well quantified when they have small variation between the neighbouring resolution cells compared to the size of the interferograms else it may seem like an error due to atmosphere or orbital errors [Hanssen, 2001]. This technique has made monitoring possible on a global scale even to the places that are poorly accessed. The major disadvantage of this tool is the inability of this tool to measure the surface deformation on demand of a particular area or at a particular time. Synthetic Aperture Radar (SAR) Satellites move in sun-synchronous Low Earth polar orbits and they have their own repeat period. Therefore, it cannot be manually steered in accordance to the needs. On the other hand, GPS and other ground geodetic techniques have less data compared to InSAR but they are locally focused ground based studies. These data when complemented with InSAR can provide insightful information about the deformation[Pinel et al., 2014].

The data acquired by sentinel-1 constellation is used in this work. The constellation consists of sentinel-1A and sentinel-1B satellites with a short repeat period of 6 days. C-band synthetic Aperture Radar is used in this satellite. The Interferometric Wide (IW) Wide swath is the main acquisition mode. It is done by Terrain Observation with Progressive Scans SAR (TOPSAR) technique. In the ScanSAR technique, the antenna is steered in the range direction but in the TOPSAR technique it is additionally steered in the azimuth direction to reduce the scalloping effect and the Signal to Noise Ratio (SNR) becomes almost constant in the azimuth direction [Meta et al., 2008]. Additionally, the data from sentinel-1 is available in different polarization modes. Polarisation is defined as the direction of travel of the vector tip of the wave.

The conventional InSAR has proven to provide good measurements of surface deformation when the coherence is good. But, at times it fails to produce measurements due to the lack of coherence (spatial and temporal decorrelation) and squint angle errors. The loss of coherence can be due to vegetation, large perpendicular baselines and change in scattering properties over time due to snow cover, etc [Hooper et al., 2004]. The value of a pixel in a Synthetic Aperture Radar (SAR) image is the sum of the scatterers present in that particular pixel. If the scatterers move in different directions to each other during the satellite passes, then the return phase would be in a random manner leading to decorrelation. But if there is one good stable reflector then the variance of the noise due to the background scatterers can be reduced and the underlying deformation signal can be extracted from the small signal (signal from the good reflector) [Hooper et al., 2007]. In this way, the decorrelation of the interferogram can be reduced. This technique is called the Persistent Scatterer Interferometry (PSI). This technique is used in this work to extract the required surface deformation information over a certain period of time. Additionally, the extent to which the deformation has been caused can also be seen.

5.2. Previous Literature

In the early 1990's many studies have shown the application of InSAR in deformation studies. Sigmundsson et al.(1997) was the first to use this technique in the Krafla region. The data from ERS-1 and ERS-2 were used. The Interferograms from 1992-1995 were analysed. The rate of subsidence (increase in range) seen in

the centre of the Krafla area was 2.4cm/year. The rate was seen decreasing. Additionally, subsidence was seen along the rift axis in the Krafla region. The work mainly concentrated on the deformations that has been caused by the post-rifting event. Besides Dalfsen et al.(2004) analysed the interferograms from 1993-1999. The work considered the unaccounted uplift signal to the north of the Krafla power plant in addition to the subsidence seen in the region. The uplift was associated with the accumulation of magma at deeper depths (app) 21 km. The decrease in co-rifting pressure was attributed as one of the reasons for the inflow of magma at deeper depths. Pedersen et al.(2009) used series of InSAR images (1993-2002) along with the GPS data to focus on surface deformation due to plate spreading. Fissure swarms were termed as the weak zones of the plate spreading. It was found that the subsidence (North-south direction) in the North Iceland was associated to the fissure swarms with recent activity. These areas were found to be weaker than the surroundings. Metzger et al.(2011) discuss the use of different combinations of input data to capture the deformation across the Húsavík Flatey fault. InSAR time series (1992-2009) and GPS were considered. The InSAR data provided only the constraints of the volcanic deformation but the GPS data was able to capture the parameters of the fault. Combined InSAR and GPS data were able to find estimates for the fault parameters.

On the other hand, Auriac et al.(2013) was able to provide good constraints on the elastic thickness and viscosity using InSAR time series and GPS data. The permanent scatterers method was used in this work to provide an velocity estimate for each of the Permanent Scatters (PS) points. The uncertainties in the InSAR observation was reduced by the use of these PS points and their corresponding LOS velocities. Therefore, the uplift caused by GIA was well constrained by the InSAR and GPS data together. The regional deformation processes were analysed using the InSAR data (1993- 2015 from different satellites) with other geodetic data by Drouin et al.(2017). The data was processed to obtain the PS scatterers and average velocity field was derived for each time series. Different models were used to fit the deformation results. Not all the the deformations were modelled and there were some residuals left. Therefore the use of other measurements (seismic recordings, borehole recording ,etc.) in along with the deformation measurements was stated for better modelling of the current deformation. In recent times, Drouin and Sigmundsson(2019) used Sentinel-1 images to cover the whole of Iceland. The near-East and near-Up velocities were similar to the general plate spreading model and the GIA model. The residuals depicted that the model requires more information on the rheology of the different rift zones.

5.3. Persistent Scatterer Interferometry

General InSAR techniques extracts information from the phase difference between the two SAR images taken over the similar area but at two different times. The value of each pixel in the image is the sum of the coherent individual scatterers. The Interferometric phase of the pixel m in the interferogram can be shown as follows

$$\phi_{Int} = \phi_m^{def} + \phi_m^{Topo} + \delta\phi_m^{atm} + \Delta\phi_m^{orb} + \phi_m^{noise} + 2.k.\pi \tag{5.1}$$

where ϕ_m^{def} represents the deformation phase component, ϕ_m^{Topo} represents the Topographic phase component and it includes the reference ellipsoid, ϕ_m^{atm} represents atmospheric phase component, $\Delta\phi_m^{orb}$ represents the phase component due to orbital errors, ϕ_m^{noise} represents the noise associated with the scattering, thermal noise, co-registration errors,etc. and $2 \cdot \pi$ is a result of the wrapped nature. The phases are bounded within the range of $(-\pi, \pi]$ and k is an integer value with phase ambiguity [Crosetto et al., 2016]. The conventional Differential Interferometric Synthetic Aperture Radar (DInSAR) comes into play when the Topographic phase component is removed with the help of a Digital Elevation Model (DEM). Finally, it is essential to remove the phase component ϕ_{def} from the rest of the phase components in equation 6.1. This is applied to all the pixels in the image. Thereby the LOS displacement due to the deformation can be obtained. In practice, it is not ideal. There is signal decorrelation in large areas which affects the measurements [Hooper et al., 2004]. Temporal and Spatial decorrelation that affects the phase component ϕ_{noise} [Hanssen, 2001]. Thereby increasing it and making it unsuitable for the purpose. The other major limitation is the atmospheric delay of the signal between the passes.

All these limitations of the conventional InSAR technique are overcome by the Permanent Scatterer technique. To accomplish this, pixels with small ϕ_{noise} must be identified. This is connected to reflectors present in the pixel. If the radar is dominated by strong reflecting object and is constant in time from a pixel. They are called the Permanent Scatterers. On the other hand if the response is constant but from different small scattering objects then they are called the Distributed Scatterers [Crosetto et al., 2016]. Initial methods used

a functional model to identify the PS pixels. The model showed a pattern of deformation with time. Besides, initial set of pixels were chosen based on the amplitude stability. Finally, a pixel was chosen if its phase is similar to the deformation in the assumed model. There were many limitations to this model. Hooper et al.(2004) devised a new method to identify PS pixels. It used spatial correlation of phase measurements rather than the temporal model. Following this, Hooper et al.(2007) improved this method to get accurate estimated displacements. Once the PS pixels are selected the Stanford Method for PS (StaMPS) is used to identify the deformation signal and provide the opportunity to reduce most of the errors caused by orbit or atmosphere.

5.4. Description and processing of data

The Sentinel-1B satellite data is used in this work. The data ranges from 2016-2019 with the months from April to September. Sentinel - 1 is a right looking satellite. Generally, the incidence angle varies from 29°- 46°. When the incidence angle is less in a particular region then it is more sensitive to the vertical motion than to the horizontal movements. With all these aspects, the descending track T9 is used as it covers the the required area (yellow square) as shown in the figure 5.1 and it has a small incidence angle (35° - 38°). The data used in this work is acquired using Interferomteric Wide (IW) swath mode and VV polarisation scheme (transmits and receives vertical waves)[37][35]. The sentinel 1 data is downloaded in the form of Single Look Complex (SLC) products from the site `https://scihub.copernicus.eu`. It can be downloaded using an interactive data viewer or by setting up an automated script as done in this work.

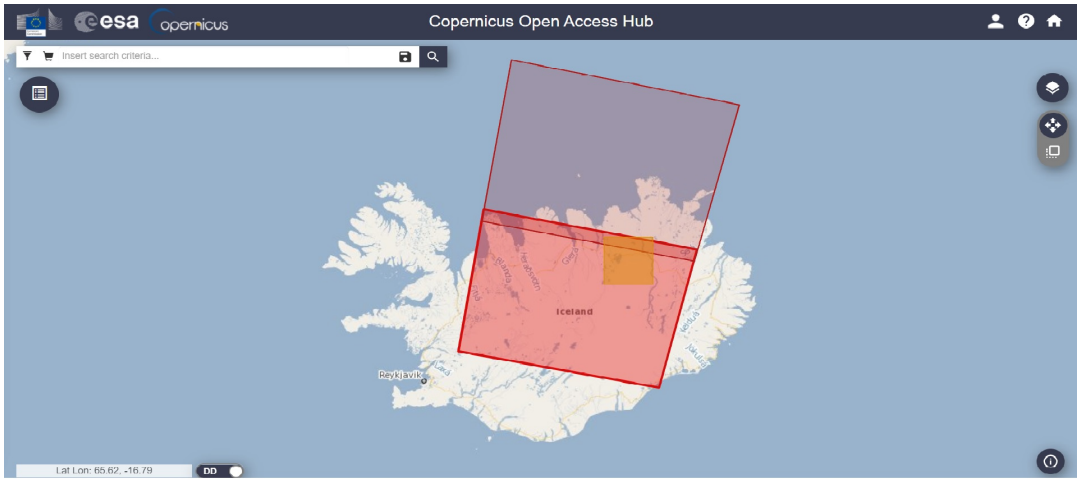

Figure 5.1: Shows the descending track T9. The two red boxes represent the two slices of the same orbit. These are consecutive acquisitions with the same parameters. They are split by ESA to distribute the data more efficiently.

The downloaded SLC data is processed initially using SentiNel Application Platform (SNAP) [42]. It is a toolbox to exploit and extract information by the InSAR processing of the sentinel data. The single master interferograms produced with SNAP are used as input for StaMPS processing which is used for PSI analysis. The steps executed in SNAP and StaMPS are explained elaborately in the Appendix-C.

5.5. Results and Analysis

The results obtained from StaMPS processing is further used to create the following figures: 1) Time series of Unwrapped Interferograms obtained by considering 12th April 2018 as the Master image is attached in appendix-c (figure C.2). 2) Time series of Unwrapped Interferograms corrected for DEM error and Atmosphere and Orbit Error (AOE) of the master and shown in figure 5.2. The sign convention for the phase is normal: When the master predates the slave then positive phase shows movement away from the satellite. The plate boundary movement is seen in all the interferograms in the form of a division across the region (orbital ramp). The Interferograms before the master have opposite sign convention as the slave predates the master. On the other hand the Interferograms after the master have regular sign convention. Therefore, the switch in colors before and after the master is visible.

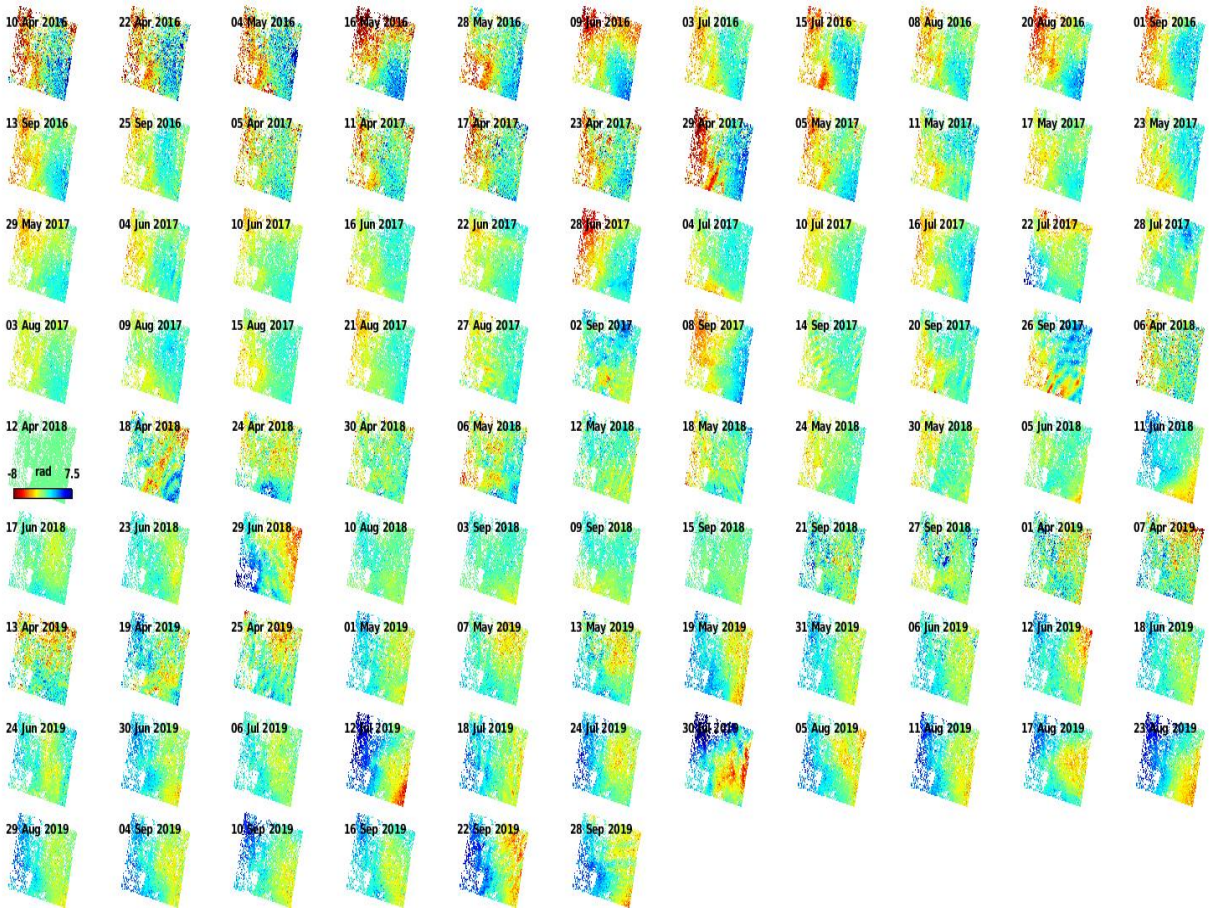

Figure 5.2: Series of Unwrapped Interferograms. The Spatially correlated DEM error and Atmosphere and Orbit Error (AOE) of master are removed from the Unwrapped phase.

The plate boundary deformation is in the form of orbital ramp (orbital error) in this case. Therefore, once the orbital ramp is removed the local deformation can be better accounted [Fattahi and Amelung, 2014]. The complete series of interferograms corrected for all the three errors (DEM error, AOE error of master and the orbital ramp) is attached in appendix-c (figure C.3). Our main area of interest lies in the Krafla region and the time of interest lies in the year 2018. Therefore the following figure 5.3 represents local deformation with the region and time of our interest.

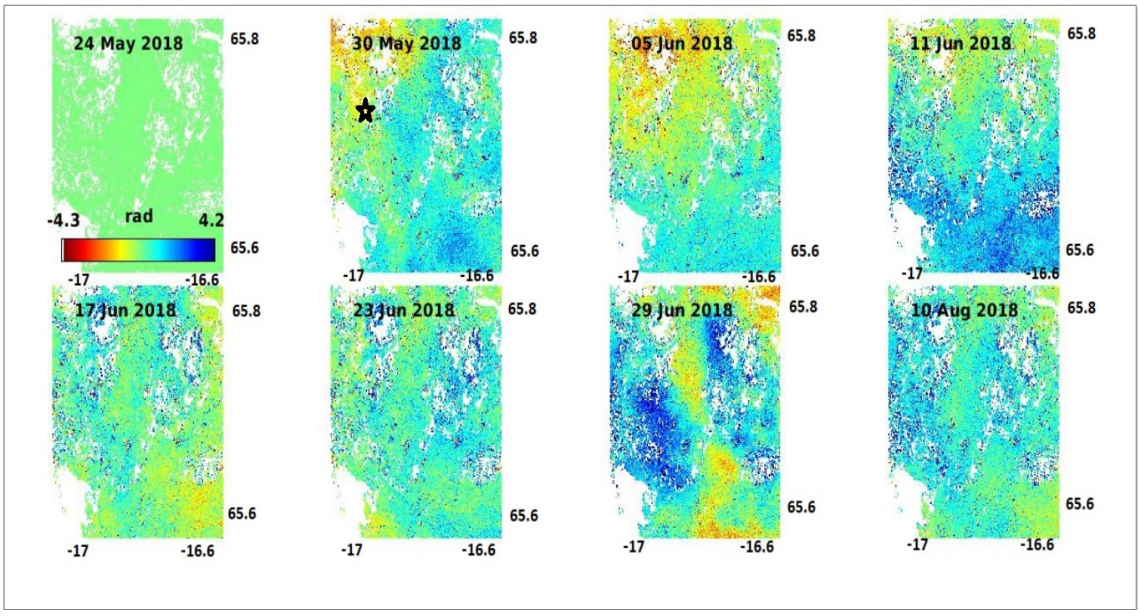

Figure 5.3: Series of Unwrapped Interferograms corrected for DEM error, AOE error of master and orbital error. Local deformation of the Krafla region is shown with respect to 24th May 2018 taken as reference. The white area in the bottom left of each interferogram is Myvatn. Additionally, the black star represents the location of the power plant.

From the above figure 5.3, the local deformation in the Krafla region is seen. The sign convention is normal as described before. In this case, the master predates the slave therefore the negative value indicates uplift in the region. The uplift signal is seen roughly to the north east of the Myvatn lake in 30 May and 05 June 2018 (near the black star in the figure 5.3 which represents Krafla power plant.) In the other interferograms, there is much noise due to atmospheric disturbance. Except, 29th June the noise in other interferograms reduce the information on the underlying deformation. But the speckles due to atmosphere in 29-06-2018 are in a pattern which should not be interpreted for the deformation signal. Therefore, no proper interpretation can be made from these other interferograms.

The line of sight velocity for the complete time series can be seen in the figure 5.4. The velocity values in the figure are with respect to the mean velocity of the whole area considered. The units are in mm/year. The velocity values are corrected for the DEM error and the orbital error. The sign convention for velocity: positive value represents movement towards the satellite and thus uplift. From the figure 5.4, there is still subsidence visible in the Krafla region and along the fissure swarm (near the black circle in the figure 5.4). The big blue blob (North East of the power plant) represents uplift in the region. As the Krafla region and its fissure swarm subsides, the surrounding region tend to show some uplift. Besides, the movement of magma into the lateral sides of the fissure swarm or the uplift due to post-rifting relaxation can cause this uplift in the region.

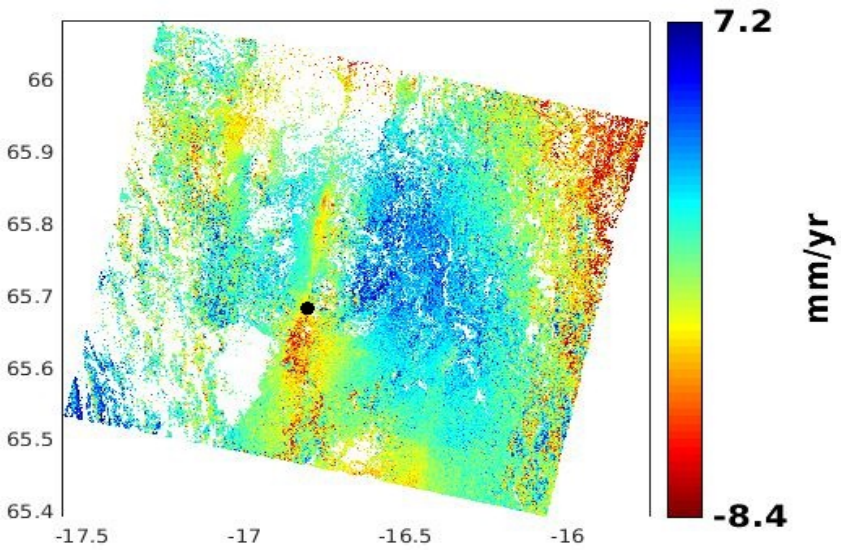

Figure 5.4: Line of sight velocity for the complete time series (2016-2019). Positive values represent uplift in the region and the vice versa for the subsidence. Large white area around -17, 65.6 is lake Myvatn. The black circle represents the Krafla power plant.

Our main focus lies on the uplift event that occurred in summer 2018. Therefore, to envision the change in the deformation pattern due to the event, the line of sight velocity before (2016 - before June 2018) and after the event (June 2018 - 2019) is considered. Accordingly, the interferograms before and after the event are considered and the velocity values for the both the periods are calculated. As mentioned before, the velocity values are corrected for the DEM and the orbital error. This change in deformation pattern is clearly seen from the figures 5.6 and 5.8 for before and after the event. The change from subsidence (in figure 5.6) to the uplift (in figure 5.8) is seen near the Krafla power plant. The uplift is mostly visible to the North of the power plant. Additionally, there is subsidence seen to the South of the power plant.

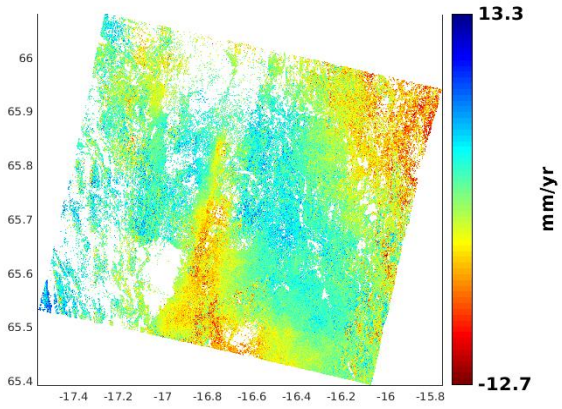

Figure 5.5: Line of sight velocity corrected for DEM and orbital error before the event (10th April 2016 - 24th May 2018) for the complete region.

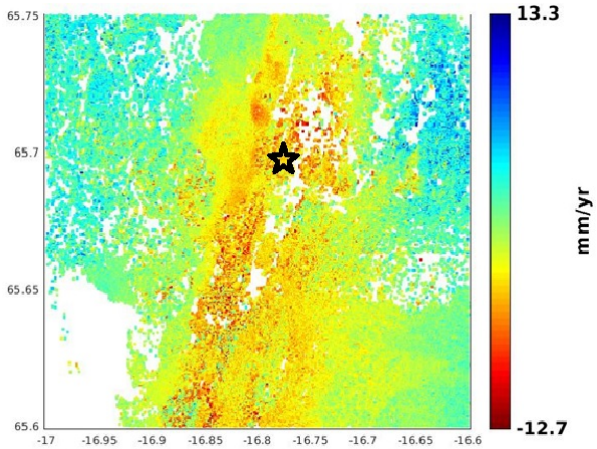

Figure 5.6: Line of sight velocity corrected for DEM and orbital error before the event (10th April 2016 - 24th May 2018) for the required area of interest. The black star represents the location of the Krafla power plant.

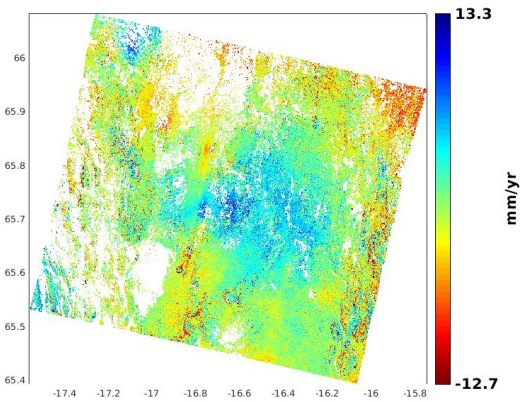

Figure 5.7: Line of sight velocity corrected for DEM and orbital error after the event (30th May 2018 - 28th September 2019) for the complete region.

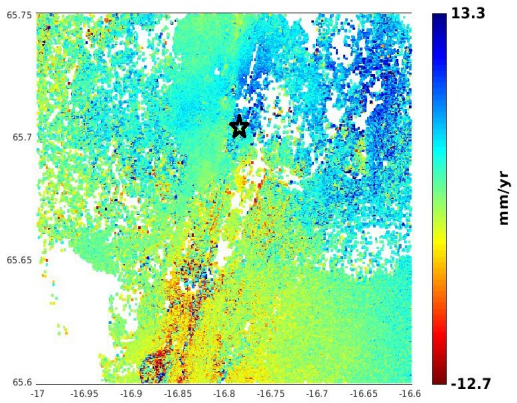

Figure 5.8: Line of sight velocity corrected for DEM and orbital error after the event (30th May 2018 - 28th September 2019) for the required region. The black star represents the location of the Krafla power plant.

5.6. Discussion

The plate spreading is very clear in figure 5.2 when the orbital ramp is not removed. The heading angle of the satellite is 192°(clockwise) and sentinel-1B is a right looking satellite. By this, all the interferograms before master show red for west spreading plate (away from the satellite) and blue for the east spreading plate. Therefore, for all the interferograms after the master image, the pattern is vice-versa. In some interferograms, this signal is not visible due to noise in the master or both master and slave image. Figure 5.3 indicates the uplift near the Krafla power plant on 30-05-2018 and 05-06-2018. The pattern is not clear in the other

interferograms due to the noise. There are speckles in the interferogram of 29-06-2018. Furthermore, the change in deformation pattern is clearly visible in the figures 5.6 and 5.8. These figures represent the line of sight velocity before and after the event. The uplift is seen near the Krafla power plant (black star in the figure 5.8). The uplift is mostly seen to the North, East and West of the power plant.

Similar change in deformation pattern is visible in the work by [Drouin and Sigmundsson] (Personal communication). The result obtained from personal communication is shown in the figure 5.9. The near-East and up velocities before and after the event is shown. These are constructed using the InSAR data from an ascending and descending track while in this InSAR work, only the descending track sentinel data is used. Additionally, KRAC (continuous GPS station of the Krafla region) benchmark is shown in the figure 5.9. This benchmark lies near the Krafla power plant. Therefore, the uplift in 2018 is mostly seen to the North of the this benchmark (from near-Up velocity in figure 5.9). Similarly, the line of sight velocity from the figure 5.8 indicates uplift mostly to the North and slightly to the East and West of the power plant. Therefore, the location of the uplift coincides. The magnitude of the change in deformation cannot be compared between line of sight velocity (from this InSAR work) and near-Up velocity (from Drouin and Sigmundsson) of the region.

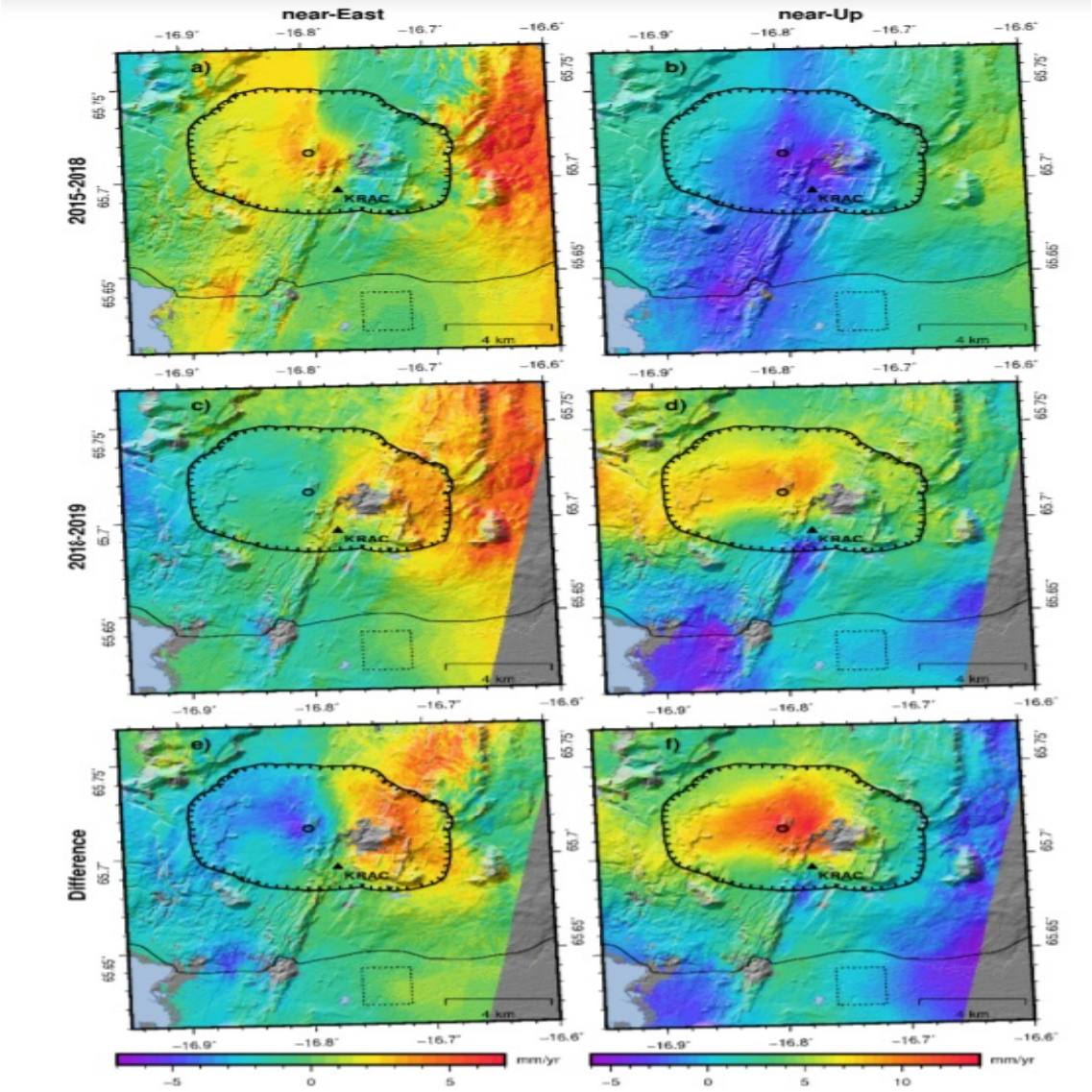

Figure 5.9: Represents the near-East and up velocities before and after the event. Background shows the shaded topography, the Krafla caldera (comb line), road 1 (black line), the Myvatn lake (blue area), the KRAC continuous GNSS site (triangle), the location of the pressure center active during the 1975-1984 Krafla Fires (circle), and the reference area for the velocities (dotted square) (Source: Drouin and Sigmundsson by Personal communication).

5.7. Conclusion

The usage of Persistent Scatterer Interferometry (PSI) has helped in the InSAR processing of this work. The atmospheric noise could have caused decorrelation and loss of measurements. The presence of few scatterers has reduced the surrounding noises. Therefore, the presence of these scatterers has helped in determining the underlying deforming signal. The change in the deformation pattern is visible in 2018. The location of uplift is indicated and validated with the results obtained from Drouin and Sigmundsson. The magnitude of the change in deformation is not compared with the results obtained from Drouin and Sigmundsson. The list of interferograms from figure C.3 have a lot of atmospheric noise. Therefore, it is difficult to conclude the time of change in deformation. Additionally, all the results and conclusions are drawn from the line of sight displacement and velocity. Presence of ascending and descending track for the same area would have solved this issue of converting into near-East and near-Up displacements. Therefore, the following would be recommendations to improve this work.

1. Removal of atmospheric noise
2. Removal of April data (from all the years) in the processing
3. More data from other satellites (For example, data from Terra SAR-X, ALOS-2, COSMO - skymed ,etc.) can be used.
4. Usage of both the ascending and descending track of the same region.

Recommendation 1 is very important as it affects the quality of the results. TRAIN package can be used in along with the StaMPS to remove the atmospheric noise. Recommendation 2 is important as the presence of snow cover in the data could affect the results. But removing the April data and repeating the steps mentioned above in this work would be easier. Similarly, repeating the above steps for both the ascending and descending data can help in deriving the near-East and near-Up displacements. These displacements can give a better understanding on the deformation that is occurring in the region. Finally, depending on the time, its availability and cost data from other satellites can be used for validation. Additionally, the InSAR data can be combined with the other space geodetic data to get a better understanding on the deformation happening in the region. For example, the data from the Continuous GPS stations like KRAC, BJAC, etc. can be used with the InSAR data to understand the deformation in a detailed manner. The local coordinates obtained from the continuous GPS and the near East and Up displacements from InSAR would provide more information on the epoch and accurate extent of the deformation in the region.

6

Modelling

6.1. Introduction

The way of measuring and collecting geodetic data has improved over the last few decades. The geodetic data represents the surface deformation due to various geodynamic processes. The data must be used utmost to understand the process underlying the deformation. Multiple algorithms can model crustal deformation due to earthquakes, volcanic eruptions, water extraction or movement of groundwater. In this work, the change in crustal deformation in the Krafla region is modelled. Mathematical modelling is a great tool to identify and constrain the source parameters (variables that are used to describe the extent and magnitude of the process) by the inversion of geodetic data [Battaglia et al., 2013]. This information is useful to alleviate and forecast the hazards for land use assessment and to assess anthropogenic environmental impact, etc. Many inversion approaches aim at finding the source parameters by reducing the misfit between the observed and the synthesized geodetic data. In truth, there could be a wide range of values for the source parameters to explain the observation. But there is a requirement of knowing reliable source parameters to understand the underlying process and to explain the observations. The commonly used inversion approaches (Simulated annealing, generic algorithm, etc.) do not give the uncertainty associated with the source parameters completely, thereby making it less reliable. In our case, Bayesian inversion approach is used. This method considers the uncertainty related to the data which is used in the formulation of the Posterior Probability Density Function (PDF) of the source parameters. Therefore by finding the maximum of the probability, the optimal set of source parameters is found. This finding satisfies the main aim of characterization of the source deformation parameters by the inversion of geodetic data.

Several models have been used in the past to understand the underlying processes in the Krafla region. The Mogi model, a spherical pressure point source was used in most of the cases in the past work to understand the reason behind inflation/deflation in the region. The regional deformation (like plate spreading) was modelled by back slip plate spreading model (closing Okada dislocation model) or by a buried dislocation model (opening Okada dislocation model) [Drouin et al., 2017]. In this work, the focus is only on the uplift event that happened in 2018. Therefore, only the Mogi (Spherical source) model is considered to keep it simple. Geodetic Bayesian Inversion Software (GBIS) software is used to perform this modelling. InSAR and GPS data are the inputs given to this software.

6.2. Theory behind Modelling technique

GBIS software uses the Bayesian inversion method to find the source parameters of the best fit model. This section explains the Bayesian inversion and its usage in estimating the source parameters, as shown in figure 6.1. The data vector d is considered along with the variance and covariance matrix Σ_d (from InSAR, GPS or both). On the other hand, the initial set of model parameters m_i is used in the non-linear model G to generate the simulated data d_i. These both are used to calculate the Likelihood function $p(d|m_i)$ (using the equation 6.1) of m_i based on the residuals between the observed data and the simulated observations.

$$p(d \mid m) = (2\pi)^{-N/2} |\Sigma_d|^{-\frac{1}{2}} \times \exp\left[-\frac{1}{2}(d-Gm)^\top \Sigma_d^{-1}(d-Gm)\right] \tag{6.1}$$

where N is the number of observations and Σ_d^{-1} represents the inverse of variance-covariance matrix of the data. A new set of model parameters is created by taking a random step in $p(m)$, where $p(m)$ represents prior information on the model parameters. The non-linear model is used to calculate the simulated observations for the new set of model parameters. The likelihood is again calculated for the new set of model parameters $p(d|m_{i+1})$. The values of the new model parameters are retained if the $p(d|m_{i+1}) > p(d|m_i)$, else the ratio of the new likelihood to the previous is calculated (termed as b). The value of b lies within the range of [0,1]. Additionally in this case, the previous model parameters are retained by changing m_{i+1} to m_i. This chain process is repeated until a representation of posterior PDF ($p(m \mid d)$) is achieved (with $10^5 - 10^7$ iterations). The equation 6.2 is the formula to calculate the posterior PDF. The iterative step in this inversion is the Markov chain Monte Carlo (MCMC) method that includes the Metropolis-Hastings algorithm, with automatic step size selection. More detailed information on the algorithm, automatic step size selection is given in [Bagnardi and Hooper, 2018].

$$p(\mathrm{m} \mid \mathrm{d}) = \frac{p(\mathrm{d} \mid \mathrm{m})\, p(\mathrm{m})}{p(\mathrm{d})} \tag{6.2}$$

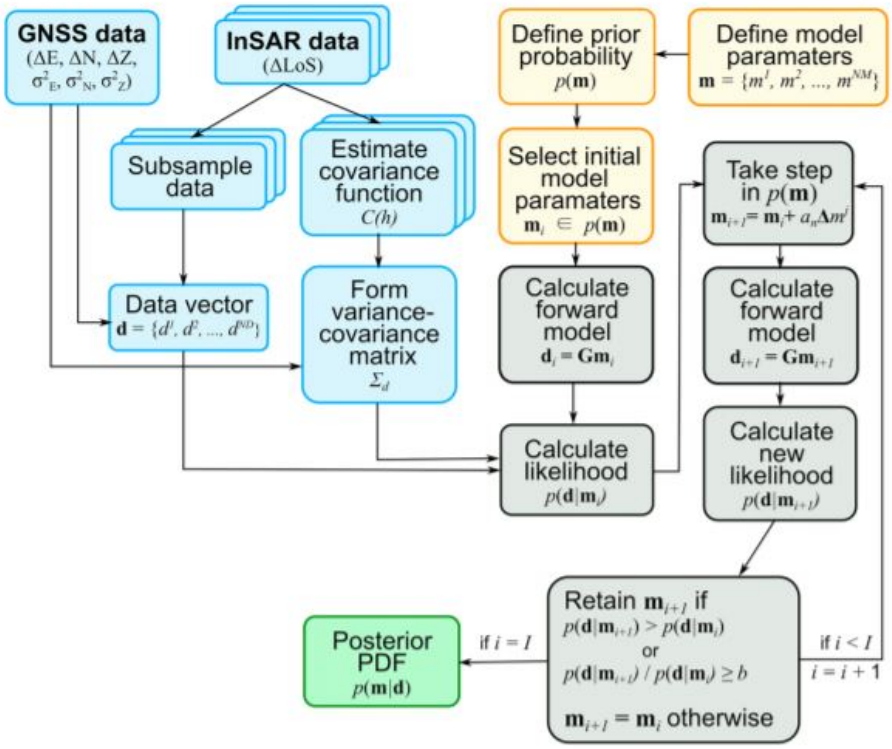

Figure 6.1: Schematic Representation of GBIS method taken from Bagnardi and Hooper [2018.

6.3. Preparing data for GBIS Modelling

In this work, modelling uses both the InSAR and GPS data as input. The region of interest is the Krafla region. Therefore, the data ingested into the software is reduced to the area of interest. The GPS benchmarks within the Krafla region are used with a total of 12 stations. The location of the selected benchmarks can be seen in the figure 6.2. The Mean subtracted horizontal velocities of these GPS benchmarks are considered by fitting a linear trend to the time series of horizontal and vertical displacements of these benchmarks. It is ingested into the algorithm using the input file in the required format as specified in the manual[Bagnardi and Hooper, 2018]. The algorithm assumes no spatial correlation between the benchmarks. It considers only the variance of the velocity components for the benchmark.

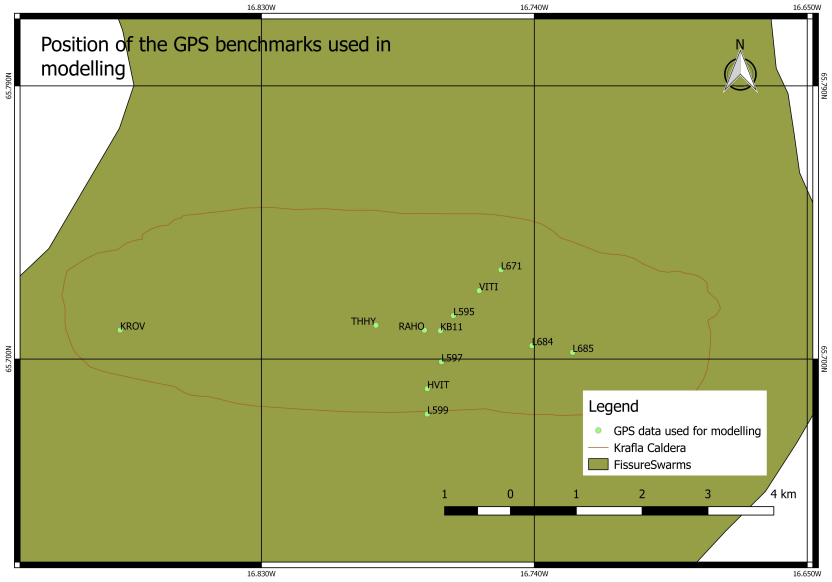

Figure 6.2: Represents the position of the GPS benchmarks in the Krafla region used for modelling.

The InSAR data during summer 2018 is considered to witness the change. The unwrapped phase corrected for various errors (DEM error, orbital error and Atmosphere and orbital error of master) captured on 30-05-2018 and 05-06-2018 with respect to 24-05-2018 is given as input. InSAR data is reduced to the Krafla region ((65.8°N,16.6°E) - (65.6°N, 17°E)) (the region as shown in figure 5.3 and figure 5.8). Approximately 40000 data points from InSAR are used for modelling. The region of the ingested data consists of both the uplift in the north and subsidence in the south. The interferograms of June 2018 are not used for modelling because of the atmospheric noise present in the data (figure 5.3). The variance-covariance matrix is formed assuming that errors in the data can be simulated using an exponential function with nugget, fitted to the isotropic experimental semi-variogram [Bagnardi and Hooper, 2018; Webster and Oliver, 2007]. The semi-variogram is calculated for the entire image by masking out the regions of surface deformation. Then, the Sill, Range and Nugget value of the calculated semi-variogram is given as input for the variance-covariance matrix of the InSAR data in modelling. The reason for choosing this GPS and InSAR data is discussed in the conclusion section. Furthermore, the reference point, wavelength of the sensor, initial model parameters of the Mogi model and its intervals are given as input to the algorithm for further inversion.

Table 6.1: Inputs given for the modelling

Geographical Reference point	16.7666° E	65.7143° N		
Wavelength (m)	0.056			
Model parameters	X-coordinate of point source (m)	Y-coordinate of point source (m)	Depth (m)	Volume change (m^3)
Upper Interval	-5000	-6000	1000	-1.00E+09
Lower Interval	5000	5000	10000	1.00E+02
Start (Initial model parameters)	0	0	1000	-1.00E+06
Step	100	100	100	1.00E+04

Diagrammatic representation of the input data given to the model for inversion is in appendix-D. The input data consists of GPS data, wrapped and unwrapped InSAR data and the sub-sampled interferograms (sub-sampled by Quadtree subsampling [Bagnardi and Hooper, 2018])

6.4. Results and Analysis

The number of iterations was given as $5 \cdot 10^5$ to perform the inversion. Initially, the burn-in period (number of initial iterations to be removed from the computation of the posterior density functions and other statistics) was set to 1 to get the convergence plots. From these plots, the number of iterations required to reach the convergence is obtained. This value is then assigned as the new burn-in period to get the following results as shown in the table 6.3 and in the figures 6.4, 6.5 and 6.6.

Parameters	Optimal	Mean	Median
Mogi X (m)	625.99	630.29	625.56
Mogi Y (m)	-641.03	-643.69	-642.73
Mogi Depth (m)	9314.45	8893.12	9105.13
Mogi DV (m^3)	-4085196.93	-3691520.25	-3795495.50

Figure 6.3: Represents the optimal, mean, median values of the model parameters obtained from modelling using the GBIS software.

In table 6.3, the optimal values for the source parameters of the considered Mogi model are presented. The optimal values are calculated using both the GPS and InSAR data. The optimal value for the X and Y coordinates of the Mogi model is near (600 m) the considered reference point. The position of the Krafla power plant is the reference point. Therefore, the optimal position of the Mogi source is near the power plant. The optimal value of depth is 9314.45 m. The optimal value of volume change is $-4.08 * 10^6 m^3$. The negative sign represents deflation in the region with the value representing the volume change. The magnitude of the depth of the Mogi source and the volume change cannot be compared to the values obtained from previous literature, because different modelling techniques were used in the past work. But, this work can use the concepts from previous modelling results. The main idea that the depth and the volume are related can be seen in this work and in the previous work as well [Drouin et al., 2017; Sturkell et al., 2008 ,etc.]. The depth of the source and the volume change is directly proportional. Therefore, with an increase in depth, higher value in volume change can be noted. Besides the optimal value of the model parameters, GPS and InSAR results are also obtained from the model. The combination of the input GPS data and the GPS results obtained from the model is in figure 6.4. The horizontal vectors point towards the centre (both in the case of data and the model) which represents subsidence. This subsidence seen in the results can be due to the complete GPS data considered along the years. But, the length of the vectors is not similar for the data and the model. The length of the model vectors is smaller than the data vectors. This result represents the fact that the model is trying to fit the data but the fit is not complete. The angle between the vectors of the data and model is less when the benchmarks are present near the source and the opposite is visible in the figure 6.4.

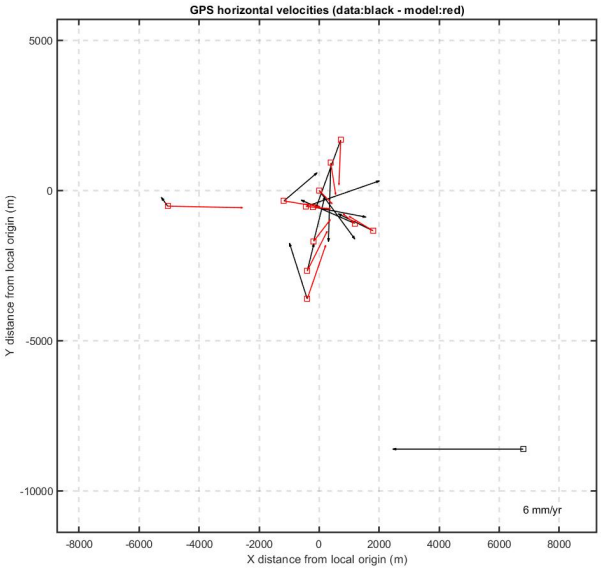

Figure 6.4: Represents the GPS data and the results obtained from the model. Black arrows represent the data and the red arrows represents the best-fit model.

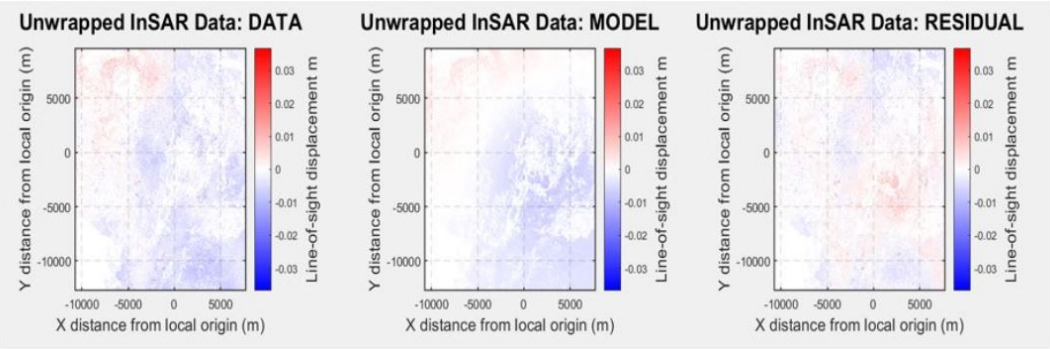

Figure 6.5: Represents unwrapped interferogram of 30-05-2018 (left), the best -fit model (middle) and the residual between data and model (right). The positive line of sight displacement represents uplift or movement towards the satellite.

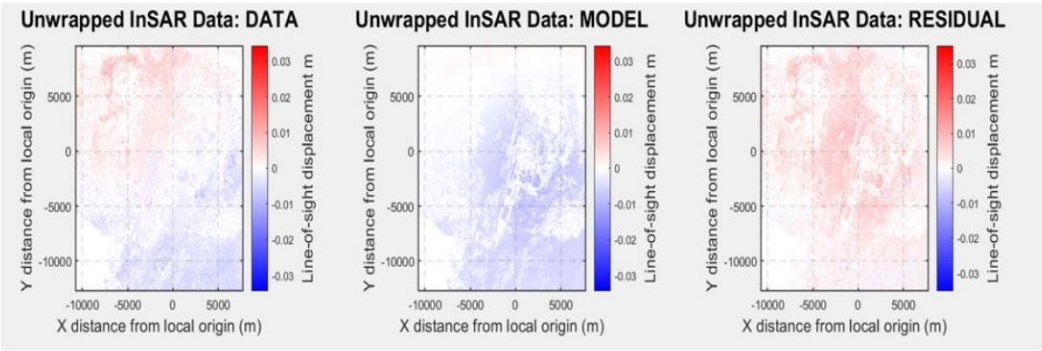

Figure 6.6: Represents unwrapped interferogram of 05-06-2018 (left), the best -fit model (middle) and the residual between data and model (right). The positive line of sight displacement represents Uplift or the movement towards the satellite.

For InSAR, unwrapped interferograms from the model and their corresponding residuals are displayed for both the input InSAR data (unwrapped interferogram of 30-05-2018 and 05-06-2018). The figure 6.5 represents the results obtained from modelling for the input (unwrapped Interferogram of 30-05-2018). In this case, the unwrapped interferograms from the data and model are quite similar. Therefore, the residual obtained is less. On the other hand, the figure 6.6 represents the results obtained from modelling for the input (unwrapped interferogram of 05-06-2018). In this case, the positive line of sight displacement is hardly visible in the unwrapped interferogram from the model, as shown in the unwrapped interferogram from the data. The residuals are higher in this case, as the unwrapped interferogram obtained from the model is not well constrained to achieve the required results. Additionally, in both cases, the unwrapped interferograms from the model mainly show subsidence; very slight uplift is seen. Therefore, both the GPS and InSAR results from modelling is trying to mostly model the subsidence in the region.

The following figures (6.7 and 6.8) are also the results obtained from the modelling carried out in this work. Convergence plots indicate the retained values of that particular model parameter. Additionally, the Posterior source density function plot for each of the source parameter is displayed in the following figure 6.8.

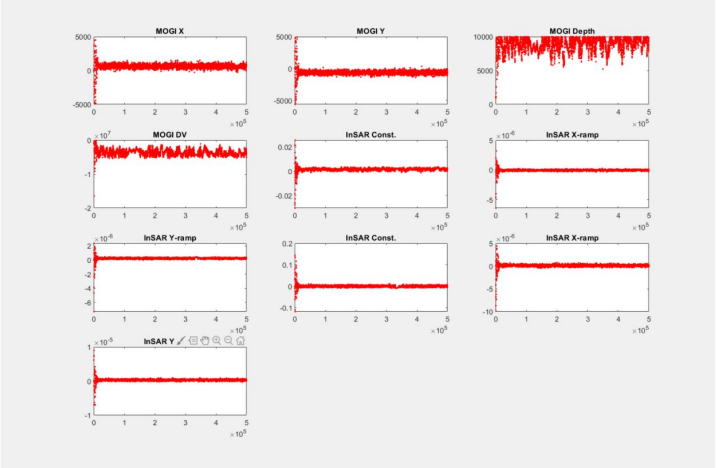

Figure 6.7: Convergence plot for all the source model parameters. The x-axis represents the number of iterations.

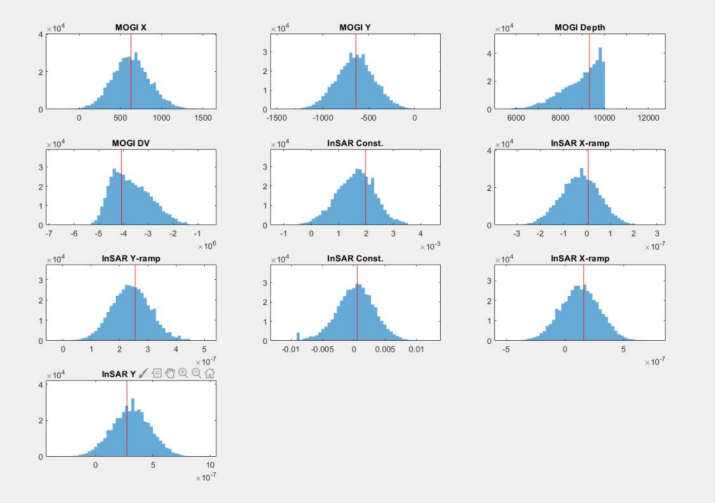

Figure 6.8: Represents histogram of Posterior Density Function (PDF) of the source parameters (blue bars) and the optimal value is shown by red line.

6.5. Discussion and Conclusion

The values of the Unwrapped interferograms ingested into the model are with respect to the 24th May 2018 interferogram. This method is adapted to reduce the noise and to map the uplift signal in the north and subsidence in the south. But, the InSAR results from modelling shows subsidence and very slight uplift. In the figure 6.5 and 6.6, the residuals represent the atmospheric noise and the unmodelled uplift signal(signal that is unaccounted in modelling). GPS velocities are used instead of GPS displacements. The horizontal vectors from the modelling results of GPS represent subsidence in the region. The main reason behind using this type of InSAR and GPS data for modelling is given as follows: Different combinations of InSAR and GPS data was tried. All these combinations had problems in constraining the source parameters and only subsidence was seen in the modelled results. But the combination of data used in this work models subsidence and slight uplift is seen. Additionally, the model parameters have better convergence than the results from the other combinations tested. The model is trying to model the subsidence in the southern region mostly. Therefore, the optimal value of the model parameters mainly represents the source for subsidence in the region. The subsidence seen in the south could be due to the drainage of magma or the solidification of magma seen across the fissure swarms. Of all the model parameters from the results, the depth of the source is not well constrained. This is clear because there is little convergence (figure 6.7) and the PDF is not complete (figure 6.8) in the case of depth. This might be due to the fact that the model is trying to fit a deep-seated source to the data which is deeper than the preset depth interval used in this work. As mentioned before, there is a

relation between the depth and the volume change. The value of the volume change is high as the depth of the source is large. From the results, it is clear that a deep-seated source could be the cause for this subsidence. The actual value of the depth and volume change is not found, but few insights on the observed deformation as mentioned before is obtained. The main reason behind this drawback is the use of data with noise and lack of additional sources to constrain the deformation. Summing up, more work has to be done on the data ingested into modelling. Besides, multiple deformation sources can capture the actual deformation (both the uplift and subsidence) and would help in understanding the actual process behind the deformation.

7

Conclusion

The Krafla volcanic system has a history of volcanic activity. One of the main events from its recent history is the Krafla fires. This eruption has already been discussed in detail in the previous chapters. Following the Krafla rifting event, there was subsidence noted from 1989 in the Krafla region [Tryggvason, 1994]. The centre of subsidence shifted from the Leirhnjukur magma chambers to the Krafla power plant. This subsidence was seen to decrease exponentially and it was not affected much by the increase in extraction of water by the power plant [de Zeeuw-van Dalfsen et al., 2006]. Additionally, there was uplift noted to the north of the Krafla power plant due to a deep-seated magma source [Dalfsen et al., 2004]. Subsidence was observed in the Krafla region until 2017 as seen from previous literature (Drouin and Sigmundsson, 2019; Drouin et al., 2017) and the data used in this work. Suddenly, there was a change in the deformation pattern noted in the region in summer 2018 (obtained from personal communication with the University of Iceland). Therefore, to substantiate the change noted in the region, several geodetic techniques are used in this work. Both the ground and space geodetic techniques are used to verify and understand the change in the region. The main reason for this work is to find the implications associated with this change in deformation and to find if any hazardous event is imminent.

The four geodetic techniques used in this work are Levelling, Global Positioning System (GPS), Gravimetry and InSAR. Data considered for each method varies depending on its availability. But in common, data from 2016 to 2019 is considered to capture the change in deformation over the years. In levelling, three important benchmark pairs are selected based on the availability of the data. The relative heights of the benchmark pair (LV956103-KB8A - East of the power plant) is increasing in the opposite direction to the benchmark pairs (LV056104-KMDC and KMDC-L595 - North of the power plant) (figure 7.2). Therefore, a subsidence bowl is noted near the Krafla power plant. In 2018, a change is observed and there is subsidence noted in the benchmark pairs (LV056104-KMDC and KMDC-L595) present to the north of the power plant. This subsidence can be explained by uplift caused in the centre of the caldera region. Diagrammatic representation and explanation of these observations are given in the following figure 7.1.

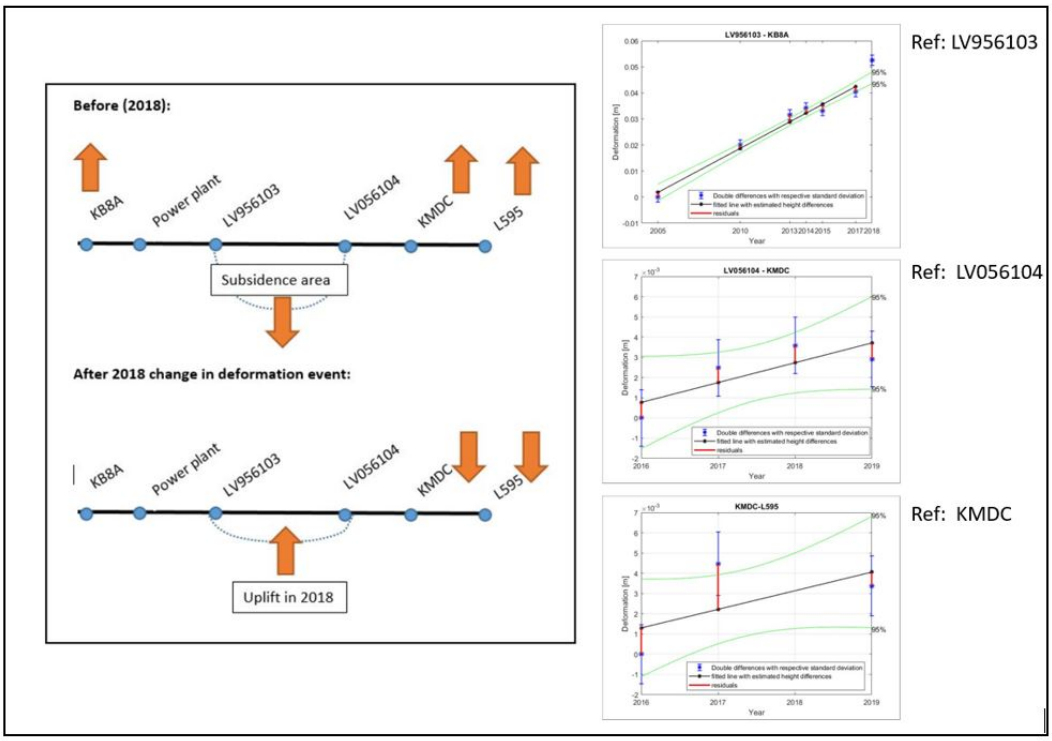

Figure 7.1: Cross section of the change in deformation pattern is displayed on the left side of the figure. On the right side, time series of benchmark pairs shown in the left is displayed and their reference benchmark is also mentioned in the figure.

Alternatively, other geodetic methods were used to monitor the deformation. The local coordinates/ local displacements obtained from the GPS technique along the years (2010-2019) are used to obtain the horizontal and vertical velocities for each of the benchmarks. The horizontal velocities (North and East velocities) obtained from the time series contain both the regional and the local deformation. To focus on local deformation, regional deformation is removed by subtracting the regional mean velocity calculated from the benchmarks. The local deformation shows subsidence in the Krafla region near the power plant (figure 3.9 from chapter-4). Consideration of the complete data (2010-2019) has resulted in this subsidence. Water extraction and the slow drainage of magma could be the possible reasons for the subsidence seen near the power plant [Drouin et al., 2017]. To focus on the uplift, vertical displacement along the years is considered. In particular, the height difference between the years 2017-2018 and 2018-2019 is taken under consideration and the change in deformation pattern is noted. The change in deformation is clearly visible in the figure 3.12 from chapter-4. The inflation is visible near the North, West and East of the power plant. The values are less reliable due to the uncertainty in vertical displacement but the change in deformation can be clearly noted. The extent and the location of the deformation pattern from GPS clearly coincides with the location obtained from the existing levelling data. This uplift, mostly situated to the north of the power plant is clearly seen in the figure 7.2. This uplift is also visible in the vertical displacement time series for the individual benchmarks present in the Krafla region (figure:3.20).

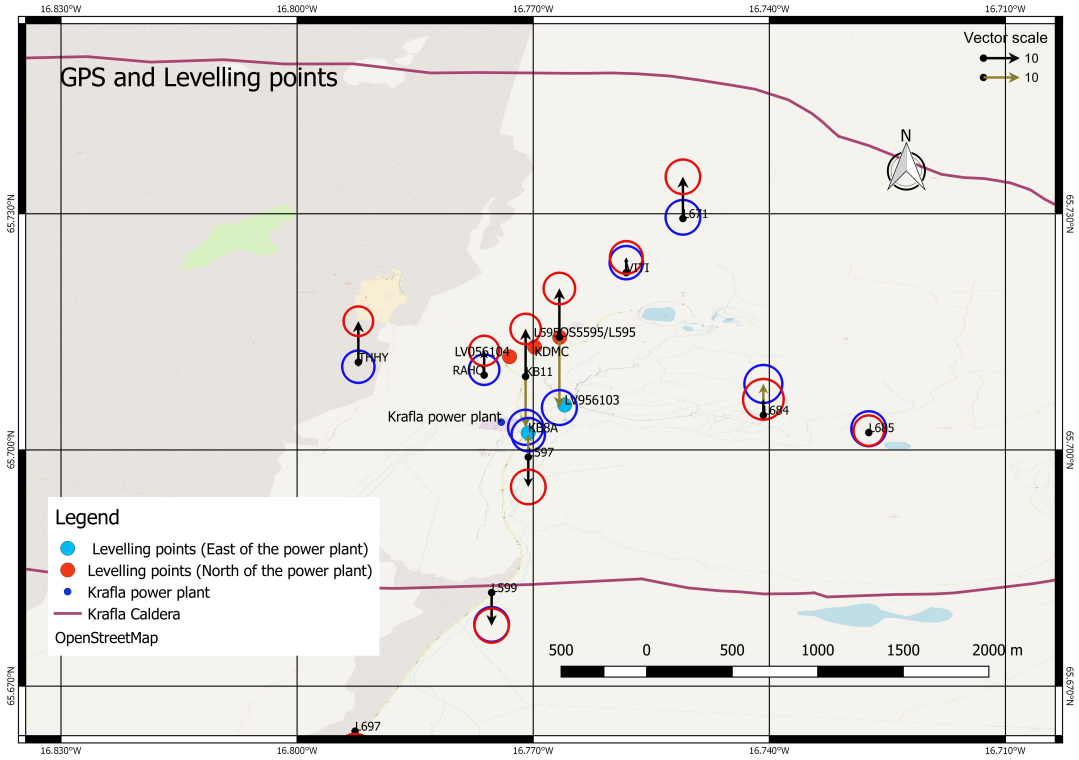

Figure 7.2: Represents the change in deformation from 2017-18 (brown colored vector lines and blue circles) to 2018-19 (black colored vector lines and red circles) in GPS data in the form of vector data. The error ellipse is circle in this case for each benchmark. It represents the one sigma uncertainty for benchmark considered. The benchmarks considered for levelling is also displayed. Different colors are given to the benchmarks based on the similar pattern of deformation (from relative heights) seen among the benchmark pairs. Finally, the street map is displayed in the background.

The other geodetic method used in this work is InSAR. The Unwrapped interferograms obtained from PSI Analysis are used for further analysis. The results used in this work still contain atmospheric noise. To understand the change in deformation pattern, a closer look at the results is taken by considering the unwrapped interferograms (corrected for errors: DEM error, Orbital Error, Atmosphere and orbital error of the master image) with respect to the result obtained on 24th May 2018. There is uplift seen in the Krafla region (figure 5.3 near the power plant. To reduce the noise and to understand the change in deformation, line of sight velocity before and after the event is calculated (figure 7.3 and figure 7.4). Positive line of sight velocity (uplift) is seen to north of the power plant. This is clearly seen in the figure 7.5. Additionally, the extent of uplift seen from the GNSS data coincides approximately with the areal extent from the InSAR data. To substantiate the findings, the results obtained from this InSAR work is compared to the results obtained on personal communication with the University of Iceland (figure 5.9) [Drouin and Sigmundsson, October, 2019]. The near-East and up velocities before and after the event is shown. These are constructed using the InSAR data from an ascending and descending track. While in this InSAR work, only the descending track sentinel data is used. Therefore, the results are in line of sight velocity and the magnitude of the change in deformation cannot be compared.

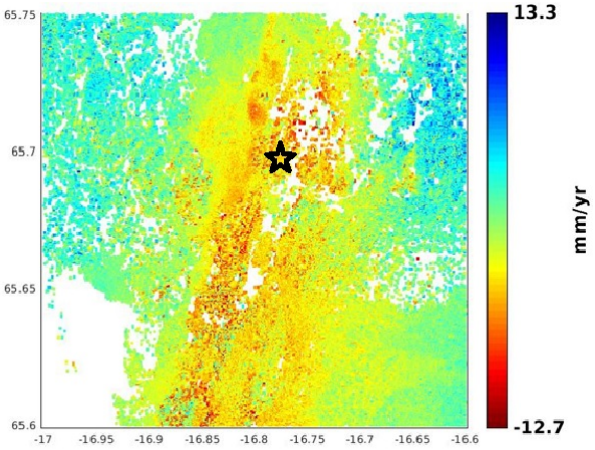

Figure 7.3: Line of sight velocity corrected for DEM and orbital error before the event (April 2016 - May 2018) for the complete region. The black star represents the location of the Krafla power plant.

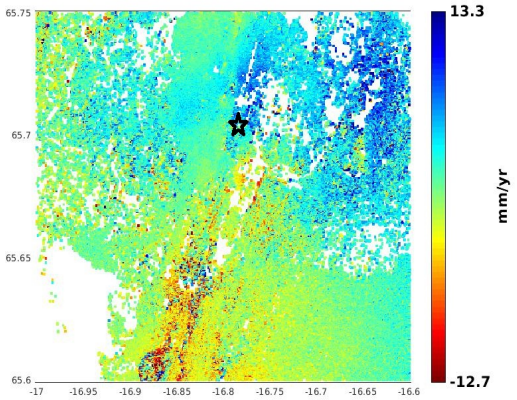

Figure 7.4: Line of sight velocity corrected for DEM and orbital error after the event (June 2018 - September 2019) for the required region. The black star represents the location of the Krafla power plant.

The geodetic techniques discussed above helps in finding the location, extent and the magnitude of the deformation. But the reason behind the deformation is not identified from these methods. Therefore, gravimetry is used to determine the sub-surface mass/density changes. The net gravity change in the year 2017-2018 is shown in figure 7.6. From the available data, there is an increase in gravity seen in the benchmarks L595 and L684. On the other hand, there is a decrease in net gravity in the benchmark L597. The water extraction from the power plant could influence the net gravity change in this benchmark. The increase in net gravity seen mostly in the north and east of the Krafla power plant. It is in line with the uplift seen in the Krafla region from the other geodetic methods (figure 7.6). The increase in gravity seen among the benchmarks in the north of the power plant could be due to the migration of magma from the deep-seated sources to shallow magma Chambers. The deep-seated sources can be either from the deep source present in the north of the Krafla caldera [Dalfsen et al., 2004] or the deep source present under the Krafla caldera which was active during the Krafla rifting episode [Sturkell et al., 2008]. Therefore, by combining different geodetic techniques, the position and the extent of the change in deformation has been found. More data and further processing is required to see the actual change in the magnitude of the deformation. To address the reasoning behind this uplift, more spatially distributed net gravity values during the event would be required.

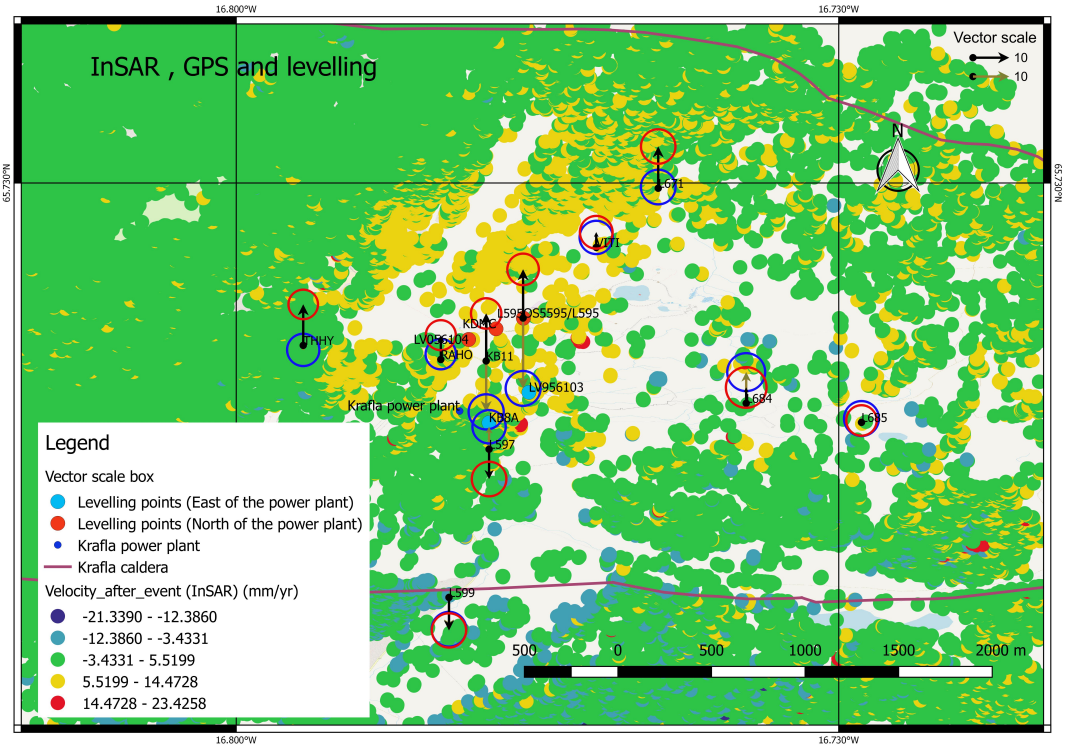

Figure 7.5: Represents Line of sight velocity (after the event) from InSAR in mm/yr. The change in deformation from 2017-18 (brown colored vector lines and blue circles) to 2018-19 (black colored vector lines and red circles) in GPS data is shown in the form of vector data. The error ellipse is represented by a circle for each benchmark. It represents the one sigma uncertainty for the height difference. The benchmarks considered for levelling are also displayed. Different colors are given to the benchmarks based on the similar pattern of deformation (from relative heights) seen among the benchmark pairs. Finally, the street map is displayed in the background.

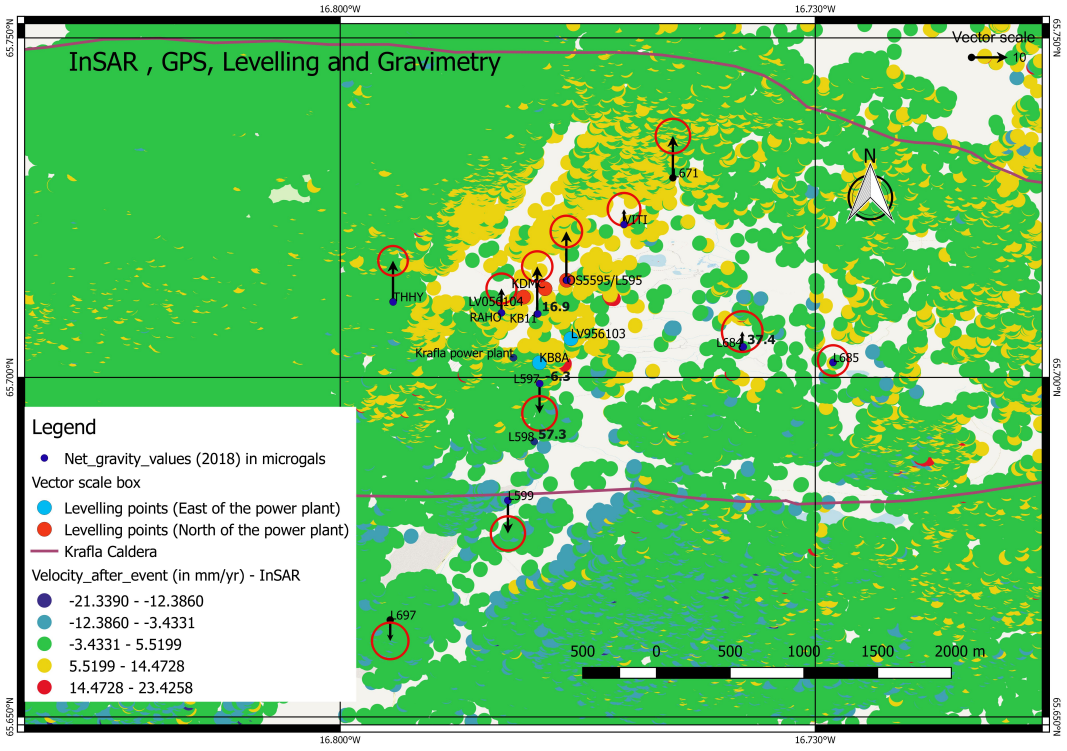

Figure 7.6: Represents Line of sight velocity (after the event) from InSAR in mm/yr. Height changes (2018-2019) from GPS are also shown in the form of black colored vector lines and red circles. The error ellipse is represented by a circle for each benchmark. It represents the one sigma uncertainty for the height difference. The benchmarks considered for levelling are also displayed. Different colors are given to the benchmarks based on the similar pattern of deformation (from relative heights) seen among the benchmark pairs. Additionally, the net gravity value differences (2017-2018) are also displayed. Finally, the street map is shown in the background.

The source parameters which could explain the observed deformation are identified using modelling. A single Mogi source is used to model the change in deformation in 2018. The model mainly captures the subsidence from the input data (GPS velocities and InSAR data) and in accordance finds the best-fit source parameters. The main findings of the modelling are: the model is trying to find a deeper depth to explain the change in deformation. Accordingly, there is a larger volume change needed to explain the observed deformation. The actual values of the depth and volume change are not found but insight in the possible cause of deformation is obtained. On the other hand, the optimal values of the model source parameters are not very reliable due to the drawbacks presented in the modelling chapter in this work. These drawbacks have to be addressed using better input data and improved model complexity (with multiple sources).

The following paragraph explicitly answers the main research question and the objectives formulated to support it. Following is the main research question:
What is the insight that could be gained from the available geodetic data regarding the location, extent (vertical and horizontal) and the gravity change of the recently observed change in the deformation pattern noted in the Krafla region, Iceland ?

The recent change in the deformation pattern in the Krafla region (in 2018) is seen in the geodetic data (InSAR, GPS and Levelling). There is an uplift seen in the area. This change in pattern is mainly situated to the North of the Krafla power plant. There is still subsidence seen to the south of the power plant along the fissure swarm. Therefore, this event is localized to the North of the power plant. The approximate extent of uplift seen from the geodetic data is (65.75°N,16.6°E) - (65.7°N, 16.9°E). Additionally, there is an increase in net gravity seen in the same region of uplift, which supports the other geodetic data. This could be because there is an increase in sub-surface mass/density, possibly due to the migration of magma from deep to the shallow magma chambers. The results from modelling try to constrain the source parameters to explain the subsidence seen in the south of the power plant.

To support the answer to the research question, the more detailed research objectives are also answered

in the following section:

Can the change in the deformation pattern be located in the InSAR data analysis? If yes, what is the location and the extent (vertical and horizontal) of deformation happening in the region?

The change in the deformation pattern is clearly seen in the line of sight velocity before and after the event. The positive line of sight velocity seen in the region is 13 - 14 mm/yr. This uplift is mainly situated to the North of the power plant. Additionally, uplift is also seen to the East and West of the power plant. There is still subsidence seen along the fissure swarm (South of the power plant).

Does the levelling data show similar vertical deformation as seen in InSAR ?

The subsidence noted in 2018 in the benchmark pairs (LV056104-KMDC and KMDC-L595) present to the north of the power plant corresponds with the uplift caused in the centre of the caldera region (North of the power plant). The uplift is identified indirectly from the available levelling data; therefore, a similar deformation pattern is observed as seen in InSAR. The magnitude of change in vertical deformation is not significant in levelling data but the information obtained from this data supports the InSAR information. In the future, InSAR data could be converted into near-East and Up displacements to be compared in terms of magnitude with the levelling data.

Similarly, does the GPS data show similar location, timing and the extent of deformation as seen in InSAR and Levelling ?

Considering the vertical displacement (from the considered GNSS data) along the years, the height difference between 2017-2018 and 2018-2019 represents the change in the deformation pattern. The uplift is visible to the North, East and West of the power plant. The values are less reliable due to the uncertainty in vertical displacement but the change in deformation can be clearly noted. The region of uplift is similar as seen in the levelling and InSAR data (figure 7.5 and figure 7.6).

Does the change in gravity data help in understanding the underlying process in 2018?

The increase in net gravity change is in the similar region of uplift as seen in the other geodetic techniques. The change in gravity has substantiated the fact that there is an uplift caused due to an increase in sub-surface mass/density (movement of magma from deep to shallow chamber). But, the reason of this activity is not known.

Is the deformation seen in the above observation techniques significant enough to draw a conclusion from it?

With respect to levelling, the subsidence seen in 2018 in the benchmarks pairs (LV056104-KMDC and KMDC-L595) present to the north of the power plant explains the uplift caused in the centre of the caldera region (North of the power plant). The value of subsidence in 2018 in these benchmarks pairs is almost equal to the 2σ value. Therefore, the deformation seen in levelling (from the available data) is not significant but the information supports the other methods.

In the time series of the local up coordinates (from PPP data), uplift in 2018 is seen in the benchmarks near the North of the Krafla power plant. The positive height differences in most of the benchmarks (in the Krafla region) calculated during 2018-19 are significant as the value is greater than the uncertainty value of the measurement (4-5 mm).

In gravimetry, the increase in net gravity in 2018 is significantly seen in very few benchmarks (L684, L595, L598). There is an increase in net gravity seen in other benchmarks but they are within the 95% confidence interval due to measurement and estimation uncertainty. In InSAR, statistical testing was not done to check if the results are significant.

An important conclusion is that none of the individual techniques is suitable to detect and evaluate the deformation pattern, but the combination of these techniques can provide clear insights on the deformation pattern due to the consistency observed.

Can the Model estimate the location, depth and the volume of the possible sources responsible for the deformation based on the InSAR and GPS data?

The model mostly captures the subsidence seen to the south of the power plant. The model source parameters obtained from modelling are associated with this subsidence. The approximate location of the source was estimated using a simple Mogi Model. The actual value of the depth and volume change is not found but an insight in the possible cause of deformation is obtained. The model is trying to find a deeper depth to explain the deformation observed in the data. This supports the fact that deeper sources present near the power plant could be the possible reason for the change in deformation.

7.1. Recommendations

This work mainly concentrated on substantiating the uplift seen in the region using different data sets. This work is a start as it considers only the data until 2019. Continuing this deformation analysis into the future will help in understanding the reason and the possible implications associated with this change in deformation event. This is especially important as this event could be the first indication of a future rifting event; therefore, it is essential to keep monitoring the region to ensure timely warning can be given to the local governments in case activity accelerates. Regarding this work, there is room for further improvements in each of the techniques for better results in the future.

With respect to levelling, the following are the most important improvements: the number of levelling benchmarks measured near the deformation region can be increased and the continuity in the data must be maintained to get a proper time series. This would help in understanding the deformation pattern across the region and along the years.

Primary improvements in GPS are listed as following: A certain number of benchmarks has to be considered and measured every year during the GNSS campaign. The benchmarks considered should be scattered all over the region. Therefore, a continuous time series from these benchmarks can help in explaining the deformation pattern in the region. The Continuous GPS data is already available (from KRAC, a CGPS benchmark near the Krafla power plant and BJAC, a CGPS benchmark in the Bjarnarflag region and a CGPS station in Theistareykir (North of the Krafla region)) but additional CGPS station near the benchmark VITI would help in better monitoring of the crustal deformation in the region. Secondary improvements can be done by increasing the number of benchmarks. These additional benchmarks can be measured alternate years apart from the required ones.

For InSAR, the input (satellite) data must be checked for certain disturbances like snow cover, vegetation and atmospheric disturbances in the region. Both the ascending and descending track data must be taken for the same area. This would help in converting the line of sight measurements into real time deformation measurements. The atmospheric noise in the data has a huge influence and therefore removal of this noise is very important. The other secondary improvements that can be done are listed as following: Depending on the availability of time and cost, data from other satellites can be used to substantiate the results. InSAR and GPS data go hand-in-hand. Therefore combining this would help in understanding the deformation better.

Last but not the least, gravimetry helps in understanding the subsurface changes. The essential things to be followed for better results in gravity is given as following: Inconsistency in data, use of different base station along the years and use of different gravimeters along the years must be addressed. The net gravity data can also be used to identify the subsurface mass and volume change for better understanding. Besides, following secondary improvements can be done to improve the accuracy and the precision of the results: Double loop measurements can be done instead of single loop and the length of the measurements can be increased. The measurements from Absolute gravimeter can be used to support the results from the relative gravimeter.

Better results for the optimal value of the model parameters can be obtained from well processed input data and multiple source modelling. On improving the results obtained from all the above mentioned geodetic techniques, better correlation in spatial and temporal distribution of data can be performed to understand the deformation. Additionally, this data can be used in modelling to understand the process and find the source, extent and the changes caused by deformation.

Bibliography

[1] Abou-Galala, M., Rabah, M., Kaloop, M., and Zidan, Z. M. Assessment of the accuracy and convergence period of precise point positioning. *Alexandria engineering journal*, 57(3):1721–1726, 2018.

[2] Algarni, D. A. and Ali, A. E. Heighting and distance accuracy with electronic digital levels. *Journal of King Saud University-Engineering Sciences*, 10(2):229–239, 1998.

[3] Árnadóttir, T., Lund, B., Jiang, W., Geirsson, H., Björnsson, H., Einarsson, P., and Sigurdsson, T. Glacial rebound and plate spreading: results from the first countrywide gps observations in iceland. *Geophysical Journal International*, 177(2):691–716, 2009.

[4] Árnason, K. New conceptual model for the magma-hydrothermal-tectonic system of krafla, ne iceland. *Geosciences*, 10(1):34, 2020.

[5] Auriac, A., Spaans, K., Sigmundsson, F., Hooper, A., Schmidt, P., and Lund, B. Iceland rising: Solid earth response to ice retreat inferred from satellite radar interferometry and visocelastic modeling. *Journal of Geophysical Research: Solid Earth*, 118(4):1331–1344, 2013.

[6] Bagnardi, M. and Hooper, A. Inversion of surface deformation data for rapid estimates of source parameters and uncertainties: A bayesian approach. *Geochemistry, Geophysics, Geosystems*, 19(7):2194–2211, 2018.

[7] Battaglia, M., Cervelli, P. F., and Murray, J. R. dmodels: A matlab software package for modeling crustal deformation near active faults and volcanic centers. *Journal of Volcanology and Geothermal Research*, 254:1–4, 2013.

[8] Björnsson, A. Dynamics of crustal rifting in ne iceland. *Journal of Geophysical Research: Solid Earth*, 90 (B12):10151–10162, 1985.

[9] Björnsson, A., Saemundsson, K., Einarsson, P., Tryggvason, E., and Grönvold, K. Current rifting episode in north iceland. *Nature*, 266(5600):318–323, 1977.

[10] Crosetto, M., Monserrat, O., Cuevas-González, M., Devanthéry, N., and Crippa, B. Persistent scatterer interferometry: A review. *ISPRS Journal of Photogrammetry and Remote Sensing*, 115:78–89, 2016.

[11] Dalfsen, E. D. Z.-V., Pedersen, R., Sigmundsson, F., and Pagli, C. Satellite radar interferometry 1993-1999 suggests deep accumulation of magma near the crust-mantle boundary at the krafla volcanic system, iceland. *Geophysical Research Letters*, 31(13), 2004.

[12] de Zeeuw-van Dalfsen, E., Rymer, H., Williams-Jones, G., Sturkell, E., and Sigmundsson, F. Integration of micro-gravity and geodetic data to constrain shallow system mass changes at krafla volcano, n iceland. *Bulletin of volcanology*, 68(5):420–431, 2006.

[13] Drouin, V. Gps time-series. URL `http://icelandsupersite.hi.is/gps/ts/NVZ.html`.

[14] Drouin, V. and Sigmundsson, F. Countrywide observations of plate spreading and glacial isostatic adjustment in iceland inferred by sentinel-1 radar interferometry, 2015–2018. *Geophysical Research Letters*, 46(14):8046–8055, 2019.

[15] Drouin, V. and Sigmundsson, F. Slow inflation within the krafla caldera 2018-2019 (intenal communication isor and university of iceland). October, 2019.

[16] Drouin, V., Sigmundsson, F., Ófeigsson, B. G., Hreinsdóttir, S., Sturkell, E., and Einarsson, P. Deformation in the northern volcanic zone of iceland 2008–2014: An interplay of tectonic, magmatic, and glacial isostatic deformation. *Journal of Geophysical Research: Solid Earth*, 122(4):3158–3178, 2017.

[17] Drouin, V., Sigmundsson, F., Verhagen, S., Ófeigsson, B. G., Spaans, K., and Hreinsdóttir, S. Deformation at krafla and bjarnarflag geothermal areas, northern volcanic zone of iceland, 1993–2015. *Journal of Volcanology and Geothermal Research*, 344:92–105, 2017.

[18] Einarsson, P. S-wave shadows in the krafla caldera in ne-iceland, evidence for a magma chamber in the crust. *Bulletin Volcanologique*, 41(3):187–195, 1978.

[19] Einarsson, P. Plate boundaries, rifts and transforms in iceland. *Jökull*, 58(12):35–58, 2008.

[20] Fattahi, H. and Amelung, F. Insar uncertainty due to orbital errors. *Geophysical Journal International*, 199(1):549–560, 2014.

[21] Foulger, G., Jahn, C.-H., Seeber, G., Einarsson, P., Julian, B., and Heki, K. Post-rifting stress relaxation at the divergent plate boundary in northeast iceland. *Nature*, 358(6386):488–490, 1992.

[22] Gudmundsson, A. Dynamics of volcanic systems in iceland: example of tectonism and volcanism at juxtaposed hot spot and mid-ocean ridge systems. *Annual Review of Earth and Planetary Sciences*, 28 (1):107–140, 2000.

[23] Hanssen, R. F. *Radar interferometry: data interpretation and error analysis*, volume 2. Springer Science & Business Media, 2001.

[24] Hauksson, E. Episodic rifting and volcanism at krafla in north iceland: Growth of large ground fissures along the plate boundary. *Journal of Geophysical Research: Solid Earth*, 88(B1):625–636, 1983.

[25] Hofton, M. and Foulger, G. Postrifting anelastic deformation around the spreading plate boundary, north iceland: 1. modeling of the 1987–1992 deformation field using a viscoelastic earth structure. *Journal of Geophysical Research: Solid Earth*, 101(B11):25403–25421, 1996.

[26] Hooper, A., Zebker, H., Segall, P., and Kampes, B. A new method for measuring deformation on volcanoes and other natural terrains using insar persistent scatterers. *Geophysical research letters*, 31(23), 2004.

[27] Hooper, A., Segall, P., and Zebker, H. Persistent scatterer interferometric synthetic aperture radar for crustal deformation analysis, with application to volcán alcedo, galápagos. *Journal of Geophysical Research: Solid Earth*, 112(B7), 2007.

[28] Johnsen, G., Bjornsson, A., Sigurdsson, S., et al. Gravity and elevation changes caused by magma movement beneath the krafla caldera, northeast iceland. *Journal of Geophysics*, 47(1):132–140, 1980.

[29] Landsvirkjun, r. Krafla, mývatn og laxá - fínhæðarmælingar sumarið 2005, 2006.

[30] Landsvirkjun, r. Krafla, mývatn fínhæðarmælingar 2010, 2011.

[31] McCormack, H., Thomas, A., and Solomon, I. The capabilities and limitations of satellite insar and terrestrial radar interferometry, 2011.

[32] Meta, A., Prats, P., Steinbrecher, U., Mittermayer, J., and Scheiber, R. Terrasar-x topsar and scansar comparison. In *7th European Conference on Synthetic Aperture Radar*, pages 1–4. VDE, 2008.

[33] Metzger, S., Jónsson, S., and Geirsson, H. Locking depth and slip-rate of the húsavík flatey fault, north iceland, derived from continuous gps data 2006-2010. *Geophysical Journal International*, 187(2):564–576, 2011.

[34] Muquans. Absolute quantum gravimeters. URL `https://www.muquans.com/product/absolute-quantum-gravimeter`.

[35] NASA. Polarimetry (get to know sar). URL `https://nisar.jpl.nasa.gov/mission/get-to-know-sar/polarimetry/`.

[36] (NRCAN), N. R. C. Precise point positioning. URL `https://webapp.geod.nrcan.gc.ca/geod/tools-outils/ppp.php`.

[37] Online, E. S. Sentinel-1 data products. URL `https://sentinel.esa.int/web/sentinel/missions/sentinel-1/data-products`.

[38] Pedersen, R., Sigmundsson, F., and Masterlark, T. Rheologic controls on inter-rifting deformation of the northern volcanic zone, iceland. *Earth and Planetary Science Letters*, 281(1-2):14–26, 2009.

[39] Pinel, V., Poland, M. P., and Hooper, A. Volcanology: lessons learned from synthetic aperture radar imagery. *Journal of Volcanology and Geothermal Research*, 289:81–113, 2014.

[40] Rotation, I. E. and Services, R. S. International terrestial reference frame. URL `https://www.iers.org/IERS/EN/DataProducts/ITRF/itrf.html`.

[41] Rymer, H., Cassidy, J., Locke, C. A., and Sigmundsson, F. Post-eruptive gravity changes from 1990 to 1996 at krafla volcano, iceland. *Journal of Volcanology and Geothermal Research*, 87(1-4):141–149, 1998.

[42] Scihub, C. Copernicus open access hub. URL `https://scihub.copernicus.eu/dhus/#/home`.

[43] Scrintex. Cg-5 autograv gravity meter. URL `https://scintrexltd.com/wp-content/uploads/2018/11/CG-5-Brochure-R3.pdf`.

[44] Sigmundsson, F. *Iceland geodynamics: crustal deformation and divergent plate tectonics*. Springer Science & Business Media, 2006.

[45] Sigmundsson, F., Vadon, H., and Massonnet, D. Readjustment of the krafla spreading segment to crustal rifting measured by satellite radar interferometry. *Geophysical Research Letters*, 24(15):1843–1846, 1997.

[46] Sturkell, E., Sigmundsson, F., Geirsson, H., Ólafsson, H., and Theodórsson, T. Multiple volcano deformation sources in a post-rifting period: 1989–2005 behaviour of krafla, iceland constrained by levelling, tilt and gps observations. *Journal of Volcanology and Geothermal Research*, 177(2):405–417, 2008.

[47] Teunissen, P. and Montenbruck, O. *Springer handbook of global navigation satellite systems*. Springer, 2017.

[48] Teunissen, P., Simons, D., and Tiberius, C. Probability and observation theory: an introduction. *Delft University of Technology, Faculty of Aerospace Engineering, Delft, the Netherlands*, 2006.

[49] Torge, W. Gravity and height variations connected with the current rifting episode in northern iceland. *Tectonophysics*, 71(1-4):227–240, 1981.

[50] Tryggvason, E. Widening of the krafla fissure swarm during the 1975–1981 volcano-tectonic episode. *Bulletin volcanologique*, 47(1):47–69, 1984.

[51] Tryggvason, E. Multiple magma reservoirs in a rift zone volcano: Ground deformation and magma transport during the september 1984 eruption of krafla, iceland. *Journal of volcanology and geothermal research*, 28(1-2):1–44, 1986.

[52] Tryggvason, E. Ground deformation in askja, iceland: its source and possible relation to flow of the mantle plume. *Journal of volcanology and geothermal research*, 39(1):61–71, 1989.

[53] Tryggvason, E. Surface deformation at the krafla volcano, north iceland, 1982–1992. *Bulletin of Volcanology*, 56(2):98–107, 1994.

[54] van der Marel, H. Reference systems for surveying and mapping lecture notes. URL `https://d1rkab7tlqy5f1.cloudfront.net/CiTG/Over%20faculteit/Afdelingen/Geoscience%20%26%20Remote%20sensing/Study/TRS_3-1.pdf`.

[55] Webster, R. and Oliver, M. A. *Geostatistics for environmental scientists*. John Wiley & Sons, 2007.

A

Levelling data

A.1. Description

The selected benchmark pairs from the year 2013-2019 data is displayed in this section. The data is displayed with the distance, Backsight and foresight measurements. The difference and the mean are calculated whose formulas are given in chapter-2. The Sum of Forwards, Sum of Backwards, Mean height Difference, Difference, closing error and the standard deviation results are displayed for each of the benchmark pairs. Additionally, the forward and the backward is maintained same for all the benchmark pairs to get a proper relative height differences along different years. These are the values which have been used in generating the graphs that are displayed in chapter - 2.

Following are the selected benchmark pairs from each of the year:

- Year (2013) ⟶ LV956103 - KB8A
- Year (2014) ⟶ LV956103 - KB8A
- Year (2015) ⟶ LV956103 - KB8A
- Year (2016) ⟶ KDMC-L595 and KDMC - LV056104
- Year (2017) ⟶ KDMC-L595 , KDMC - LV056104 AND LV956103 - KB8A
- Year (2018) ⟶ KDMC - LV056104 and LV956103 - KB8A
- Year (2019) ⟶ KDMC-L595 and KDMC - LV056104

2013 :

2013 data : (LV956103 – KB8A)

	POINT ID		DISTANCE [m]		Backsight [m]	Foresight [m]	Difference	Error [mm]	Mean
	From	To	Bi	Fi	Bi	Fi	dhi = Bi-Fi	dh2 - dh1	dh = (dh1+dh2)/2
i=1	LV956103				0,79428	1,99912	-1,20484	0,0002	-1,20474
i=2					0,79442	1,99906	-1,20464		
i=1					0,24845	1,60427	-1,35582	-0,00307	-1,357355
i=2					0,24543	1,60432	-1,35889		
i=1					0,39588	1,68422	-1,28834	3E-05	-1,288325
i=2					0,39593	1,68424	-1,28831		
i=1					0,79046	1,51576	-0,7253	-0,00019	-0,725395
i=2					0,79019	1,51568	-0,72549		
i=1					0,78626	2,20792	-1,42166	-5E-05	-1,421685
i=2					0,78614	2,20785	-1,42171		
i=1					0,29632	1,40613	-1,10981	-3E-05	-1,109825
i=2					0,29638	1,40622	-1,10984		
i=1					1,04077	1,26708	-0,22631	-0,00018	-0,2264
i=2					1,04055	1,26704	-0,22649		
i=1					0,30211	2,06572	-1,76361	1E-04	-1,76356
i=2					0,3022	2,06571	-1,76351		
i=1					1,93524	0,55627	1,37897	-1E-04	1,37892
i=2					1,93524	0,55637	1,37887		
i=1					0,27721	0,58298	-0,30577	3E-05	-0,305755
i=2					0,27722	0,58296	-0,30574		
i=1		KB8A			0,33437	1,9569	-1,62253	0,00011	-1,622475
i=2					0,33424	1,95666	-1,62242		
i=1									0
i=2									
i=1	KB8A				1,95711	0,33741	1,6197	-7E-05	1,619665
i=2					1,95703	0,3374	1,61963		
i=1					0,41642	0,10744	0,30898	-5E-05	0,308955
i=2					0,41637	0,10744	0,30893		
i=1					0,48418	1,85626	-1,37208	2E-05	-1,37207
i=2					0,48421	1,85627	-1,37206		
i=1					1,964	0,210777	1,753223	7E-06	1,7532265
i=2					1,96396	0,21073	1,75323		
i=1					1,33585	1,1139	0,22195	0,0002	0,22205
i=2					1,33575	1,1136	0,22215		
i=1					1,36769	0,23957	1,12812	0,0002	1,12822
i=2					1,36787	0,23955	1,12832		
i=1					2,11829	0,70789	1,4104	-0,00019	1,410305
i=2					2,1182	0,70799	1,41021		

i=1					1,35799	0,63153	0,72646	-0,00019	0,726365
i=2					1,35786	0,63159	0,72627		
i=1					1,57864	0,2879	1,29074	-0,00016	1,29066
i=2					1,57856	0,28798	1,29058		
i=1					1,67372	0,32412	1,3496	-4E-05	1,34958
i=2					1,67376	0,3242	1,34956		
i=1		LV956			2,12541	0,91629	1,20912	-7E-05	1,209085
i=2		103			2,12538	0,91633	1,20905		

Sum of Forwards [m]:	-9,646595	LV956103 – KB8A
Sum of Backwards [m]:	9,6460415	KB8A - LV956103
Mean height difference [m]:	-9,64631825	
Difference |Bi + Fi| [mm]:	0,5535	
Closing error [mm/km]:	0,579126341	
Total distance (forward + backward) [km]:	0,95575	
Allowed difference [mm]	0,977624672	
Standard deviation [mm]	0,691285035	

2014 :

2014 data : (LV956103 – KB8A)

	POINT ID		**DISTANCE [m]**		**Backsight [m]**	**Foresight [m]**	**Difference**	**Error [mm]**	**Mean**
	From	**To**	**Bi**	**Fi**	**Bi**	**Fi**	**dhi = Bi-Fi**	**dh2 - dh1**	**dh = (dh1+dh2)/2**
i=1	LV956				1,09507	2,34936	-1,25429	-0,00011	-1,254345
i=2	103				1,09496	2,34936	-1,2544		
i=1					0,47329	1,67814	-1,20485	-5E-05	-1,204875
i=2					0,4733	1,6782	-1,2049		
i=1					0,65381	1,94046	-1,28665	0,00012	-1,28659
i=2					0,65388	1,94041	-1,28653		
i=1					0,95969	1,64678	-0,68709	0,0001	-0,68704
i=2					0,95967	1,64666	-0,68699		
i=1					0,89735	1,82697	-0,92962	0,0001	-0,92957
i=2					0,89741	1,82693	-0,92952		
i=1					0,26982	1,9103	-1,64048	-3E-05	-1,640495
i=2					0,26986	1,91037	-1,64051		
i=1					0,59598	1,8987	-1,30272	0	-1,30272
i=2					0,59596	1,89868	-1,30272		
i=1					1,02933	1,66674	-0,63741	-4E-05	-0,63743
i=2					1,02939	1,66684	-0,63745		
i=1					1,74007	1,50242	0,23765	-0,00017	0,237565
i=2					1,73991	1,50243	0,23748		
i=1		KB8A			1,14083	2,07865	-0,93782	-5E-05	-0,937845

i=2					1,14088	2,07875	-0,93787		
i=1								0	0
i=2									
i=1	KB8A				2,07423	1,10899	0,96524	-9E-05	0,965195
i=2					2,07409	1,10894	0,96515		
i=1					0,97162	1,18965	-0,21803	-2E-05	-0,21804
i=2					0,97163	1,18968	-0,21805		
i=1					1,67614	1,05565	0,62049	0,0002	0,62059
i=2					1,67622	1,05553	0,62069		
i=1					2,29797	1,06016	1,23781	-1E-05	1,237805
i=2					2,29806	1,06026	1,2378		
i=1					1,96088	0,32951	1,63137	0,00013	1,631435
i=2					1,96097	0,32947	1,6315		
i=1					1,98008	0,95954	1,02054	5E-05	1,020565
i=2					1,98009	0,9595	1,02059		
i=1					1,84825	1,14603	0,70222	1E-05	0,702225
i=2					1,8482	1,14597	0,70223		
i=1					1,96007	0,82478	1,13529	0,00018	1,13538
i=2					1,96028	0,82481	1,13547		
i=1					2,01125	0,71657	1,29468	2E-05	1,29469
i=2					2,01128	0,71658	1,2947		
i=1		LV95			2,34928	1,09501	1,25427	2E-05	1,25428
i=2		6103			2,34928	1,09499	1,25429		

Sum of Forwards [m]:	-9,643345	LV956103 – KB8A
Sum of Backwards [m]:	9,644125	KB8A - LV956103
Mean height difference [m]:	-9,643735	
Difference |Bi + Fi| [mm]:	0,78	
Closing error [mm/km]:	0,816113	
Total distance (forward + backward) [km]:	0,95575	
Allowed difference [mm]	0,977624672	
Standard deviation [mm]	0,691285035	

2015 :

2015 data : (LV956103 – KB8A)

	POINT ID		DISTANCE [m]		Backsight [m]	Foresight [m]	Difference	Error [mm]	Mean
	From	To	Bi	Fi	Bi	Fi	dhi = Bi-Fi	dh2 - dh1	dh = (dh1+dh2)/2
i=1	LV95 4103		23,38	22,52	1,00157	2,11362	-1,11205	-6E-05	-1,11208
i=2					1,00158	2,11369	-1,11211		
i=1			21,8	21,08	0,51205	1,69957	-1,18752	0,0001	-1,18747
i=2					0,51208	1,6995	-1,18742		
i=1			25,73	25,56	0,59089	1,95562	-1,36473	-6E-05	-1,36476
i=2					0,59098	1,95577	-1,36479		
i=1			25,68	25,36	0,95604	1,70587	-0,74983	1E-04	-0,74978
i=2					0,95608	1,70581	-0,74973		
i=1			26,9	25,54	0,99544	2,1457	-1,15026	0,00016	-1,15018
i=2					0,99557	2,14567	-1,1501		
i=1			26,29	26,39	0,34641	1,81599	-1,46958	2E-05	-1,46957
i=2					0,34644	1,816	-1,46956		
i=1			23	22,93	0,81241	2,11645	-1,30404	1E-05	-1,304035
i=2					0,81237	2,1164	-1,30403		
i=1			26,01	24	1,14947	1,52339	-0,37392	4E-05	-0,3739
i=2					1,14961	1,52349	-0,37388		
i=1			21,75	21,91	1,70117	1,63839	0,06278	-3E-05	0,062765
i=2					1,70121	1,63846	0,06275		
i=1		KB8A	20,99	21,86	1,17254	2,16814	-0,9956	-9E-05	-0,995645
i=2					1,17244	2,16813	-0,99569		
i=1								0	0
i=2									
i=1	KB8A		21,85	21,02	2,16811	1,17252	0,99559	5E-05	0,995615
i=2					2,16802	1,17238	0,99564		
i=1			27,23	25,99	1,61563	1,73402	-0,11839	-3E-05	-0,118405
i=2					1,61566	1,73408	-0,11842		
i=1			25,49	24,29	1,68054	1,09767	0,58287	0,0001	0,58292
i=2					1,68067	1,0977	0,58297		
i=1			24,21	24,26	2,24046	,94599	1,29447	6E-05	1,2945
i=2					2,24048	,94595	1,29453		
i=1			23,07	23,49	1,99261	,34368	1,64893	1E-04	1,64898
i=2					1,99262	,34359	1,64903		
i=1			23,55	24,57	1,91951	1,07257	0,84694	-0,00012	0,84688
i=2					1,91944	1,07262	0,84682		
i=1			25,82	23,55	1,80908	1,04809	0,76099	-9E-05	0,760945
i=2					1,80901	1,04811	0,76090		

i=1			23,67	22,73	2,10275	,83347	1,26928	-6E-05	1,26925
i=2					2,10268	,83346	1,26922		
i=1			23,65	23,77	1,96578	,66109	1,30469	-0,00011	1,304635
i=2					1,9657	,66112	1,30458		
i=1		LV95 6103	22,61	22,35	2,20975	1,1501	1,05965	6E-05	1,05968
i=2					2,20979	1,15008	1,05971		

Sum of Forwards [m]:	-9,644655	LV956103 – KB8A
Sum of Backwards [m]:	9,645	KB8A - LV956103
Mean height difference [m]:	-9,6448275	
Difference |Bi + Fi| [mm]:	0,345	
Closing error [mm/km]:	0,360935293	
Total distance (forward + backward) [km]:	0,95585	
Allowed difference [mm]	0,977675815	
Standard deviation [mm]	0,691321199	

2016 :

2016 data : (LV056104 – KDMC)

	POINT ID		**DISTANCE [m]**		**Backsight [m]**	**Foresight [m]**	**Difference**	**Error [mm]**	**Mean**
	From	**To**	**Bi**	**Fi**	**Bi**	**Fi**	**dhi = Bi-Fi**	**dh2 - dh1**	**dh = (dh1+dh2)/2**
i=1	LV056104		26,01	28,25	0,25141	-0,41762	0,66903	9E-05	0,669075
i=2					0,25157	-0,41755	0,66912		
i=1			23,38	22,04	1,12778	-0,57353	1,70131	-4E-05	1,70129
i=2					1,12777	-0,5735	1,70127		
i=1			25,48	24,43	1,01662	-1,25104	2,26766	-6E-05	2,26763
i=2					1,01658	-1,25102	2,2676		
i=1			19,14	17,98	2,06392	-1,10768	3,1716	-4E-05	3,17158
i=2					2,06388	-1,10768	3,17156		
i=1			15,35	15,66	0,01124	-0,27752	0,28876	1E-04	0,28881
i=2					0,01134	-0,27752	0,28886		
i=1		KDMC	10,08	10,91	0,64496	-0,32967	0,97463	0,00012	0,97469
i=2					0,64501	-0,32974	0,97475		
i=1	KDMC		6,33	5,47	-0,62685	0,49331	-1,12016	-1E-05	-1,120165
i=2					-0,62686	0,49331	-1,12017		
i=1			18,52	19,45	-0,03737	0,78757	-0,82494	-0,00012	-0,825
i=2					-0,03744	0,78762	-0,82506		
i=1			25,39	24,72	-0,11603	2,43369	-2,54972	9E-05	-2,549675

i=2					-0,11599	2,43364	-2,54963		
i=1			24,45	23,71	-1,41114	2,03323	-3,44437	2E-05	-3,44436
i=2					-1,41113	2,03322	-3,44435		
i=1			21,41	21,64	0,46319	1,03359	-0,5704	6E-05	-0,57037
i=2					0,46321	1,03355	-0,57034		
i=1		LV05	29,23	29,24	-0,54298	0,02095	-0,56393	0,00014	-0,56386
i=2		6104			-0,5429	0,02089	-0,56379		

Sum of Forwards [m]:	-9,073430	KDMC - LV056104
Sum of Backwards [m]:	9,073075	LV056104 - KDMC
Mean height difference [m]:	-9,0732525	
Difference |Bi + Fi| [mm]:	0,355	
Closing error [mm/km]:	0,727056751	
Total distance (forward + backward) [km]:	0,48827	
Allowed difference [mm]	0,698763193	
Standard deviation [mm]	0,494100192	

2016: KDMC – L595

	POINT ID		**DISTANCE [m]**		**Backsight [m]**	**Foresight [m]**	**Difference**	**Error [mm]**	**Mean**
	From	**To**	**Bi**	**Fi**	**Bi**	**Fi**	**dhi = Bi-Fi**	**dh2 - dh1**	**dh = (dh1+dh2)/2**
i=1	KDM		10,91	10,08	-0,32966	0,64501	-0,97467	-6E-05	-0,9747
i=2	C				-0,32971	0,64502	-0,97473		
i=1			23,96	24,08	-0,88871	-0,12892	-0,75979	-9E-05	-0,759835
i=2					-0,88878	-0,1289	-0,75988		
i=1			25,72	24,69	0,23428	-0,57221	0,80649	-4E-05	0,80647
i=2					0,23425	-0,5722	0,80645		
i=1			24,03	23,4	0,98812	-0,98801	1,97613	0	1,97613
i=2					0,98819	-0,98794	1,97613		
i=1			17,86	20,37	2,00948	-1,06077	3,07025	2E-05	3,07026
i=2					2,00951	-1,06076	3,07027		
i=1			12,64	12,05	1,81504	-1,30302	3,11806	6E-05	3,11809
i=2					1,81511	-1,30301	3,11812		
i=1			14,46	14,99	1,57414	-0,56971	2,14385	-6E-05	2,14382
i=2					1,57412	-0,56967	2,14379		
i=1		L595	8,45	8,88	0,08038	-0,02669	0,10707	-7E-05	0,107035
i=2					0,08036	-0,02664	0,107		
i=1							0	0	0
i=2							0		
i=1	L595		23,74	25,36	-1,1741	2,4954	-3,6695	-4E-05	-3,66952
i=2					-1,17416	2,49538	-3,66954		
i=1			23,66	23,79	-1,1661	2,60169	-3,76779	-0,00018	-3,76788

i=2					-1,16628	2,60169	-3,76797		
i=1			20,59	20,63	-1,32203	1,44041	-2,76244	-0,0001	-2,76249
i=2					-1,32205	1,44049	-2,76254		
i=1			24,92	24,64	-1,25353	0,3385	-1,59203	0	-1,59203
i=2					-1,25352	0,33851	-1,59203		
i=1			27,36	28,32	-0,12198	-1,30638	1,1844	-6E-05	1,18437
i=2					-0,12198	-1,30632	1,18434		
i=1		KDMC	5,46	6,33	0,49329	-0,62691	1,1202	1E-05	1,120205
i=2					0,49325	-0,62696	1,12021		

Sum of Forwards [m]:	9,487270	KDMC - L595
Sum of Backwards [m]:	-9,487345	L595 - KDMC
Mean height difference [m]:	9,4873075	
Difference |Bi + Fi| [mm]:	0,075	
Closing error [mm/km]:	0,141144589	
Total distance (forward + backward) [km]:	0,53137	
Allowed difference [mm]	0,728951302	
Standard deviation [mm]	0,515446408	

2017 :

2017 data: LV056104 – KDMC (DAY 1)

	POINT ID		**DISTANCE [m]**		**Backsight [m]**	**Foresight [m]**	**Difference**	**Error [mm]**	**Mean**
	From	**To**	**Bi**	**Fi**	**Bi**	**Fi**	**dhi = Bi-Fi**	**dh2 - dh1**	**dh = (dh1+dh2)/2**
i=1	KDMC		34,96	34,27	1,08532	3,83652	-2,7512	8E-05	-2,75116
i=2					1,08549	3,83661	-2,75112		
i=1			29,68	29,06	0,05565	3,94701	-3,89136	0,00059	-3,891065
i=2					0,05599	3,94676	-3,89077		
i=1			27,82	28,24	1,18667	2,89284	-1,70617	-1E-05	-1,706175
i=2					1,18665	2,89283	-1,70618		
i=1		LV104	26,77	26,92	0,72229	1,44394	-0,72165	0,00055	-0,721375
i=2					0,72264	1,44374	-0,7211		
								0	0
i=1	LV104		26,93	26,75	1,44407	0,72265	0,72142	-0,00021	0,721315
i=2					1,44382	0,72261	0,72121		

i=1			28,08	28,23	3,04696	1,3347	1,71226	-0,00026	1,71213
i=2					3,0472	1,3352	1,712		
i=1			29,61	29,08	4,00141	0,13354	3,86787	0,00025	3,867995
i=2					4,00159	0,13347	3,86812		
i=1		KDMC	34,67	34,82	3,82774	1,05805	2,76969	-1E-04	2,76964
i=2					3,82747	1,05788	2,76959		

2017 data: LV056104 – KDMC (DAY 2)

	POINT ID		DISTANCE [m]		Backsight [m]	Foresight [m]	Difference	Error [mm]	Mean
	From	To	Bi	Fi	Bi	Fi	dhi = Bi-Fi	dh2 - dh1	dh = (dh1+dh2)/2
i=1	LV056104		32,46	31,99	2,69291	1,47075	1,22216	-8E-05	1,22212
i=2					2,69288	1,4708	1,22208		
i=1			24,35	24,51	3,07114	0,56909	2,50205	-9E-05	2,502005
i=2					3,0711	0,56914	2,50196		
i=1			20,23	21,17	2,12703	1,33439	0,79264	-8E-05	0,7926
i=2					2,12701	1,33445	0,79256		
i=1			17,35	17,67	3,41075	0,13087	3,27988	-6E-05	3,27985
i=2					3,41104	0,13122	3,27982		
i=1			15	14,49	1,75834	1,0155	0,74284	0	0,74284
i=2					1,7584	1,01556	0,74284		
i=1		KDMC	16,15	15,27	1,1013	0,56805	0,53325	-5E-05	0,533225
i=2					1,1013	0,5681	0,5332		
i=1							0	0	0
i=2							0		
i=1	KDMC		15,26	16,16	0,56798	1,10123	-0,53325	0,00011	-0,533195
i=2					0,56807	1,10121	-0,53314		
i=1			14,55	14,96	1,01138	1,75441	-0,74303	3E-05	-0,743015
i=2					1,01144	1,75444	-0,743		
i=1			20,01	20,38	0,19207	3,47665	-3,28458	1E-05	-3,284575
i=2					0,19216	3,47673	-3,28457		
i=1			20,3	20,26	1,07018	1,85234	-0,78216	5E-05	-0,782135
i=2					1,07025	1,85236	-0,78211		
i=1			24,28	24,69	1,05678	3,56731	-2,51053	-5E-05	-2,510555
i=2					1,05675	3,56733	-2,51058		

i=1		**LV05 6104**	31,7	32,71	1,76266	2,97961	-1,21695	-7E-05	-1,216985
i=2					1,76249	2,97951	-1,21702		

Sum of Forwards [m]	-9,07046	Using the second half of the second day (KDMC-LV056104)
Sum of backwards [m]	9,07108	Using the second half of the first day (LV056104-KDMC)
Mean height difference [m]:	-9,07077	
Difference |Bi + Fi| [mm]:	0,62	
Closing error [mm/km]:	1,256510549	
Total distance (Forward + backward) [km]:	0,49343	
Allowed difference [mm]	0,702445727	
Standard deviation [mm]	0,496704137	

2017 : KDMC – L595

	POINT ID		**DISTANCE [m]**		**Backsight [m]**	**Foresight [m]**	**Difference**	**Error [mm]**	**Mean**
	From	**To**	**Bi**	**Fi**	**Bi**	**Fi**	**dhi = Bi-Fi**	**dh2 - dh1**	**dh = (dh1+dh2)/2**
i=1	KDMC		34,82	33,74	1,14068	1,54143	-0,40075	-0,00017	-0,400835
i=2					1,14063	1,54155	-0,40092		
i=1			28,4	28,18	1,90415	0,8142	1,08995	-4E-05	1,08993
i=2					1,90443	0,81452	1,08991		
i=1			22,46	22,39	2,87142	0,04832	2,8231	-0,0001	2,82305
i=2					2,87131	0,04831	2,823		
i=1			12,86	12,54	2,4926	1,01331	1,47929	-1E-05	1,479285
i=2					2,49263	1,01335	1,47928		
i=1			28,29	28,22	3,35996	0,28484	3,07512	1E-05	3,075125
i=2					3,35998	0,28485	3,07513		
i=1			22,55	21,42	2,07231	1,05832	1,01399	3E-05	1,014005
i=2					2,07248	1,05846	1,01402		
i=1			13,63	12,86	1,6676	1,74259	-0,07499	-0,00015	-0,075065
i=2					1,66741	1,74255	-0,07514		
i=1		L595	16,62	16,62	1,66894	1,18262	0,48632	-5E-05	0,486295
i=2					1,66891	1,18264	0,48627		
i=1							0	0	0
i=2							0		
i=1	L595		18,86	18,98	1,039	1,35959	-0,32059	2E-05	-0,32058
i=2					1,039	1,35957	-0,32057		
i=1			20,3	19,96	1,33066	1,96895	-0,63829	0	-0,63829
i=2					1,33069	1,96898	-0,63829		
i=1			22,27	21,88	0,92719	2,28018	-1,35299	0	-1,35299
i=2					0,92723	2,28022	-1,35299		

i=1			15,57	15,08	0,35324	2,41383	-2,06059	-1E-04	-2,06064
i=2					0,35312	2,41381	-2,06069		
i=1			16,25	16,13	0,67109	2,56995	-1,89886	0	-1,89886
i=2					0,67108	2,56994	-1,89886		
i=1			20,1	19,99	0,04046	2,53737	-2,49691	2E-05	-2,4969
i=2					0,04042	2,53731	-2,49689		
i=1			15,67	15,74	0,94343	1,83781	-0,89438	-2E-05	-0,89439
i=2					0,94339	1,83779	-0,8944		
i=1			16,25	15,9	1,29503	1,53195	-0,23692	-0,00012	-0,23698
i=2					1,29491	1,53195	-0,23704		
i=1			13,29	12,81	1,02888	1,43292	-0,40404	-2E-05	-0,40405
i=2					1,0289	1,43296	-0,40406		
i=1		KDMC	12,57	12,91	1,91997	1,10809	0,81188	7E-05	0,811915
i=2					1,92004	1,10809	0,81195		

Sum of Forwards [m]:	9,491790	KDMC – L595
Sum of Backwards [m]:	-9,491765	L595 - KDMC
Mean height difference [m]:	9,4917775	
Difference |Bi + Fi| [mm]:	0,025	
Closing error [mm/km]:	0,035913864	
Total distance (forward + backward) [km]:	0,69611	
Allowed difference [mm]	0,834332068	
Standard deviation [mm]	0,589961863	

2017 : (LV956103 – KB8A)

	POINT ID		**DISTANCE [m]**		**Backsight [m]**	**Foresight [m]**	**Difference**	**Error [mm]**	**Mean**
	From	**To**	**Bi**	**Fi**	**Bi**	**Fi**	**dhi = Bi-Fi**	**dh2 - dh1**	**dh = (dh1+dh2)/2**
i=1	**LV956103**		28,91	28,77	1,09323	2,65127	-1,55804	-9E-05	-1,558085
i=2					1,09313	2,65126	-1,55813		
i=1			31,15	31,29	0,67621	2,24147	-1,56526	0,00017	-1,565175
i=2					0,67635	2,24144	-1,56509		
i=1			28,41	28,84	0,76446	1,86887	-1,10441	0,00018	-1,10432
i=2					0,76453	1,86876	-1,10423		
i=1			29,93	29,62	0,97309	1,92639	-0,9533	-5E-05	-0,953325
i=2					0,97306	1,92641	-0,95335		
i=1			19,81	19,55	0,36316	1,9879	-1,62474	1E-05	-1,624735
i=2					0,36318	1,98791	-1,62473		
i=1			18,74	17,97	1,1999	1,61632	-0,41642	6E-05	-0,41639
i=2					1,19992	1,61628	-0,41636		
i=1			29,53	29,43	1,48033	1,6324	-0,15207	-0,0002	-0,15217

i=2					1,48013	1,6324	-0,15227		
i=1			26,86	27,79	0,35687	0,93156	-0,57469	4E-05	-0,57467
i=2					0,357	0,93165	-0,57465		
i=1			20,34	20,91	0,8123	0,82237	-0,01007	-9E-05	-0,010115
i=2					0,81227	0,82243	-0,01016		
i=1		KB8A	20,56	21,5	0,43521	2,11348	-1,67827	7E-05	-1,678235
i=2					0,43518	2,11338	-1,6782		
i=1							0	0	0
i=2							0		
i=1	KB8A		21,49	20,57	2,1135	0,43535	1,67815	-0,0002	1,67805
i=2					2,11361	0,43566	1,67795		
i=1			20,34	20,94	0,82722	0,81724	0,00998	8E-05	0,01002
i=2					0,82739	0,81733	0,01006		
i=1			26,64	26,72	0,9091	0,3342	0,5749	-6E-05	0,57487
i=2					0,90898	0,33414	0,57484		
i=1			29,45	29,5	1,51074	1,3585	0,15224	0,00012	0,1523
i=2					1,51094	1,35858	0,15236		
i=1			17,27	17,18	1,65428	1,27027	0,38401	-7E-05	0,383975
i=2					1,65421	1,27027	0,38394		
i=1			21,83	21,18	1,92872	0,22776	1,70096	-4E-05	1,70094
i=2					1,92924	0,22832	1,70092		
i=1			20	20,14	1,76314	1,07522	0,68792	1E-05	0,687925
i=2					1,76324	1,07531	0,68793		
i=1			18,88	18,52	1,55491	1,05355	0,50136	-6E-05	0,50133
i=2					1,55498	1,05368	0,5013		
i=1			20,53	20,4	1,67687	0,7574	0,91947	-0,00013	0,919405
i=2					1,67694	0,7576	0,91934		
i=1			16,78	16,87	1,7506	0,93716	0,81344	8E-05	0,81348
i=2					1,75072	0,9372	0,81352		
i=1			16,73	17,37	1,74204	0,70105	1,04099	0	1,04099
i=2					1,74213	0,70114	1,04099		
i=1		**LV956103**	24,58	24,44	2,16826	0,99371	1,17455	0	1,17455
i=2					2,16826	0,99371	1,17455		

Sum of Forwards [m]:	-9,637220	LV956103 – KB8A
Sum of Backwards [m]:	9,637835	KB8A - LV956103
Mean height difference [m]:	-9,6375275	
Difference |Bi + Fi| [mm]:	0,615	
Closing error [mm/km]:	0,603971481	
Total distance (forward + backward) [km]:	1,01826	
Allowed difference [mm]	1,009088698	
Standard deviation [mm]	0,713533461	

2018 :

2018 : LV056104 – KDMC

	POINT ID		DISTANCE [m]		Backsight [m]	Foresight [m]	Difference	Error [mm]	Mean
	From	To	Bi	Fi	Bi	Fi	dhi = Bi-Fi	dh2 - dh1	dh = (dh1+dh2)/2
i=1	KDMC		33,35	34,54	1,03649	2,91906	-1,88257	-8E-05	-1,88261
i=2					1,0362	2,91885	-1,88265		
i=1			15,24	14,94	0,27011	3,18791	-2,9178	-0,00014	-2,91787
i=2					0,26989	3,18783	-2,91794		
i=1			10,16	10,37	0,2708	2,50444	-2,23364	7E-05	-2,233605
i=2					0,27082	2,50439	-2,23357		
i=1			20,96	20,23	0,68152	1,9466	-1,26508	0,00012	-1,26502
i=2					0,68138	1,94634	-1,26496		
i=1			23,5	23,2	1,31006	2,20143	-0,89137	0,0001	-0,89132
i=2					1,31014	2,20141	-0,89127		
i=1		LV104	18,27	18,46	1,79141	1,66996	0,12145	-0,00019	0,121355
i=2					1,79122	1,66996	0,12126		
i=1							0	0	0
i=2							0		
i=1	LV104		18,45	18	1,67023	1,79137	-0,12114	-6E-05	-0,12117
i=2					1,67012	1,79132	-0,1212		
i=1			23,33	23,34	2,23192	1,3365	0,89542	-9E-05	0,895375
i=2					2,23189	1,33656	0,89533		
i=1			20,12	20,96	1,871	0,6098	1,2612	-3E-05	1,261185
i=2					1,87089	0,60972	1,26117		
i=1			9,92	10,55	2,55825	0,32478	2,23347	4E-05	2,23349
i=2					2,55831	0,3248	2,23351		
i=1			14,61	15,48	3,21244	0,29958	2,91286	0,00018	2,91295
i=2					3,21263	0,29959	2,91304		
i=1		KDMC	34,67	32,92	2,94307	1,05466	1,88841	3E-05	1,888425
i=2					2,94288	1,05444	1,88844		

Sum of Forwards [m]:	-9,069070	KDMC - LV056104
Sum of Backwards [m]:	9,070255	LV056104 - KDMC
Mean height difference [m]:	-9,069663	
Difference |Bi + Fi| [mm]:	1,185	
Closing error [mm/km]:	2,440430834	
Total distance (forward + backward) [km]:	0,48557	
Allowed difference [mm]	0,69682853	
Standard deviation [mm]	0,492732179	

2018 : LV956103 – KB8A

	POINT ID		DISTANCE [m]		Backsight [m]	Foresight [m]	Difference	Error [mm]	Mean
	From	To	Bi	Fi	Bi	Fi	dhi = Bi-Fi	dh2 - dh1	dh = (dh1+dh2)/2
i=1	LV956103		14,61	13,97	0,93656	1,29492	-0,35836	-0,00008	-0,3584
i=2					0,93652	1,29496	-0,35844		
i=1			13,08	12,48	0,93304	1,91445	-0,98141	-0,00008	-0,98145
i=2					0,93302	1,91451	-0,98149		
i=1			16,52	16,03	0,74042	1,70395	-0,96353	-0,00008	-0,96357
i=2					0,74045	1,70406	-0,96361		
i=1			21,13	21,35	0,87749	1,96354	-1,08605	0,00001	-1,086045
i=2					0,87751	1,96355	-1,08604		
i=1			22,42	21,92	0,91443	1,72192	-0,80749	-0,00004	-0,80751
i=2					0,91442	1,72195	-0,80753		
i=1			21,71	22,74	1,11072	1,6693	-0,55858	-0,00002	-0,55859
i=2					1,11069	1,66929	-0,55860		
i=1			18,13	18,67	1,09605	2,32459	-1,22854	0,00004	-1,22852
i=2					1,09613	2,32463	-1,22850		
i=1		TP1	18,36	18,49	0,54238	1,54036	-0,99798	-0,00003	-0,997995
i=2					0,54239	1,5404	-0,99801		
i=1	TP1		22,84	22,75	1,14956	2,36425	-1,21469	9E-05	-1,214645
i=2					1,14956	2,36416	-1,2146		
i=1			25,79	25,47	0,9211	1,46919	-0,54809	4E-05	-0,54807
i=2					0,92102	1,46907	-0,54805		
i=1			24,75	24,55	1,6134	1,51109	0,10231	0,00011	0,102365
i=2					1,6135	1,51108	0,10242		
i=1		KB8A	22,31	21,44	1,09494	2,0865	-0,99156	2E-05	-0,99155
i=2					1,09493	2,08647	-0,99154		
i=1	KB8A		21,46	22,33	2,08667	1,09516	0,99151	-0,00008	0,99147
i=2					2,08664	1,09521	0,99143		
i=1			24,73	24,34	1,57958	1,68208	-0,10250	0,00013	-0,102435
i=2					1,57967	1,68204	-0,10237		
i=1			25,09	25,76	1,37635	0,83986	0,53649	0,00003	0,536505
i=2					1,37639	0,83987	0,53652		
i=1			22,34	22,19	2,02484	0,79871	1,22613	-0,00009	1,226085
i=2					2,02476	0,79872	1,22604		
i=1			18,41	18,95	1,52598	0,48820	1,03778	-0,00003	1,037765
i=2					1,52605	0,48830	1,03775		
i=1			18,76	18,28	2,30544	1,11977	1,18567	0,00015	1,185745
i=2					2,30555	1,11973	1,18582		
i=1			22,49	21,94	1,68915	1,12819	0,56096	0,00006	0,56099
i=2					1,68917	1,12815	0,56102		
i=1			22,07	22,3	1,69902	0,91787	0,78115	-0,00011	0,781095
i=2					1,69899	0,91795	0,78104		

i=1			21,55	21,11	1,94215	0,84716	1,09499	-0,00003	1,094975
i=2					1,94221	0,84725	1,09496		
i=1			16,01	16,51	1,66033	0,74588	0,91445	0,00003	0,914465
i=2					1,66035	0,74587	0,91448		
i=1			12,57	12,94	1,93105	0,89935	1,03170	0,00007	1,031735
i=2					1,93109	0,89932	1,03177		
i=1		LV956103	13,99	14,61	1,29508	0,93665	0,35843	-0,00002	0,35842
i=2					1,29505	0,93664	0,35841		

Sum of Forwards [m]:	-9,633980	LV956103 – KB8A
Sum of Backwards [m]:	9,616815	KB8A - LV956103
Mean height difference [m]:	-9,6253975	
Difference |Bi + Fi| [mm]:	0,017165	
Closing error [mm/km]:	0,017838585	
Total distance (forward + backward) [km]:	0,96224	
Allowed difference [mm]	0,980938326	
Standard deviation [mm]	0,693628142	

2019:

2019 : KDMC –L595

	POINT ID		**DISTANCE [m]**		**Backsight [m]**	**Foresight [m]**	**Difference**	**Error [mm]**	**Mean**
	From	**To**	**Bi**	**Fi**	**Bi**	**Fi**	**dhi = Bi-Fi**	**dh2 - dh1**	**dh = (dh1+dh2)/2**
i=1	L595	1	21,46	21,48	1,00198	1,49379	-0,49181	-3E-05	-0,491825
i=2					1,00194	1,49378	-0,49184		
i=1			20,77	20,74	1,36394	2,01567	-0,65173	-3E-05	-0,651745
i=2					1,36394	2,0157	-0,65176		
i=1			23,76	24,92	0,91646	2,50927	-1,59281	3E-05	-1,592795
i=2					0,91646	2,50924	-1,59278		
i=1			10,18	11,91	0,27369	2,96196	-2,68827	-0,00016	-2,68835
i=2					0,27356	2,96199	-2,68843		
i=1			9,11	8,38	0,02473	2,8342	-2,80947	2E-05	-2,80946
i=2					0,02482	2,83427	-2,80945		
i=1			7,02	8,1	0,07405	1,7179	-1,64385	4E-05	-1,64383
i=2					0,07409	1,7179	-1,64381		
i=1			21,1	21,96	0,49429	1,58212	-1,08783	0,00021	-1,087725
i=2					0,49445	1,58207	-1,08762		
i=1			20,15	19,92	1,04823	1,06138	-0,01315	-1E-04	-0,0132
i=2					1,04817	1,06142	-0,01325		
i=1			10,74	11,68	1,49443	0,74026	0,75417	1E-05	0,754175
i=2					1,49446	0,74028	0,75418		

i=1		KDMC	13,34	14,43	1,14222	0,40873	0,73349	0,00011	0,733545
i=2					1,14235	0,40875	0,7336		
i=1							0	0	0
i=2							0		
i=1	KDMC	1	13,14	12,26	0,32385	1,66374	-1,33989	8E-05	-1,33985
i=2					0,32394	1,66375	-1,33981		
i=1	1	2	13,74	14,16	1,18571	1,53704	-0,35133	7E-05	-0,351295
i=2					1,18576	1,53702	-0,35126		
i=1	2	3	22,42	23,32	1,44387	1,07810	0,36577	-1E-05	0,365765
i=2					1,44384	1,07808	0,36576		
i=1	3	4	19,85	20,44	1,65045	1,07308	0,57737	-2E-05	0,57736
i=2					1,65041	1,07306	0,57735		
i=1	4	5	12,55	6,84	1,84897	0,07889	1,77008	-1E-05	1,770075
i=2					1,84902	0,07895	1,77007		
i=1	5	6	5,77	5,02	2,08775	0,21663	1,87112	3E-05	1,871135
i=2					2,08776	0,21661	1,87115		
i=1	6	7	9,99	5,22	2,76637	0,11842	2,64795	-1E-05	2,647945
i=2					2,76635	0,11841	2,64794		
i=1	7	8	7,17	5,66	2,40421	0,38681	2,0174	-6E-05	2,01737
i=2					2,40416	0,38682	2,01734		
i=1	8	9	17,35	17,67	2,07084	0,45751	1,61333	9E-05	1,613375
i=2					2,07087	0,45745	1,61342		
i=1	9	L595	10,98	11,01	1,32768	1,00940	0,31828	1E-05	0,318285
i=2					1,32770	1,00941	0,31829		

Sum of Forwards [m]:	9,490165	KDMC – L595
Sum of Backwards [m]:	-9,49121	L595 – KDMC
Mean height difference [m]:	9,4906875	
Difference |Bi + Fi| [mm]:	1,045	
Closing error [mm/km]:	1,815149989	
Total distance (forward + backward) [km]:	0,57571	
Allowed difference [mm]	0,75875556	
Standard deviation [mm]	0,536521202	

2019: KDMC - LV056104

	POINT ID		**DISTANCE [m]**		**Backsight [m]**	**Foresight [m]**	**Difference**	**Error [mm]**	**Mean**
	From	**To**	**Bi**	**Fi**	**Bi**	**Fi**	**dhi = Bi-Fi**	**dh2 - dh1**	**dh = (dh1+dh2)/2**
i=1	KDMC	1	25,97	27,09	0,72844	1,59365	-0,86521	2E-05	-0,8652
i=2					0,72846	1,59365	-0,86519		
i=1	1	2	19,86	19,78	0,17275	2,99921	-2,82646	4E-05	-2,82644
i=2					0,17273	2,99915	-2,82642		
i=1	2	3	10,14	9,88	0,10011	2,55796	-2,45785	0,00012	-2,45779

i=2					0,10025	2,55798	-2,45773		
i=1	3	4	10,42	10,99	0,44117	2,33877	-1,8976	-7E-05	-1,897635
i=2					0,44116	2,33883	-1,89767		
i=1	4	5	10,54	10,75	0,65713	2,05574	-1,39861	-8E-05	-1,39865
i=2					0,6571	2,05579	-1,39869		
i=1	5	6	14,25	13,45	0,81217	1,25483	-0,44266	0	-0,44266
i=2					0,81215	1,25481	-0,44266		
i=1	6	7	18,7	19,85	1,71832	0,66252	1,0558	-5E-05	1,055775
i=2					1,71827	0,66252	1,05575		
i=1	7	LV056104	13,3	10,34	1,06664	1,30433	-0,23769	-5E-05	-0,237715
i=2					1,06662	1,30436	-0,23774		
i=1									
i=2									
i=1	LV056104	IP1	21,77	21,41	1,6218	2,17778	-0,55598	8E-05	-0,55594
i=2					1,62187	2,17777	-0,5559		
i=1	IP1	IP2	19,21	19,19	1,17217	1,36257	-0,1904	1E-05	-0,190395
i=2					1,17205	1,36244	-0,19039		
i=1	IP2	IP3	13,23	13,61	2,40862	0,75514	1,65348	8E-05	1,65352
i=2					2,40869	0,75513	1,65356		
i=1	IP3	IP4	9,5	9,54	2,24523	0,52852	1,71671	0,00011	1,716765
i=2					2,24529	0,52847	1,71682		
i=1	IP4	IP5	8,44	8,84	2,31336	0,73405	1,57931	-4E-05	1,57929
i=2					2,31336	0,73409	1,57927		
i=1	IP5	IP6	10,28	10,84	2,7375	0,18474	2,55276	-3E-05	2,552745
i=2					2,7376	0,18487	2,55273		
i=1	IP6	IP7	15,91	15,9	1,45079	0,91792	0,53287	-0,00016	0,53279
i=2					1,45062	0,91791	0,53271		
i=1	IP7	KDMC	12,81	11,95	2,75687	0,97532	1,78155	2E-05	1,78156
i=2					2,75686	0,97529	1,78157		

Sum of Forwards [m]:	-9,070315	KDMC - LV056104
Sum of Backwards [m]:	9,070335	LV056104 - KDMC
Mean height difference [m]:	-9,070325	
Difference |Bi + Fi| [mm]:	0,02	
Closing error [mm/km]:	0,042758798	
Total distance (forward + backward) [km]:	0,46774	
Allowed difference [mm]	0,683915199	
Standard deviation [mm]	0,483601075	

B

GPS

B.1. Analysis on Individual Benchmarks

The vertical movement of the Individual benchmarks that have not been included in the GPS chapter is displayed in the following section (figures B.1 - B.22). The local up coordinate is used to represent the vertical deformation. Additionally, the pattern seen in the selected benchmarks in the Krafla region is also seen in KB11, THHY, L671 and L685 (Benchmarks of the Krafla region). To each and individual benchmark, there is a pattern seen. When the benchmarks are nearby, the same pattern is seen in general with a change in magnitude. This similarity in the pattern is seen in the benchmarks from the Krafla and Bjarnaflag region. They have their pattern in accordance with the region. For example, the benchmarks BF13, L603, FM15, etc. show a similar pattern where there is inflation seen up to 2017 from 2014. Then there is deflation seen in the region from 2017.

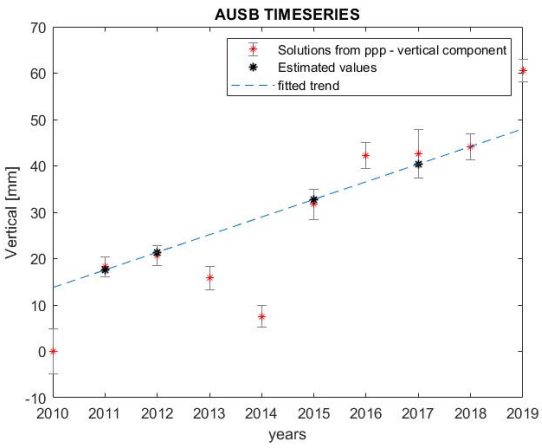

Figure B.1: Time series of the local up coordinate for the benchmark AUSB. The linear trend is fitted to this time series. The black star represents the estimated values and it is in line with the fitted trend. The other values with the red star are the outliers.

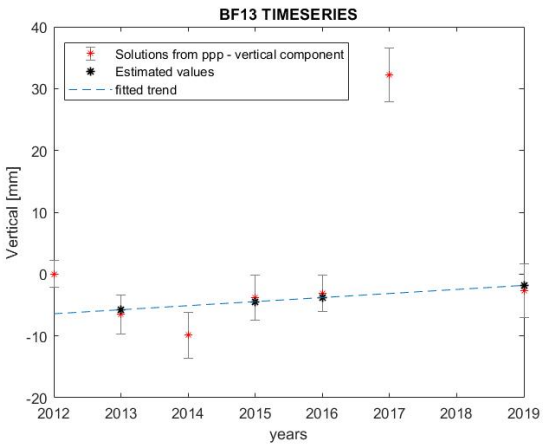

Figure B.2: Time series of the local up coordinate for the benchmark BF13. The linear trend is fitted to this time series. The black star represents the estimated values and it is in line with the fitted trend. The other values with the red star are the outliers.

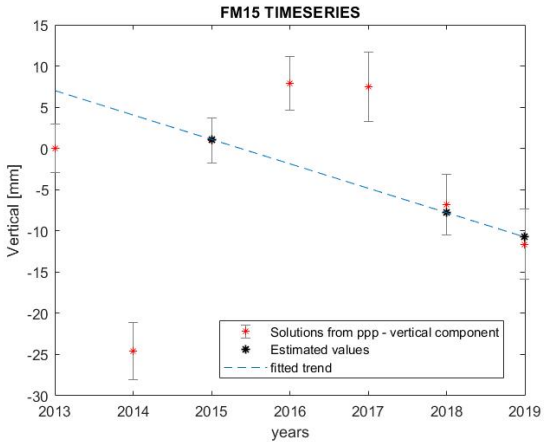

Figure B.3: Time series of the local up coordinate for the benchmark FM15. The linear trend is fitted to this time series. The black star represents the estimated values and it is in line with the fitted trend. The other values with the red star are the outliers.

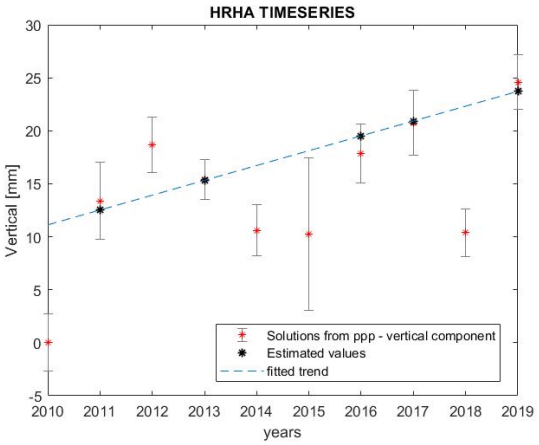

Figure B.4: Time series of the local up coordinate for the benchmark HRHA. The linear trend is fitted to this time series. The black star represents the estimated values and it is in line with the fitted trend. The other values with the red star are the outliers.

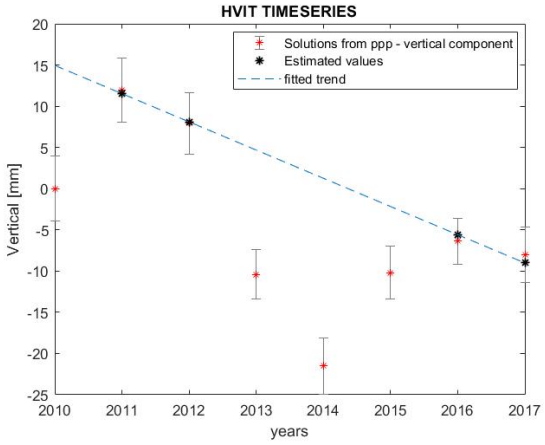

Figure B.5: Time series of the local up coordinate for the benchmark HVIT. The linear trend is fitted to this time series. The black star represents the estimated values and it is in line with the fitted trend. The other values with the red star are the outliers.

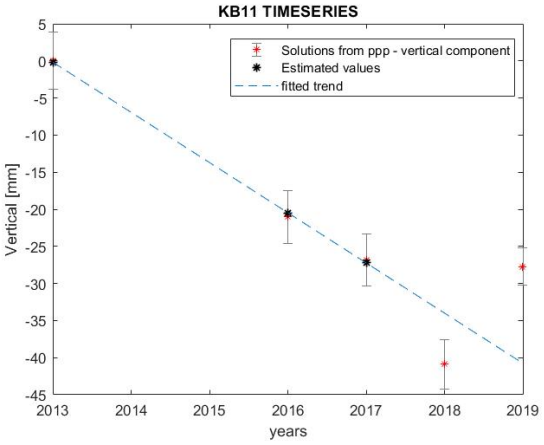

Figure B.6: Time series of the local up coordinate for the benchmark KB11. The linear trend is fitted to this time series. The black star represents the estimated values and it is in line with the fitted trend. The other values with the red star are the outliers.

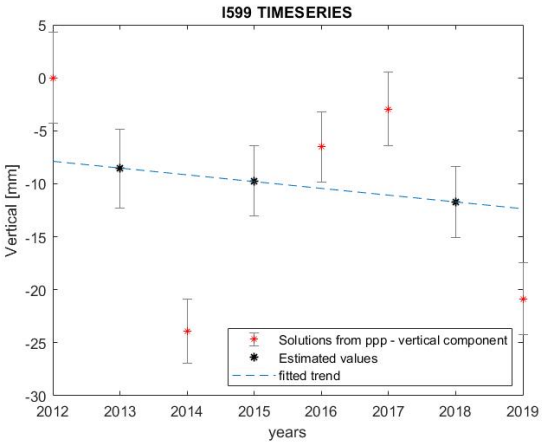

Figure B.7: Time series of the local up coordinate for the benchmark L599. The linear trend is fitted to this time series. The black star represents the estimated values and it is in line with the fitted trend. The other values with the red star are the outliers.

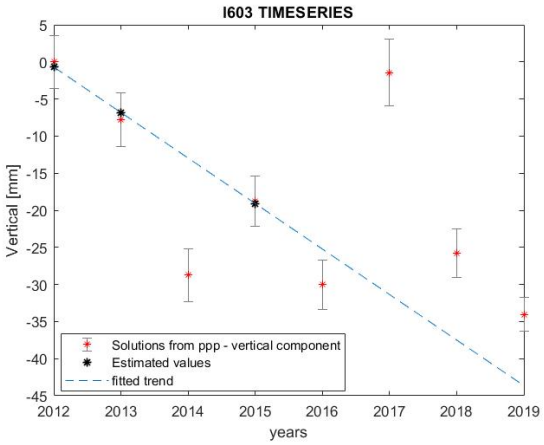

Figure B.8: Time series of the local up coordinate for the benchmark L603. The linear trend is fitted to this time series. The black star represents the estimated values and it is in line with the fitted trend. The other values with the red star are the outliers.

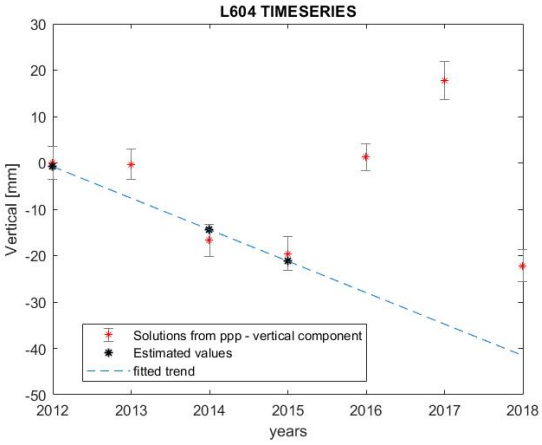

Figure B.9: Time series of the local up coordinate for the benchmark L604. The linear trend is fitted to this time series. The black star represents the estimated values and it is in line with the fitted trend. The other values with the red star are the outliers.

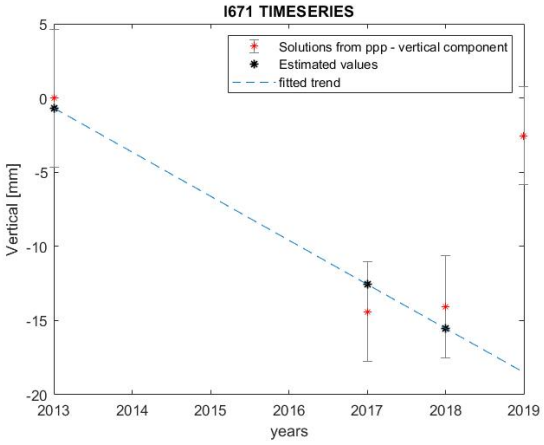

Figure B.10: Time series of the local up coordinate for the benchmark L603. The linear trend is fitted to this time series. The black star represents the estimated values and it is in line with the fitted trend. The other values with the red star are the outliers.

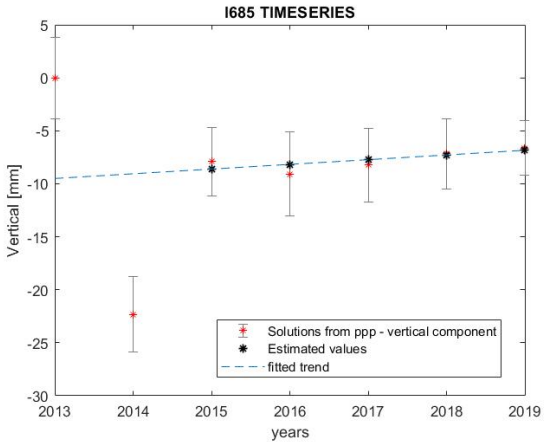

Figure B.11: Time series of the local up coordinate for the benchmark L685. The linear trend is fitted to this time series. The black star represents the estimated values and it is in line with the fitted trend. The other values with the red star are the outliers.

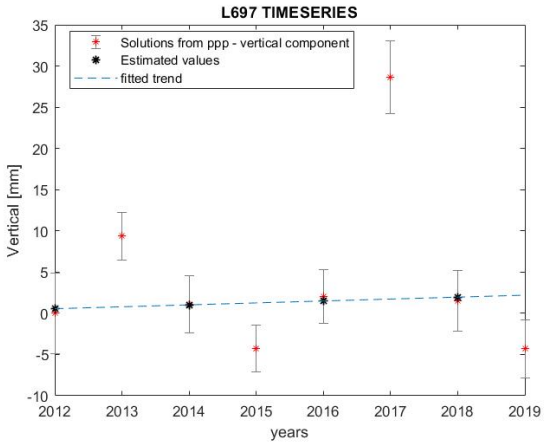

Figure B.12: Time series of the local up coordinate for the benchmark L697. The linear trend is fitted to this time series. The black star represents the estimated values and it is in line with the fitted trend. The other values with the red star are the outliers.

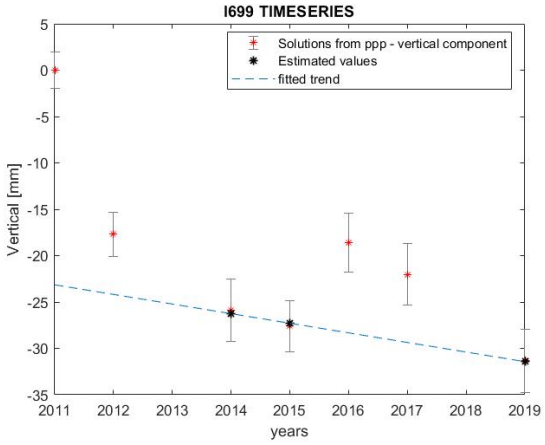

Figure B.13: Time series of the local up coordinate for the benchmark L699. The linear trend is fitted to this time series. The black star represents the estimated values and it is in line with the fitted trend. The other values with the red star are the outliers.

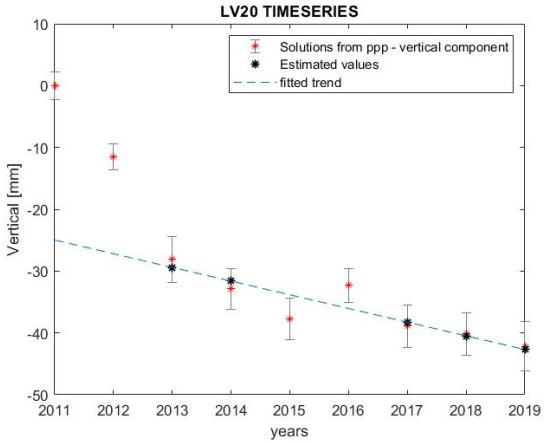

Figure B.14: Time series of the local up coordinate for the benchmark LV20. The linear trend is fitted to this time series. The black star represents the estimated values and it is in line with the fitted trend. The other values with the red star are the outliers.

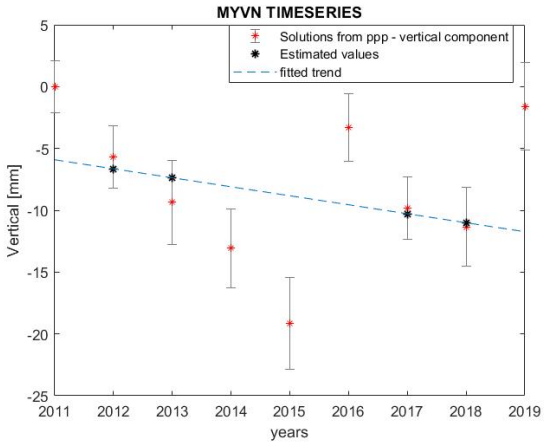

Figure B.15: Time series of the local up coordinate for the benchmark MYVN. The linear trend is fitted to this time series. The black star represents the estimated values and it is line with the fitted trend. The other values with the red star are the outliers.

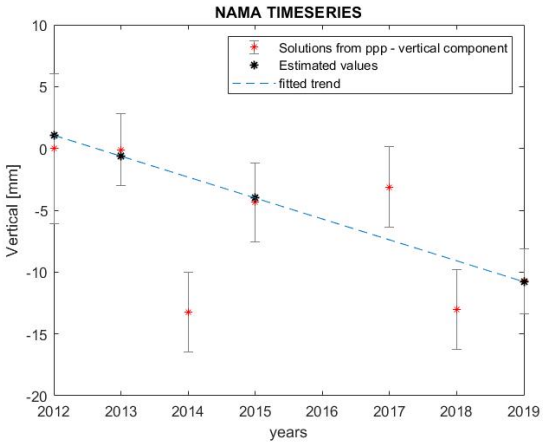

Figure B.16: Time series of the local up coordinate for the benchmark NAMA. The linear trend is fitted to this time series. The black star represents the estimated values and it is in line with the fitted trend. The other values with the red star are the outliers.

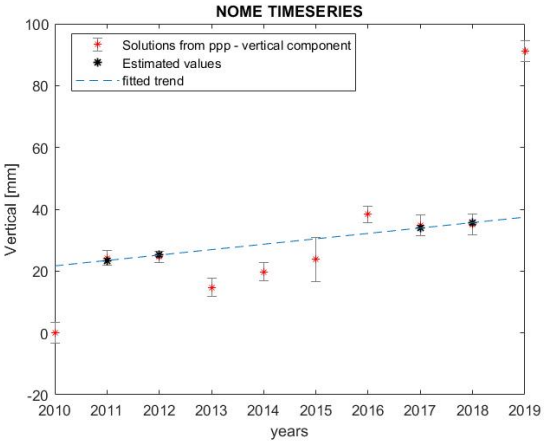

Figure B.17: Time series of the local up coordinate for the benchmark NOME. The linear trend is fitted to this time series. The black star represents the estimated values and it is in line with the fitted trend. The other values with the red star are the outliers.

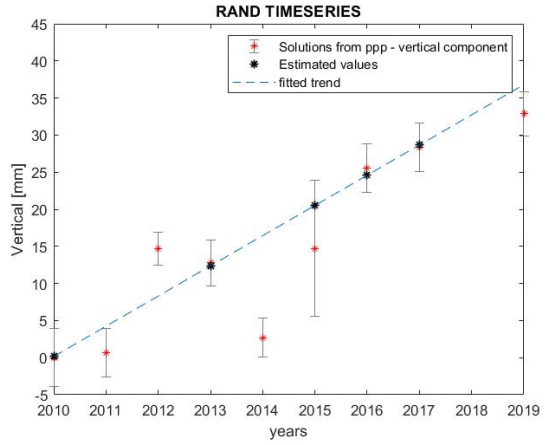

Figure B.18: Time series of the local up coordinate for the benchmark RAND. The linear trend is fitted to this time series. The black star represents the estimated values and it is in line with the fitted trend. The other values with the red star are the outliers.

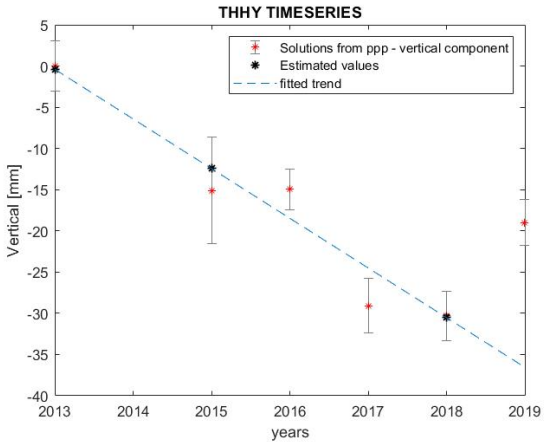

Figure B.19: Time series of the local up coordinate for the benchmark THHY. The linear trend is fitted to this time series. The black star represents the estimated values and it is line with the fitted trend. The other values with the red star are the outliers.

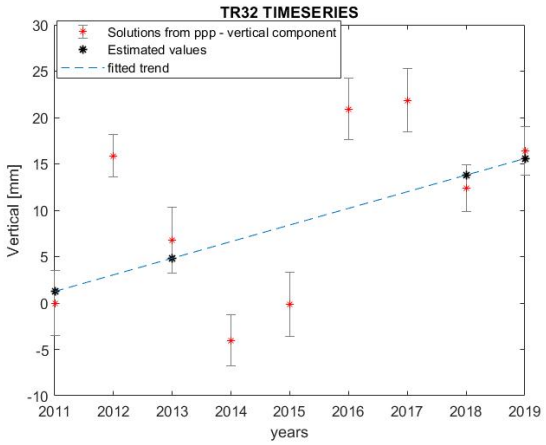

Figure B.20: Time series of the local up coordinate for the benchmark TR32. The linear trend is fitted to this time series. The black star represents the estimated values and it is in line with the fitted trend. The other values with the red star are the outliers.

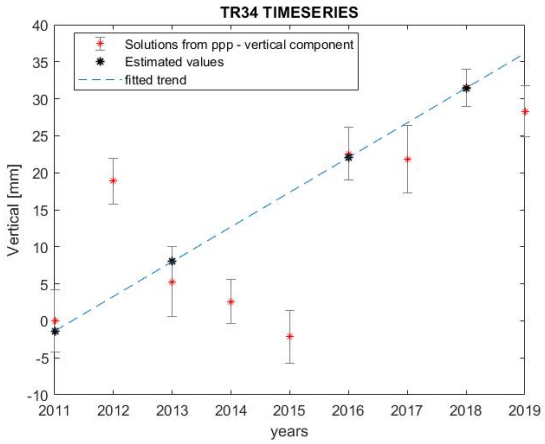

Figure B.21: Time series of the local up coordinate for the benchmark TR34. The linear trend is fitted to this time series. The black star represents the estimated values and it is in line with the fitted trend. The other values with the red star are the outliers.

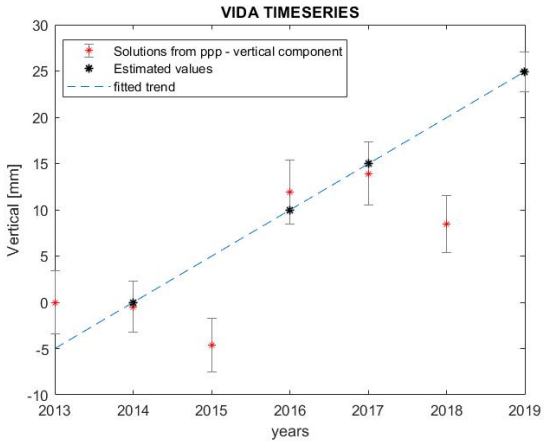

Figure B.22: Time series of the local up coordinate for the benchmark VIDA. The linear trend is fitted to this time series. The black star represents the estimated values and it is in line with the fitted trend. The other values with the red star are the outliers.

The following figure represents the time series of KRAC (Continuous GPS benchmark in Krafla region). The data is processed by Vincent Drouin using the GAMIT/GLOBK 10.6 software and daily solutions are given (source: [13]). These daily solutions are converted into yearly solutions and their residuals are calculated by fitting a linear trend and removing it from the data.

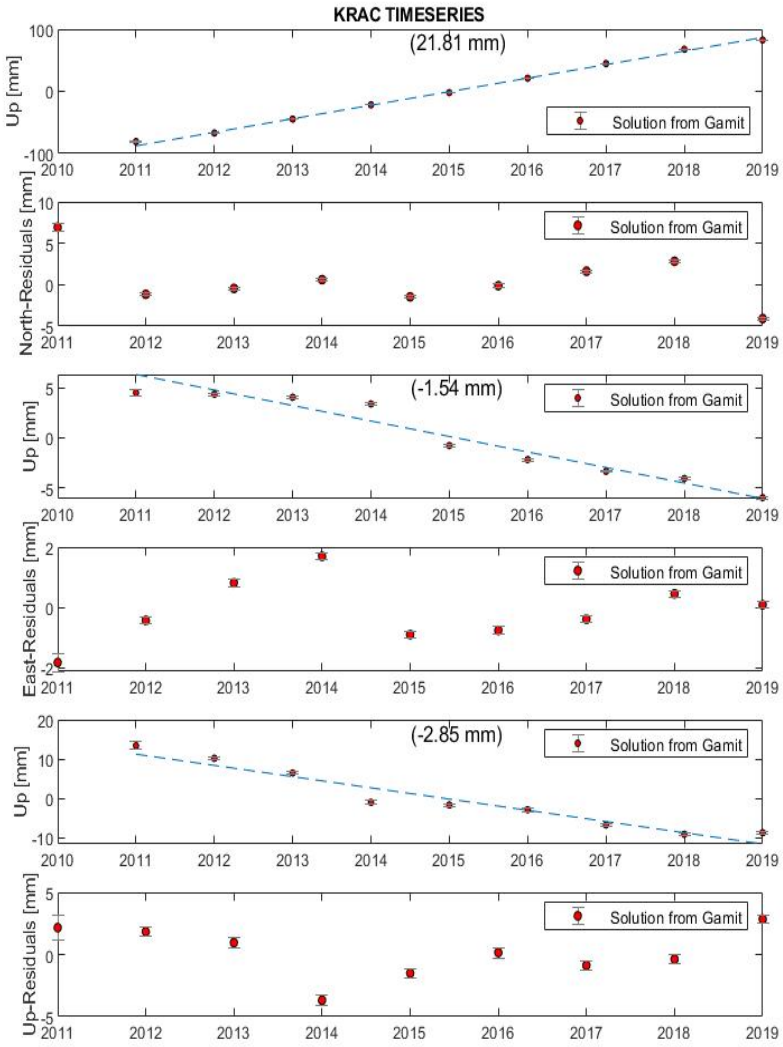

Figure B.23: Time series of East, North and Up coordinates of KRAC (Continuous GPS benchmark in Krafla region) and their respective residuals after removing the fitted linear trend.

C

InSAR

C.1. Processing of data

The steps executed in SNAP pre-processing are shown in the following figure C.1. Read-1 and 2 are the SLC products of the same pass. As the complete region do not fall in the same tile, consecutive images are taken and glued together using the slice Assembly operator. Then the Image is split into three subswaths (IW1, IW2 and IW3) for efficient processing. Then the following steps are performed to each of the subswath. The Orbit file is applied. The image obtained on 12th April, 2018 is used as the Master Image to produce Interferograms. Similarly, the Master image is divided into three subswaths. Then it is geo-coded to all the slave images. Read-3,4 and 5 represent the subswaths of the master image. The back-geocoding requires a DEM. Therefore an external DEM, named EU-DEM with a resolution of 25m is used for the analysis. Following this step, Enhanced Spectral Diversity (ESD) (Range and azimuth offsets are calculated) is done to all the subswaths which finally can be used in Interferogram formation. The phase is a mixture of Topographic phase and surface deformation. Therefore the image may contain the individual bursts. TOPSAR-Deburst is used to combine the individual bursts into a continuous image. This is applied to both the Interferogram and the output obtained from ESD which is the co-registered stack. Finally, all the Debursted Interferograms from the three subswaths are merged into one interferogram. 93 Interferograms are formed from 94 images. Similarly, the co-registered stack from ESD for each of the subswath is merged into one co-registered image. The processed images contain a lot of extra information and therefore the subset option is used to crop the required region. Finally, the subset of the co-registered stack and the Interferogram is used for the StaMPS export.

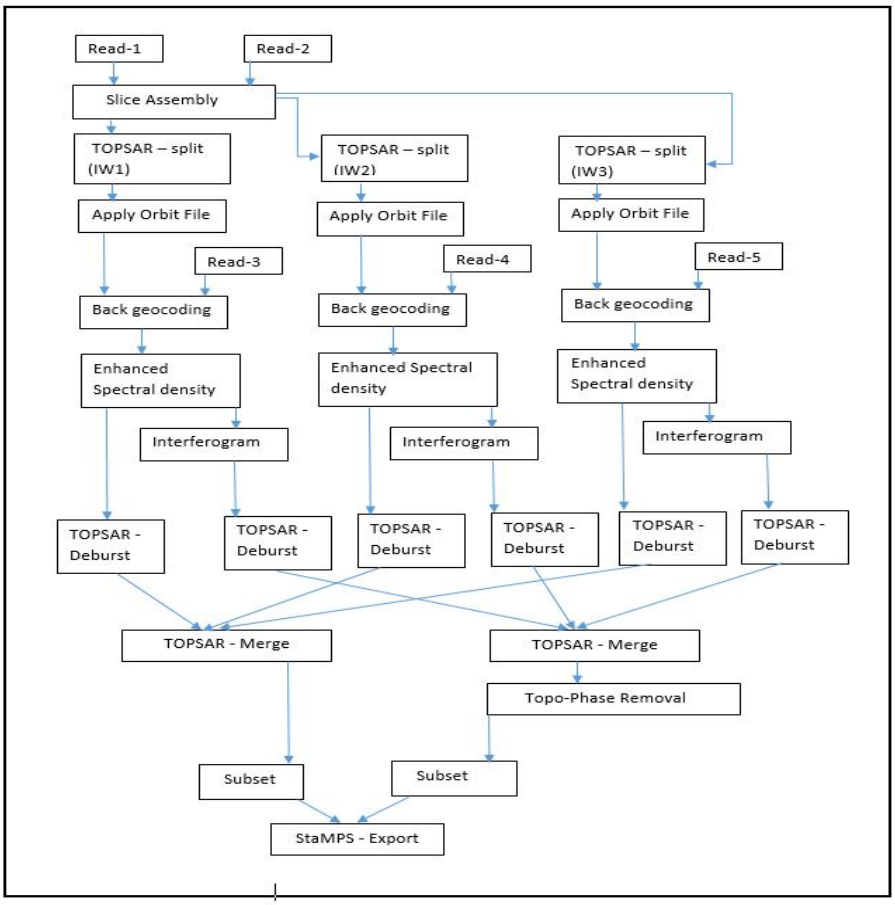

Figure C.1: Flowchart with the steps used for SNAP Pre-processing

With the StaMPS export, Initial set of pixels are selected using the amplitude dispersion. Then, the phase analysis is done to estimate the phase stability of the pixels in an iterative process. Further, the PS pixels are selected based on amplitude dispersion and phase stability. Certain pixels are then dropped based on their probability of being PS in some interferograms and being dominated by adjacent PS pixels in the others. Finally the unwrapping is done and the nuisances terms are subtracted from it to identify the signal due to deformation [27]. Step 1 to 7 in StaMPS perform the above mentioned procedure. Step 8 can be used used for Atmospheric filtering. There are various parameters present in StaMPS that can be changed accordingly to obtain the required results. Finally, the time series can be created from the selected pixels for the considered stack of Interferograms.

C.2. Results

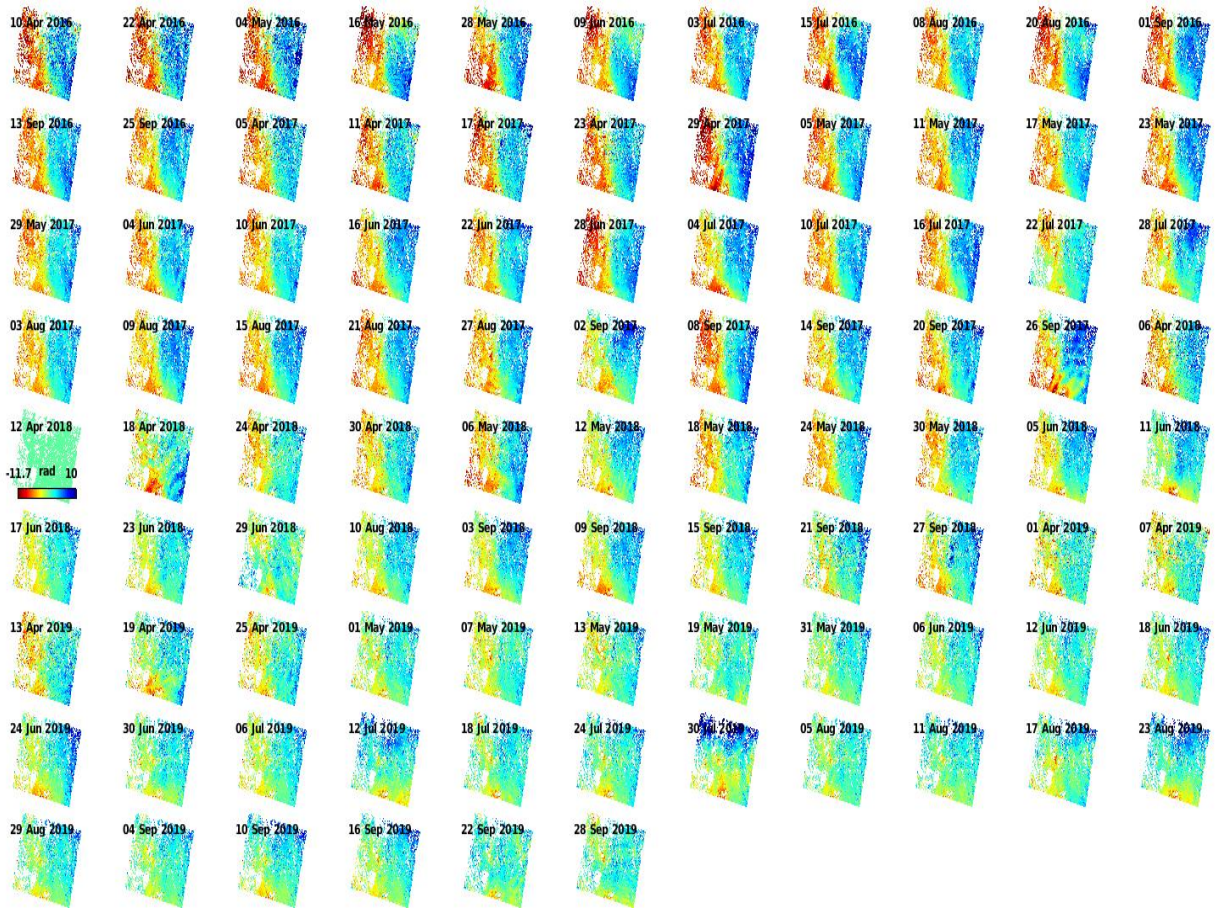

Figure C.2: Series of Unwrapped interferograms

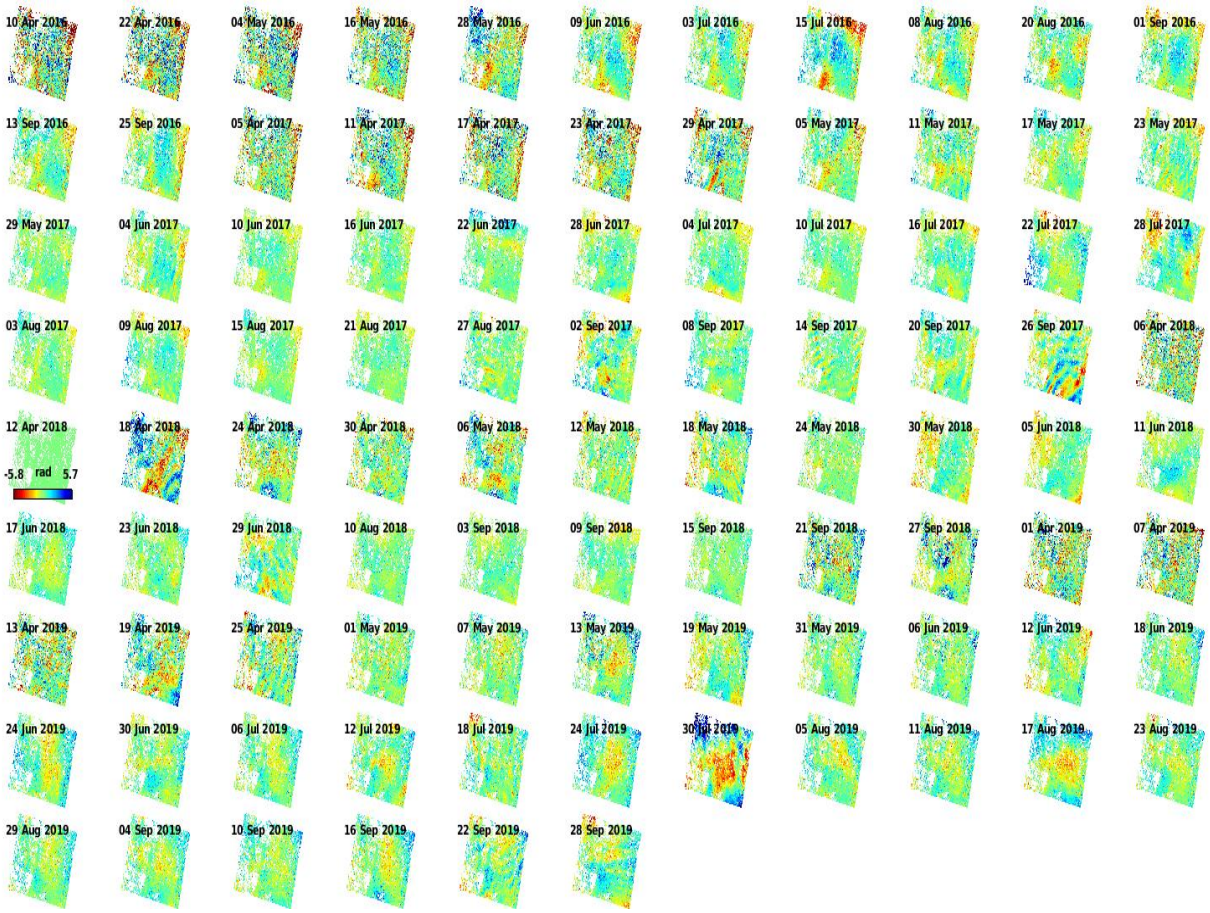

Figure C.3: Series of Unwrapped interferograms corrected for DEM, orbital and AOE error of the master image.

D

Modelling

Diagrammatic representation of the input data given into the modelling is displayed in the following figures (D.1 - D.3). First and foremost the GPS data in the form of horizontal vectors is given as input (as presented in figure D.1) . Then, the wrapped (figure D.3) and the unwrapped (figure D.2) interferograms of 30-05-2018 and 05-06-2018 with respect to 24th May 2018 is given as input.

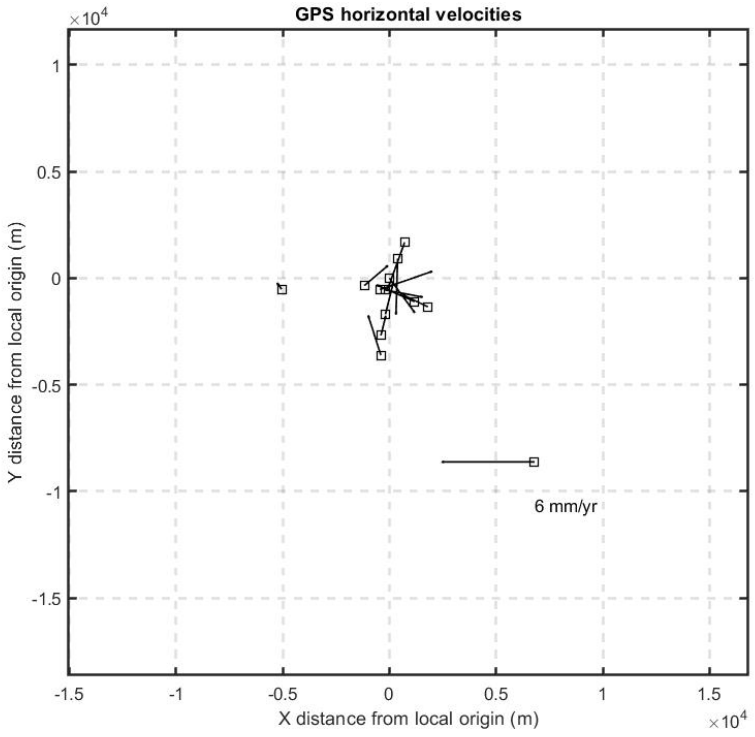

Figure D.1: Represents the GPS data (horizontal velocities) ingested into the model.

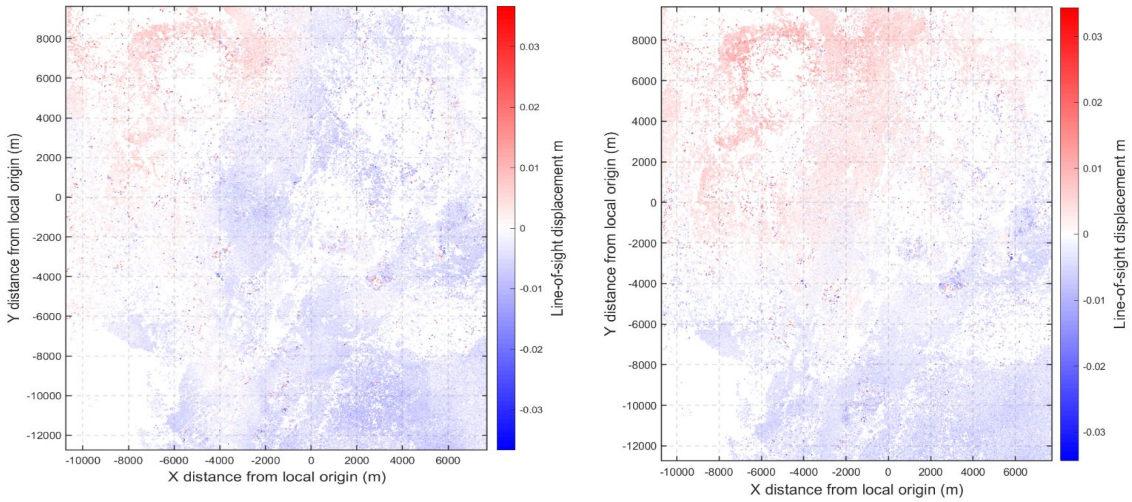

(a) Unwrapped Interferogram of 30-05-2018

(b) Unwrapped Interferogram of 05-06-2018

Figure D.2: Represents the Unwrapped interferograms corrected for various errors (DEM error, orbital error and Atmosphere and orbital error of master) captured on 30-05-2018 and 05-06-2018 with respect to 24-05-2018

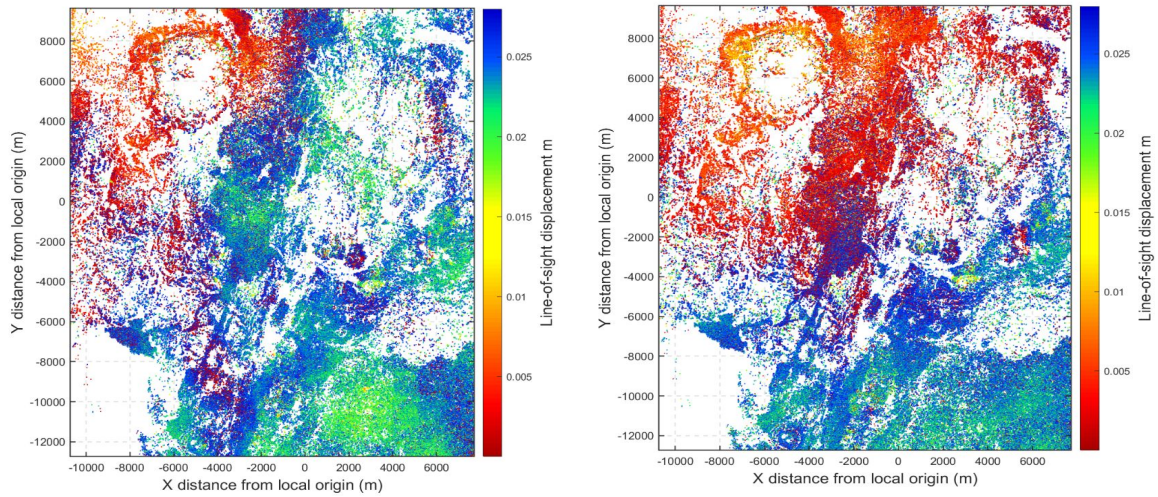

(a) Wrapped Interferogram of 30-05-2018

(b) Wrapped Interferogram of 05-06-2018

Figure D.3: Represents the Wrapped interferograms corrected for various errors (DEM error, orbital error and Atmosphere and orbital error of master) captured on 30-05-2018 and 05-06-2018 with respect to 24-05-2018

The following figures (D.4 - D.6) are also the results obtained from the modelling carried out in this work. Convergence plots indicate the retained values of that particular model parameter. Additionally, the Posterior source density function plot for each of the source parameter is displayed in the following figure D.5. The convergence plots and the PDF plot is displayed in the main report but again it is displayed here as well in along with the other results. Finally, the Joint probabilities of the source parameters are displayed in figure D.6.

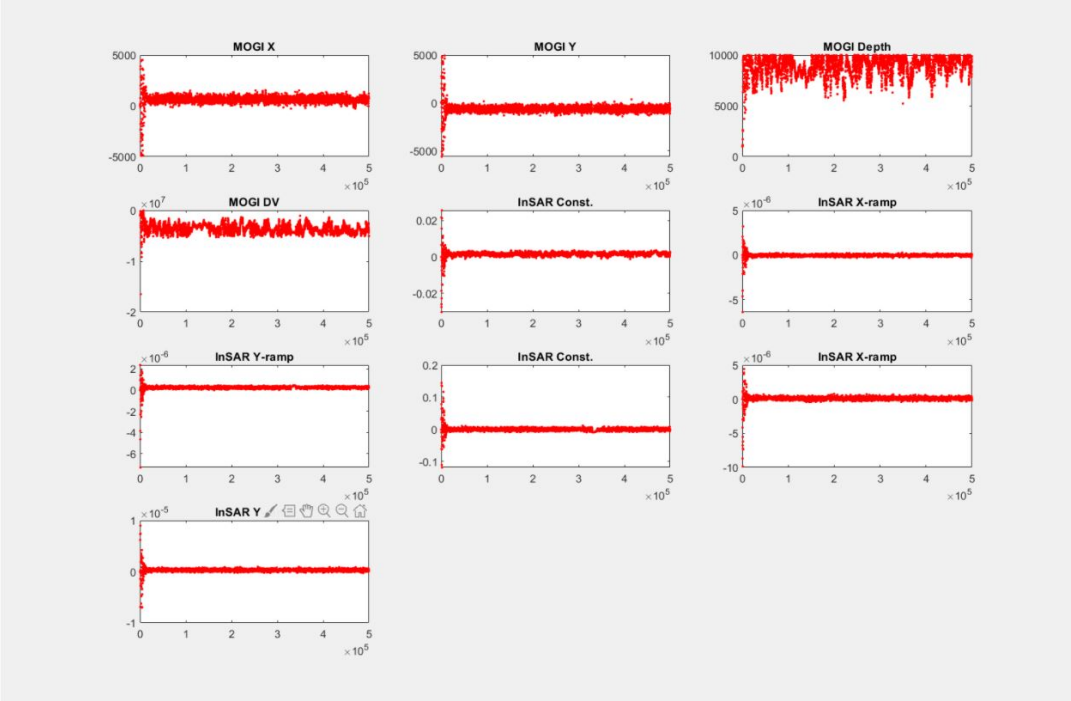

Figure D.4: Convergence plot for all the source model parameters. The x-axis represents the number of iterations.

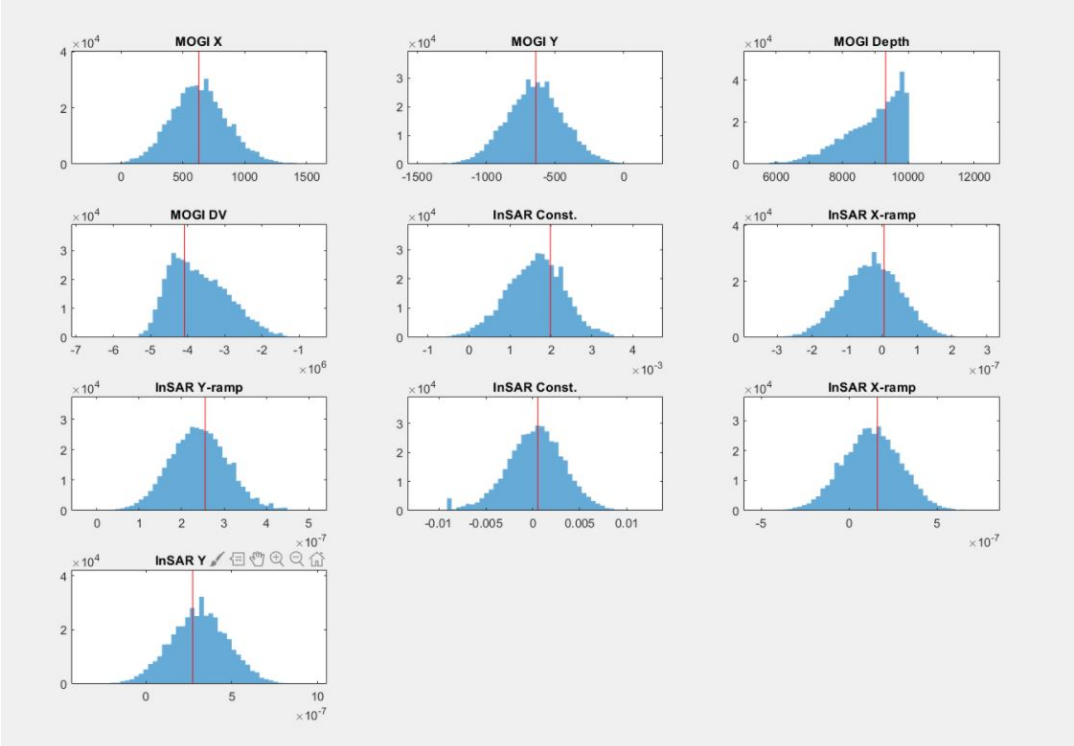

Figure D.5: Represents histogram of Posterior Density Function (PDF) of the source parameters (blue bars) and the optimal value is shown by red line.

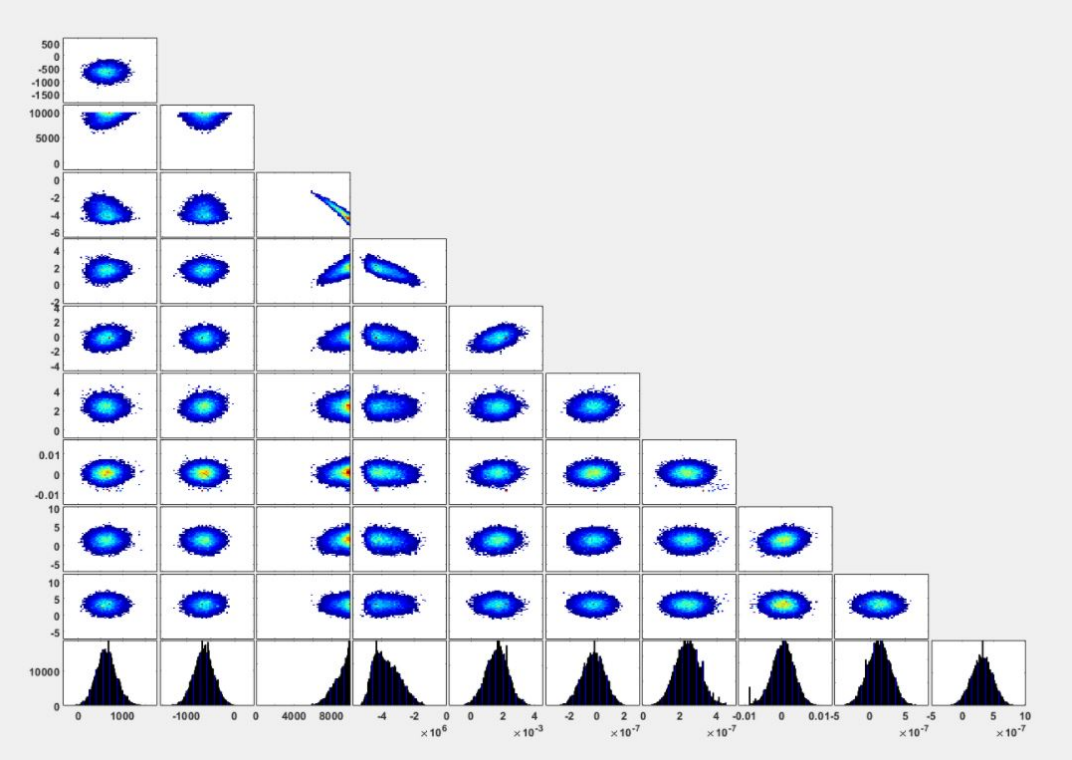

Figure D.6: Represents Joint PDF between the pairs of the source model parameters